AEOSR-TR- 93 0008

Annual Technical Report #2

November 1, 1991–October 31, 1992

New Micro- and Macroscopic Models of Contact and Friction

W. W. Tworzydlo, W. Cecot, J. T. Oden, and C. H. Yew

TR-92-15
November 1992

Contract F49620-91-C-0011

AIR FORCE OFFICE OF SCIENTIFIC RESEARCH
Building 410
Bolling Air Force Base, DC 20332-6448

Computational Mechanics Company, Inc.
7701 North Lamar, Suite 200
Austin, TX 78752

REPORT DOCUMENTATION PAGE

Form Approved
OMB No. 0704-0188

1. AGENCY USE ONLY *(Leave blank)*	2. REPORT DATE	3. REPORT TYPE AND DATES COVERED
	November 25, 1992	Annual, Nov. 1, 1991-Oct. 31, 1992

4. TITLE AND SUBTITLE

New Micro- and Macroscopic Models of Contact and Friction

5. FUNDING NUMBERS

C-F49620-91-C-0011
PR-2304/A3-2302/C2
TA-0001AA

6. AUTHOR(S)

W.W. Tworzydlo, W. Cecot, J.T. Oden, and C. H. Yew

7. PERFORMING ORGANIZATION NAME(S) AND ADDRESS(ES)

The Computational Mechanics Co., Inc.
7701 North Lamar, Suite 200
Austin, TX 78752

8. PERFORMING ORGANIZATION REPORT NUMBER

TR-92-15

9. SPONSORING / MONITORING AGENCY NAME(S) AND ADDRESS(ES)

The Air Force Office of Scientific Research
Building 410
Bolling AFB, DC 20332-6448

10. SPONSORING / MONITORING AGENCY REPORT NUMBER

UNKNOWN

11. SUPPLEMENTARY NOTES

12a. DISTRIBUTION / AVAILABILITY STATEMENT

Approved for public release;
distribution unlimited

12b. DISTRIBUTION CODE

13. ABSTRACT *(Maximum 200 words)*

This report summarizes work in the second year of a project devoted to the development of new asperity-based models of frictional interfaces. The main concept is to combine statistical homogenization methods with a realistic nonlinear finite element analysis of surface asperities, and thus produce new asperity-based models of contact and friction.

The research in the first year of the project provided a complete theory and software for statistical homogenization of random surface parameters.

In the second year of the project, the effort focused on the development of a finite element code for modeling of nonelastic surface asperities, as well as on the design and performance of the verification experiment. The asperity modeling code is based on an hp adaptive finite element kernel, with object-based data structure, error esitmation and graphic user interface. The code is capable of modeling elastic and elasto-viscoplastic solids in contact with a rigid flat. In parallel with the code development, an experiment was designed and performed for custom-made asperities in contact with rigid surfaces. The results of these experiments compare favorably with numerical predictions of the finite element method. Finally, the results of the finite element analysis were used to construct the first asperity-bsaed contact model of random surface. This work will continue in the next year.

14. SUBJECT TERMS

contact, friction, asperity, adhesion, interface, finite elements, viscoplastic

15. NUMBER OF PAGES

98

16. PRICE CODE

N/A

17. SECURITY CLASSIFICATION OF REPORT	18. SECURITY CLASSIFICATION OF THIS PAGE	19. SECURITY CLASSIFICATION OF ABSTRACT	20. LIMITATION OF ABSTRACT
Unclassified	Unclassified	Unclassified	UL

Annual Technical Report #2
November 1, 1991–October 31, 1992

New Micro- and Macroscopic Models of Contact and Friction

W. W. Tworzydlo, W. Cecot, J. T. Oden, and C. H. Yew

TR-92-15
November 1992

Contract F49620-91-C-0011

AIR FORCE OFFICE OF SCIENTIFIC RESEARCH
Building 410
Bolling Air Force Base, DC 20332-6448

Computational Mechanics Company, Inc.
7701 North Lamar, Suite 200
Austin, TX 78752

Contents

1 Introduction **1**

1.1 Summary of Objectives of the Project 2

1.2 Research Progress 2

1.3 Outline of the Report 3

1.4 Presentations and Publications 4

2 Asperity–Based Models of Contact and Friction **5**

2.1 Microstructure of the Frictional Interface 10

2.2 Statistics of a Random Surface 14

2.3 Calculation of Surface Statistics From Profile Data 16

2.3.1 Profiles on Gaussian Isotropic Surfaces 16

2.3.2 Profiles on Gaussian Anisotropic Surfaces 19

2.4 Calculation of Asperity Statistics From Surface Statistics 20

2.4.1 Asperity Statistics for Gaussian Isotropic Surfaces 20

2.4.2 Asperity Statistics for Gaussian Anisotropic Surfaces 21

2.4.3 Asperity Statistics for Deterministic Surfaces 21

2.5 Calculation of Macrocontact Expectations of Interface Parameters 24

2.5.1 Expectation Calculation for Gaussian Isotropic Surfaces 26

2.5.2 Expectation Calculation for Random Anisotropic Surfaces 27

2.5.3 Expectation Calculation for Deterministic Surfaces 29

2.6 Numerical Verification of Statistical Postprocessing 29

3 Deformation Mechanics of a Single Asperity **29**

3.1 Momentum and Geometric Equations 29

3.2 Constitutive Equations 30

3.2.1 Linearly Elastic Constitutive Models 30

3.2.2 Elasto–Viscoplastic Constitutive Model With Damage 31

3.3 Boundary Conditions 34

3.3.1 Support Conditions 34

3.3.2 Contact Condition 35

3.3.3 Adhesion 36

3.3.4 Shear Resistance 36

3.3.5 Initial Conditions 37

3.4 Variational Formulation 40
3.5 Solution Method for Elastic Contact Problems 42
3.6 Solution Method for Viscoplastic Contact Problems 44

4 Finite Element Analysis of Contact Problems with Friction 46
4.1 General Information About the 3D Finite Element Code 46
4.2 Formulation of a Structural Deformation Problem in the 3D Code 52

5 Basic Verification of Numerical Models 53

6 Verification of Numerical Models of Asperity 61
6.1 Elastic Sphere in Contact with a Rigid Flat 61
6.2 Experimental Studies of Models of Asperity 68
6.2.1 The Test Apparatus 68
6.2.2 Tests Results From the Above Apparatus 70
6.2.3 Deformation of Asperities Under a Larger Normal Load 70
6.3 Numerical Simulation of Experimental Measurements 76
6.3.1 Viscoplastic Uniaxial Stress State Numerical Test 76
6.3.2 Viscoplastic Cylindrical Asperity 79
6.3.3 Viscoplastic Custom Surface Model 79

7 A Simple Asperity-Based Contact Model 88

8 Conclusions and Research Forecast 90

9 References 91

List of Figures

2.1 A general classification of surfaces. 8
2.2 Flowchart for statistical homogenization of interfaces. 9
2.3 Contacting bodies and coupons near the contact interface subjected to an average stress vector of magnitude Σ. 12
2.4 (a) Profiles of opposing rough surfaces, and (b) microtopography of surfaces and the equivalent sum surface z. 13
2.5 Mechanical difference between asperity behavior and sum surface model. . . 15
2.6 Sampling of profilometric data. 18
2.7 Typical asperity: (a) isotropic random surface, (b) anisotropic random surface. 22
2.8 Sampling of arbitrary surface. 23
2.9 Accumulation of joint probability density $f_{z\kappa}(z_p, \kappa)$ for arbitrary surfaces. . . 25
2.10 Numerical integration of expectation value $E(X)$. 28
3.11 Penalty function for contact condition. 38
3.12 Surface asperity in contact with a rigid flat (a section). 39
3.13 A regularization function ϕ 40
3.14 Graphical presentation of construction of a series $u_0, u_1, u_2, \ldots$ convergent to a solution u^* of equation f (u) = 0. 43
4.15 A general finite element code structure 47
4.16 Vectorization and parallelizaton for groups and colors 49
4.17 Sample screen with interactive window environment 51
5.18 Adaptive timestepping algorithm for viscoelastoplastic evolution problems. . 55
5.19 Experimental and numerical results of uniaxial tension (incorrect value of Young modulus). 56
5.20 Experimental and numerical results of uniaxial tension of a specimen with corrected Young modulus 57
5.21 Cyclic loading test of the viscoplastic model - 10 cycles. 58
5.22 Relaxation test of the viscoplastic model 59
5.23 Creep test of the viscoplastic model 60
6.24 Refined mesh for the Hertz problem, w = .02, deformed configuration. Only boundary elements shown. 62
6.25 Isosurfaces of the vertical displacement for the Hertz problem, w=.02 63
6.26 Isosurfaces of the σ_{yy} for the Hertz problem, w=.02 65
6.27 Distribution of error indicator for the Hertz problem, w = .02 66
6.28 Comparison of theoretical and numerical results for the Hertz problem . . . 67

6.29 Comparison of theoretical and numerical results for the Hertz problem; (a) displacement versus contact area, and (b) displacement versus contact load . 69
6.30 A sketch of test apparatus (not to scale). 71
6.31 Different models of asperities studied experimentally. 72
6.32 Load-displacement curve for V-shaped asperity 73
6.33 Load-displacement curve for truncated asperity 74
6.34 Load-displacement curve for cylindrical asperity 75
6.35 A photograph of deformed asperity 76
6.36 A compressive stress-strain curve for aluminum 77
6.37 A tensile stress-strain curve for aluminum 78
6.38 Comparison of stress-strain relation behavior for uniaxial tension test. 81
6.39 Original discretization of the cylinder 82
6.40 Refined discretization of the cylinder 82
6.41 Numerical results for the cylinder 83
6.42 Comparison of numerical and experimental results for the cylinder 83
6.43 Original discretization of the second specimen (truncated V-shaped asperity) 84
6.44 Refined discretization of the second specimen 84
6.45 Deformation of the second specimen 85
6.46 Numerical results for the second specimen 86
6.47 Numerical and experimental results for the second specimen 87
7.48 Comparison of Greenwood-Williamson theory with numerical predictions; (a) load-separation curve and (b) load-area curve. 89

1 Introduction

Friction and rubbing of materials are among the most common phenomena in mechanics, present whenever two solid bodies come into contact. They are responsible for a variety of occurrences in everyday life. Some of them, such as tire traction, are very useful; others, like violin music, are asthetic and pleasing, and many others, such as noises, vibrations, and wear, are extremely unpleasant and dilatorius to mechanical systems. This common occurrence of friction and the diversity of its effects underscore the extreme importance of a deep understanding, modeling, and the control of friction phenomena. It is well known, however, that the phenomena of contact and friction of solid bodies are among the most complex and difficult to model of all mechanical events, primarily due to the complex structure of engineering surfaces, the severe elasto-plastic deformation, damage, heat generation, atomic-range interactions that take place on typical contact surfaces, the presence of contaminants, lubrication, and even chemical reactions on these contact surfaces.

Efforts toward an understanding of frictional phenomena and of modeling friction began with the historical works of Amontons [2] and Coulomb [32] over two centuries ago. Since then, an extensive body of experimental and theoretical work has accumulated on general tribology and a good empirical understanding of the subject exists today. However, the progress in formulating a theoretical background and models of frictional interfaces have been much slower to evolve than experimental investigations. Although considerable progress in this direction has been made in recent years, there are still several issues that need to be resolved in order to model friction and predict frictional phenomena with practical reliability. One of the most difficult problems encountered is the estimation of material constants occurring in the new constitutive models of frictional interfaces. These difficulties reflect an urgent need for constructing new constitutive models of contact and friction and for estimating the necessary material coefficients.

Presently there are two basic approaches for the development of mechanical constitutive models of friction and two resulting types of frictional interface models which appear to be the most promising. There are:

1. phenomenological models based primarily on experimental observations, and
2. asperity-based models, formulated via a theoretical analysis and statistical homogenization of the microscale deformation of surface asperities in contact with an opposing surface.

Unfortunately, to date none of these approaches has produced completely satisfactory results. It is well known that experimental results depend strongly on the characteristics of the test apparati, so the results of different tests on the same sample can be considerably scattered. Moreover, these macroscopic experimental measurements do not provide sufficient insight into the nature of the phenomena occurring on the contacting surfaces, severity of the deformation, propagation of damage, etc. Such an insight can be provided by asperity-based models, which are based on the microscale analysis of deformation and the relative

sliding of surface asperities. However, predictions made using classical or existing asperity-based models are not generally applicable to the environments normally met in engineering applications. The main reason is that these classical models are based on analytical, closed-form solutions of the deformation of a surface asperity, which require gross simplifications of geometry of the asperity and of the constitutive models of the contacting materials (elastic, plastic, or at most elasto-plastic).

1.1 Summary of Objectives of the Project

In this project, a new approach for constructing constitutive models of frictional interfaces is under development, which promises to provide a realistic link between microscale phenomena occurring on contacting surfaces and macroscale phenomenological models of the interface. This approach involves the use of special finite element methods in the modeling of complex deformations of asperities of arbitrary shape, with realistic nonlinear constitutive models of the contacting materials. The technical approach for the evaluation of the microasperity-based models of contact and friction consists of two stages:

1. Apply the finite element technique to the analyze the nonlinear mechanical responses of surface asperities of different heights, shapes, and with general viscoelastoplastic material properties and with material damage.

2. Apply statistical homogenization techniques to evaluate macroscopic, phenomenological constitutive models of the interface.

The approach being developed here should provide a means for generating a variety of new and useful models of frictional interfaces. Depending on the selected level of complexity of the model of the asperity, a viscoelastoplastic, hyperelastic, or brittle material can be considered, evolution of damage of the surface can be modeled, and effects of lubrication and surface contamination can be taken into account.

1.2 Research Progress

The results of the first year of effort on this project included a complete formulation of the theory and a corresponding software package for statistical homogenization of the interface parameters.

In the second year of the project the effort has focused on the development of a finite element code for modeling the nonelastic surface asperities, as well as on the design and performance of the verification experiments, followed by initial verifications of the numerical models for the surface asperities. In particular, the following tasks were completed during the second year:

1. development of a three-dimensional adaptive finite element code for the analysis of surface asperities in contact with opposing surfaces. The starting point for this effort

was an existing in-house finite element kernel, which was extended and customized to satisfy the objectives of this project. Our effort during the last year has been focused on the implementation of elastic and viscoplastic three-dimensional solid models, the development of contact and sliding resistance algorithms and on extensions of the graphics, user interface and adaptive algorithms specifically related to this project.

2. Design, development and performance of Phase I of the verification experiments, oriented toward testing the numerical models of nonelastic surface asperities in contact with a rigid flat.

3. Verification of the finite element asperity models by comparison with analytical and experimental results. The numerical predictions were compared with existing analytical solutions for selected simplified cases (Hertz problem) and with the experimental results obtained for fully nonlinear, elastoplastic contact problems.

4. Introductory tests of the complete homogenization procedure, which are based on a combination of numerical models of the asperity with statistical homogenization, to predict the response of random surfaces to contact and friction loads. Comparisons with existing simplified asperity-based models (Greenwood-Williamson [44]).

1.3 Outline of the Report

This report presents the results of the second year of effort on this project, as well as a brief compilation of the most important results of year I. In particular, Section 2 presents a study of statistical methods of homogenization of interface parameters. Of particular interest are such issues as extraction of surface statistics from profilometric data, calculation of an asperity distribution for random surfaces, and the practical calculation of expected macroscopic parameters from a microasperity analysis. In Section 3, a detailed formulation of the boundary value problem representing the deformation of a surface asperity is developed. This formulation includes elastic and viscoelastoplastic material properties, damage modeling, a nonpenetration condition on the contact plane, and boundary conditions resulting from adhesion forces and sliding resistance of the interface. Section 4 presents the background of the adaptive finite element technology developed for the analysis of the deformation of a microasperity. A general background of the *hp*-adaptive finite element methodology is discussed in this section, together with a detailed presentation of the numerical algorithms used for the solution of elastic and viscoplastic contact problems.

The above theoretical part of the report is followed by examples and tests of the microasperity analysis. In particular, Section 5 presents some basic tests of numerical models of viscoplastic material behavior. Then, in Section 6, finite element models of asperity response are verified by comparison with the Hertz solution and with experimental measurements performed for custom-shaped asperities. This section is followed by an introductory example of a complete homogenization, and comparison is made with the classical Greenwood-Williamson contact model. Finally, in Section 8, a research forecast is presented for the third year of the project.

1.4 Presentations and Publications

Our research related to new models of contact and friction was presented at the 113th ASME Winter Annual Meeting, Anaheim, California, November 8-13, 1992.

The following papers were published or submitted for publication in 1992:

1. Tworzydlo, W.W., Becker, E.B., and Oden, J.T., "Numerical Modeling of Friction-Induced Vibrations and Dynamics Instabilities", in **Friction-Induced Vibration, Chatter, Squeal, and Chaos**, Ibrahim, R.A. and Soom, A., editors, ASME Publications, New York, 1992, pp. 13-32.

2. Lee, C. Y., and Oden, J.T., "Theory and Approximation of Quasistatic Friction and Contact Problem", to appear in Comp. Meth. Appl. Mech. Engng., 1992.

3. Oden, J.T., Ainsworth, M., and Lee, C.Y., "Local A Posteriori Error Estimators for Variational Inequalities," *International Journal for Numerical Methods in Partial Differential Equations*, (in press).

4. Oden, J.T., Lee, C.Y., and Ainsworth, M., "Local A Posteriori Error Estimates and Numerical Results for Contact Problems and Problems of Flow Through Porous Media", *Nonlinear Computational Mechanics–State of the Art*, P. Wriggers and W. Wagner, eds., Springer-Verlag, (in press)

5. Lee, C.Y. and Oden, J.T., "A Posteriori Error Estimation of *hp*- Finite Element Approximations of Frictional Contact Problems with Normal Compliance," *International Journal of Engineering Science*, (in press).

2 Asperity–Based Models of Contact and Friction

One of the major missions in tribology is the development of constitutive models of frictional interfaces. Throughout the decades a variety of approaches and types of models have been developed. They can be classified into several groups, including:

- models based on experimental observations,
- microasperity–based models,
- phenomenological models developed from basic principles of mechanics, and
- models of the type related to plasticity theory.

It should be noted here that this distinction is only of a general nature and most of the models presented in the literature combine, in some sense, features of more than one of these groups.

In this project we focus on the development of new asperity–based models of contact and friction. These models are aimed at the development of constitutive equations of frictional interfaces via the statistical homogenization of the deformation of surface asperities subject to contact with an opposing surface. The advantage of the asperity–based models is that they provide good quantitative insight into the phenomena occurring at the interface and predict additional information hardly available from the experiment–based laws, such as the surface plasticity indices, microfracture indices, etc.

The first contact model that was constructed to predict the true contact area can be found in a paper by Abbott and Firestone [1], in which the contact surface was simulated in a network of spheres that are truncated upon indentation into a hard flat. By knowing the hardness of the softer of the two materials in contact, an estimate of the true contact area could be made, assuming perfectly plastic deformations.

An important advance in development of asperity–based models of contact is represented by the pioneering paper of Greenwood and Williamson [44], in which the rough surfaces were viewed as a randomly distributed population of elastic asperities with randomly distributed asperity heights. Each asperity was assumed to be spherical and elastic and its deformation properties governed by the Hertz solution for elastic contact. Experimental evidence was provided to support the assertion, now widely held by tribologists, that for [illegible]ly isotropic engineering surfaces, a Gaussian distribution of asperities heights generally exists. In such models, there are no microfrictional effects on the asperities, such effects leading to second–order changes in contact pressure, a result established nearly two decades earlier by Mindlin [63]. In a related paper, Greenwood and Tripp [43] showed that contact of two rough surfaces with Gaussian distributions of asperity heights on which asperity contacts were misaligned was equivalent to a single elastic surface with a Gaussian distribution of asperity heights impending on a rigid flat. The use of such statistical representations of surface topography has since become a popular approach in modeling both elastic and inelastic contact.

The Greenwood-Williamson model was based on the assumption that only the asperity height was a random variable, and that the radius R of each peak was constant. Several generalizations of such random topography models appeared in the literature of the 1970s. The paper of Whitehouse and Archard [99] extends the random–asperity models to include random heights and curvatures, and Nayak [67] provided a general approach to random surface modeling using notions of joint probability distribution functions. In this same vein, we mention the work of Bush, Gibson, and Thomas [23], who derived a joint probability distribution density function for random asperity heights and curvatures of a random population of elliptic paraboloids in elastic contact with a smooth rigid flat.

Such random–microtopography models that employ a deterministic function for asperity peak shapes are called *asperity models*. One source of possible inconsistency in such models has to do with the fact that a Gaussian distribution of asperity heights and curvatures for a given asperity shape may lead to a non–Gaussian cumulative probability distribution of the surface height, an unrealistic result for most "engineering surfaces." This problem was addressed by Hisakado [48] and Hisakado and Tsukizoe [49], by assuming a Gaussian PDF (Probability Density Function) for surface heights, with a given deterministic asperity shape, and then deriving the PDF for peak heights. Hisakado [48] assumed a paraboloidal asperity shape and Hisakado and Tsukizoe [49] a conical shape. Francis [41] points out that the Hisakado models may lead to unrealistic PDFs for asperity heights, since they may be strongly dependent on the asperity shape and may become negative for paraboloidal and conical shapes.

Extensions of asperity–based models to microcontact deformation laws involving elastoplastic deformations were first contributed by Hisakado [48]. Halling and Nuri [46] account for plastic deformation of the interface by assuming that a rough surface deforms elastically while contacting a nonlinearly elastic flat, representing strain–hardening, with each microcontact defined by a fully–plastic spherical indentation. Significant generalizations of these types of asperity models can be found in the detailed studies of Francis [41], who introduces the notion of the *sum surface*, discussed later in the present work. This enables one to model Gaussian engineering surfaces with asperity shapes that a paraboloidal only at their vertices, but which have random heights and curvatures, using the joint PDF of Nayak [67]. Moreover, Francis [41] also takes into account elastic and fully plastic deformations, with strain–hardening, using functions determined empirically from spherical indentations of various metals. We also mention that an extension of the Greenwood-Williamson model of spherical asperities with Hertzian elastic contact, constant radii, and random heights to cases in which a transition to perfectly plastic deformations occur was recently proposed by Chang, Etsion, and Bogy [26–28].

We note that most of the references cited above dealt with attempts to model either contact without sliding motion, or purely static or quasi–static friction effects.

The asperity–based models of frictional interfaces are constructed in five basic steps:

1. Perform a statistical analysis for the surface profile (profiles),

2. calculate the surface statistics (distribution of surface height, gradient, and curvature) from one or more set of profile data,

3. calculate, from surface statistics, the probability distribution and density of surface asperities of different heights and (possibly) peak shapes,

4. calculate, by analytical or numerical methods, responses of representatives of a family of surface asperities of different shapes to prescribed load programs,

5. calculate, from asperity data and the probabilistic distribution of asperities, the expected values of the interface response (normal and tangential forces, damage, etc.) to prescribed load programs. This response characterizes constitutive properties of the interface.

Several variations of this basic scheme may be derived for random and deterministic surfaces, isotropic or anisotropic finish, etc. In this case a general classification of surfaces presented (after Nayak [66]) in Fig. 2.1 is helpful.

For practical purposes, it is reasonable to consider the following three classes:

(i) Gaussian isotropic surfaces,

(ii) Gaussian anisotropic surfaces, and

(iii) other surfaces, in particular deterministic surfaces obtained by special finishing techniques.

The flowchart illustrating the homogenization procedure for these three groups is presented in Fig. 2.2.

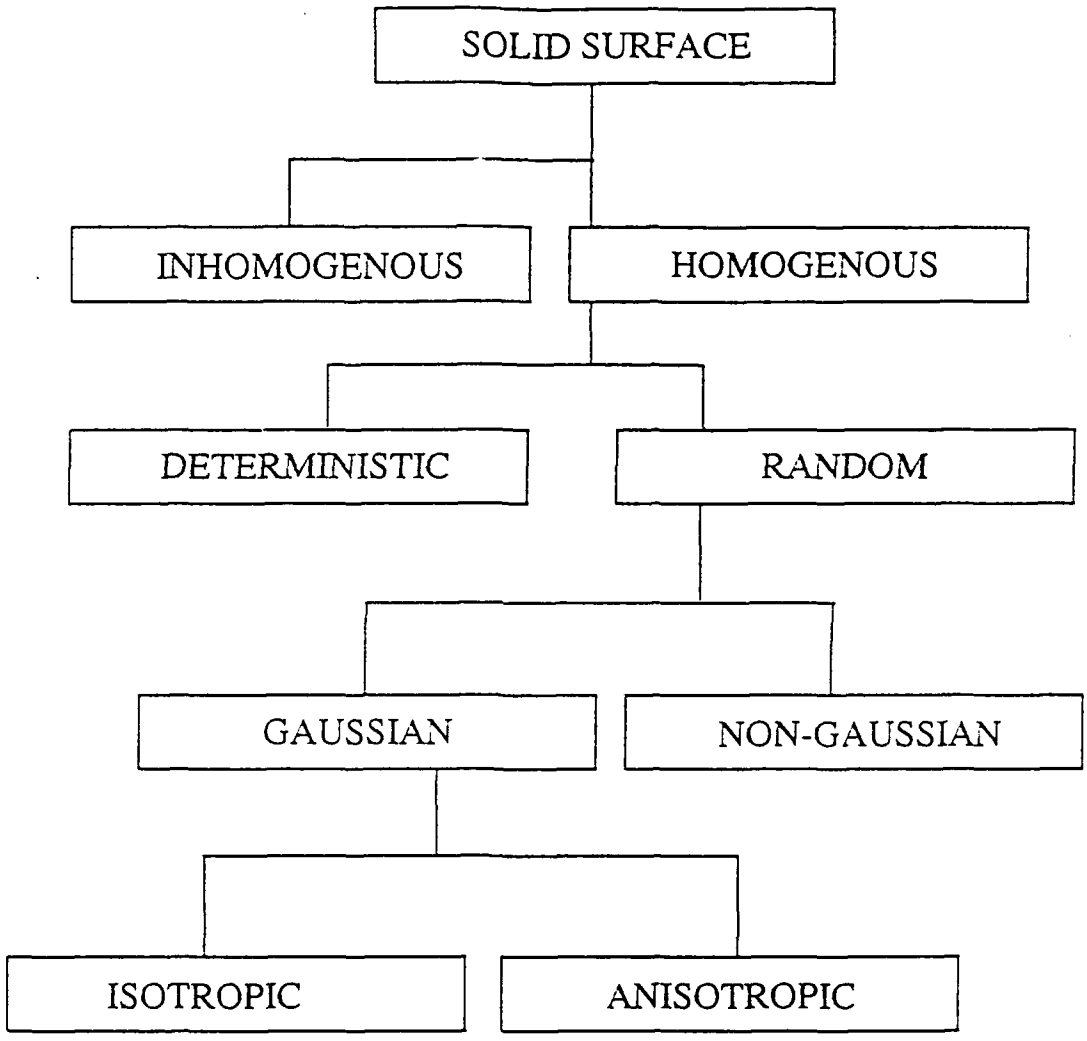

Figure 2.1: A general classification of surfaces.

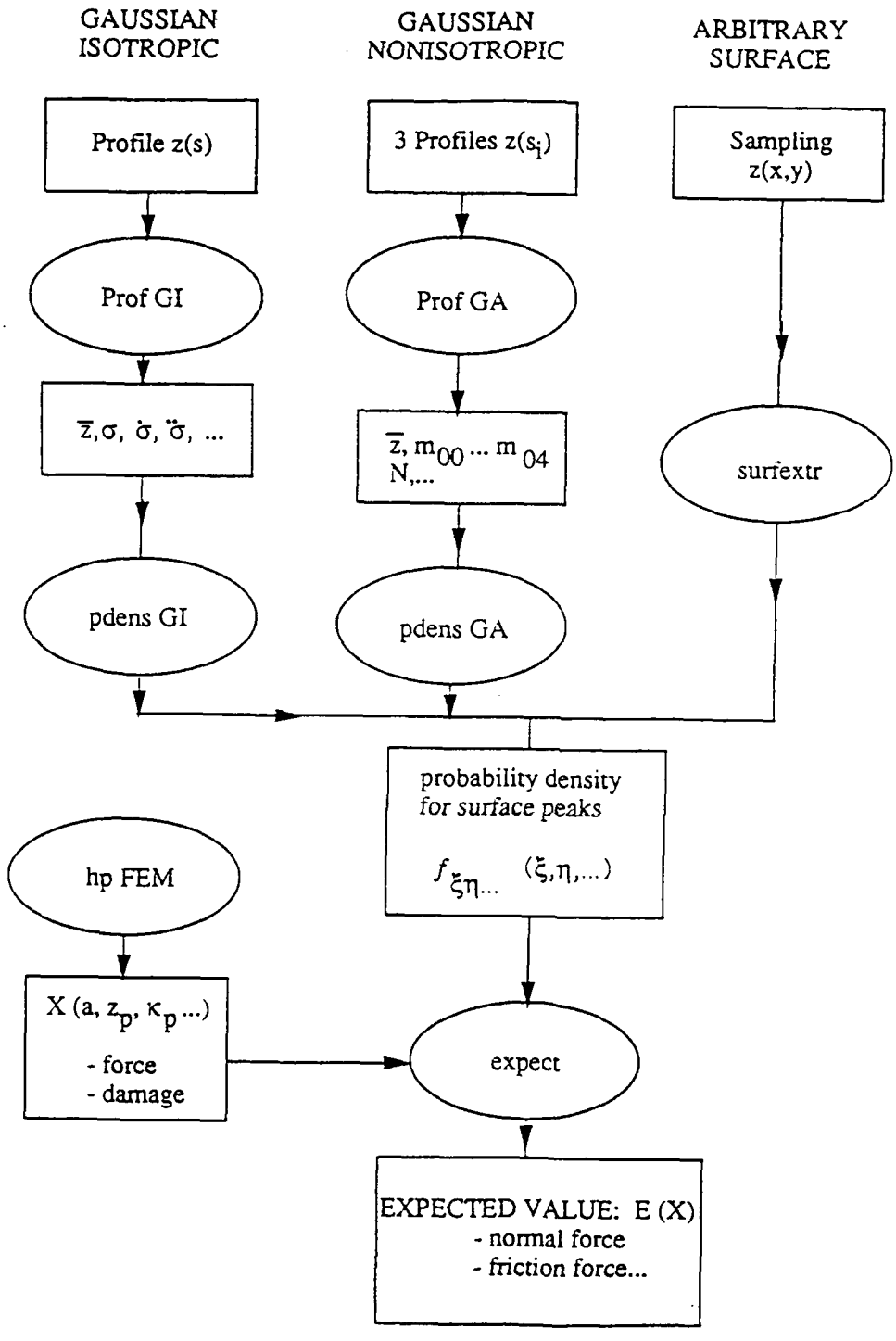

Figure 2.2: Flowchart for statistical homogenization of interfaces.

The details of these procedures will be discussed later. Here it is important to observe that for Gaussian isotropic surfaces it suffices to gather profilometric data along only one profile on the surface and to consider asperities of axisymmetric peak shapes. For Gaussian *anisotropic* surfaces, however, one needs at least three nonparallel profiles and asperities of different principal curvatures and orientations. Finally, for non–random surfaces, a full two–dimensional map $z = z(x, y)$ of the surface may be needed, and asperities may have various deterministic shapes, depending on the surface finish.

2.1 Microstructure of the Frictional Interface

We begin by considering the contact of two deformable bodies, I and II, over a nominal contact area A_0, as illustrated in Fig. 2.3. An element of unit nominal contact area is isolated for study, as indicated in the figure. The average stress vector Σ over the unit contact area has components of force P and Q normal and tangential to the unit area, respectively. The situation is equivalent to that of two typical coupons of surface material, one taken from the material near the contact surface of each body, pressed together with a force P normal to the tangent plane at the center of the coupon interface and simultaneously subjected to a shear force Q tangent to the plane. The bulk deformations of bodies I and II are ignored, our aim being only to characterize the mechanical properties of the contact interface. The nominal unit surfaces in contact are, for the present, assumed to be initially flat and parallel to one another.

It is standard practice to depict the approximate profile of rough engineering surfaces with a profilometer or stylus, drawn across the surface, which generally yields a jagged profile with an exaggerated vertical scale of the type shown in Fig. 2.4(a). We consider two such opposing surfaces 1 and 2 which are to ultimately come in contact. Refrence planes defining the mean asperity height of each surface profile are established, and we characterize the shape of each profile by introducing functions z_1 and z_2, given the height of asperities above the respective reference planes, i.e., the functions $z_i = z_i(x, y), i = 1, 2$, with (x, y) a point in the parallel mean–height reference planes, define the profiles of the rough material surfaces 1 and 2, respectively. The distance h between planes is the separation of the surfaces, and the distance between actual opposing material points is denoted s. Thus, at a point (x, y) on the reference plane, we have

$$s = h - z \tag{2.1}$$

where z is the *sum surface* (see Francis [41]),

$$z = z_1 + z_2$$

Francis has pointed out that, from the fact that the sum z of the surface heights appears in the geometric relation (2.1), the situation is equivalent to that of a single deformable surface of height $z = z_1 + z_2$ approaching a rigid flat, as suggested in Fig. 2.4(b).

Clearly, the undeformed surfaces overlap whenever

$$s(x, y) < 0$$

As the normal load pressing the surfaces together increases, the separation h decreases and at each minimum of the function s a microcontact nucleates and expands due to local deformation of the surfaces.

It is of importance to note that arguments presented by Francis [41] are of a purely geometric nature. From a mechanical point of view, two major objections can be raised here:

1. The sum of two asperities (say, spherical) in contact with a rigid flat is not mechanically equivilant to two spheres in contact—see Fig. 2.5.

   In particular, the distance–force curves $P = P(a)$ for the two models are different. Moreover, the "asperity" peak on the sum surface corresponding to two spheres is not spherical. It can be shown, however, using the Hertz solution, that these differences vanish when the ratio of asperity radius R to the contact radius r goes to infinity (relatively smooth surfaces at moderate loads).

2. In the case of contact with friction, the sum surface approach will not model the friction component due to the interlocking of asperities. Similarly as above, the importance of this effect diminishes with increasing surface smoothness.

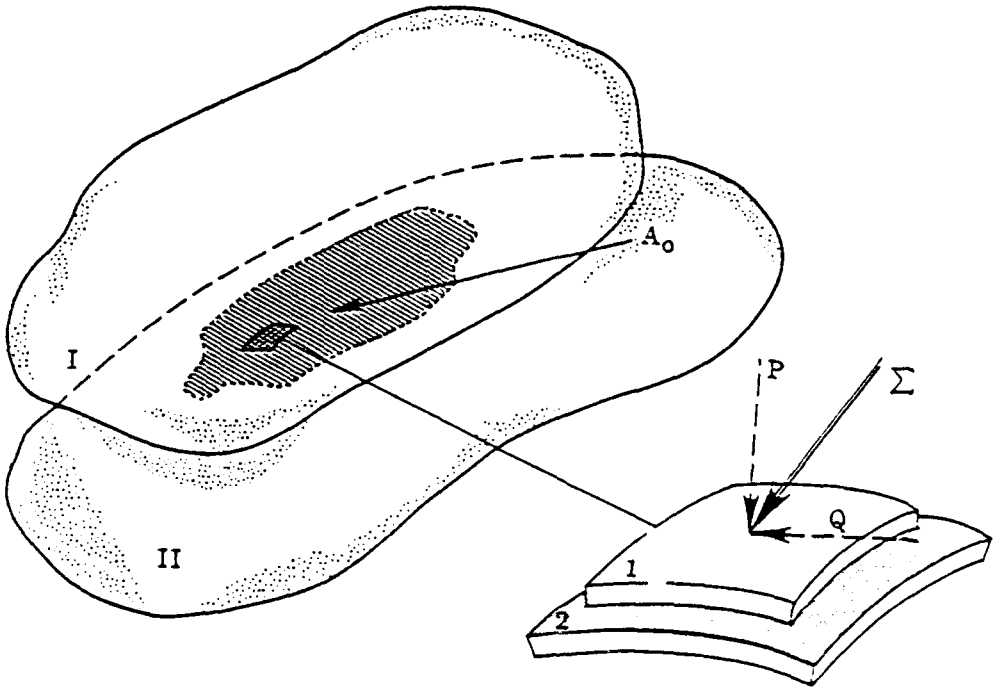

Figure 2.3: Contacting bodies and coupons near the contact interface subjected to an average stress vector of magnitude Σ.

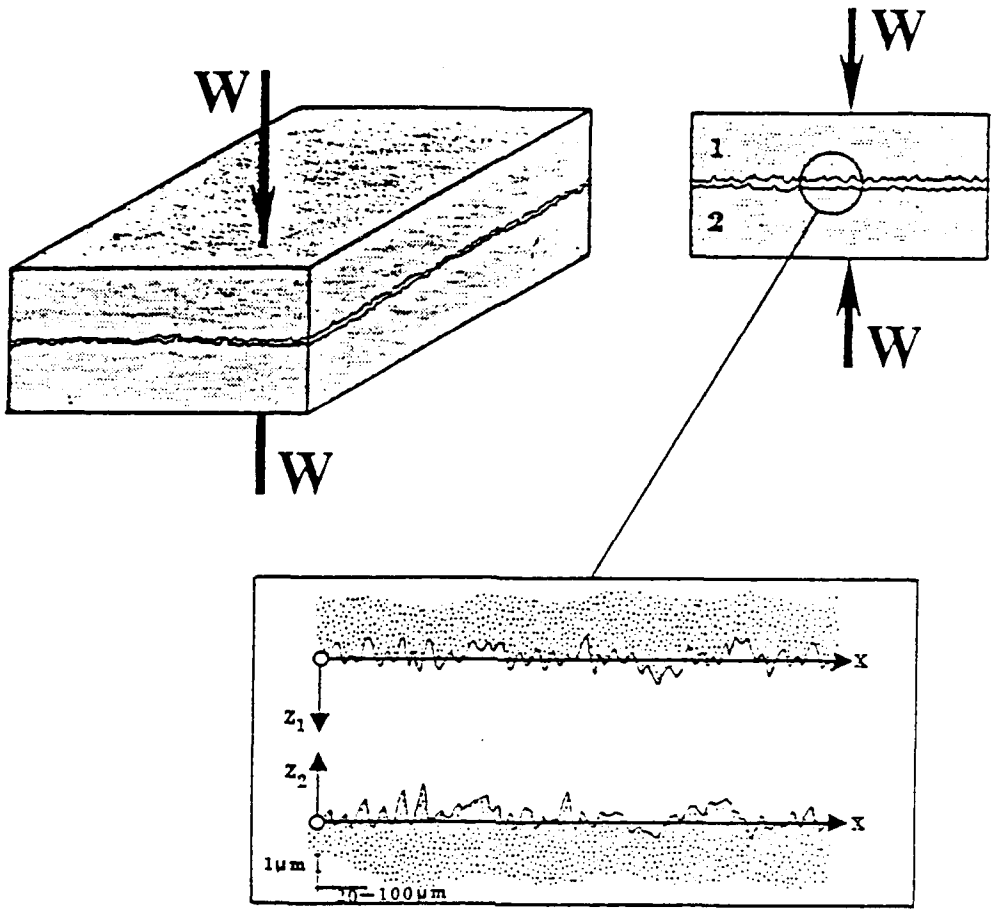

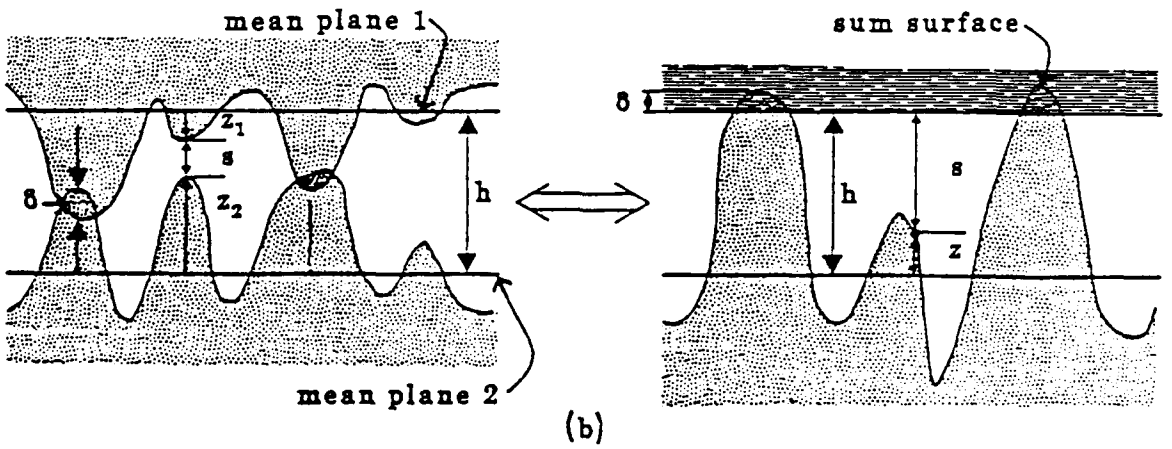

Figure 2.4: (a) Profiles of opposing rough surfaces, and (b) microtopography of surfaces and the equivalent sum surface z.

In view of these remarks, the sum surface approach seems to be correct and justified for typical engineering surface finishes at moderate loads. Note that this condition is also required for the satisfaction of the assumption that separate microcontacts do not interact mechanically and that contacts do not merge.

It is well known in tribology that techniques used to produce engineering surfaces usually produce a Gaussian distribution of the surface heights z_i. Moreover, the sum z of two Gaussian surfaces is also Gaussian; indeed, Tallian [89] points out that if z_1 and z_2 are not exactly Gaussian, their sum surface will be closer to Gaussian than either surface. If the shape of an asperity is assumed to be paraboloidal, as have been done by several authors, then the peak heights and curvatures are correlated random variables, with the result that a Gaussian distriution of heights and curvatures may lead to a cumulative probability distribution of surface heights which is non-Gaussian. This issue has been studied by Hisakado [48], Hisakado and Tsukizoe [49], and by Francis [41], who assert that if the peak shape is paraboloidal only at its vertex, then the ensemble of peaks can be made to conform to the Gaussian distribution.

2.2 Statistics of a Random Surface

There are several methods of homogenization that can be found in the literature. Few have been effectively used for describing nonlinear frictional phenomena. As one possible technique we describe a general approach inspired by the works of Lonquet-Higgins [56–58], Nayak [67], and Francis [41]; see also Chang, Etsion, and Bogy [26–28]. To fix some of these ideas, we note that for a given asperity profile, one defines the autocorrelation function $C(X,Y)$ for the random variable $z = z(x,y)$ (the surface height),

$$C(X,Y) = \lim_{\substack{a\to\infty \\ b\to\infty}} \frac{1}{ab}\int_0^a \int_0^b z(x,y)z(x+X,y+Y)dx\ dy$$

and the power spectral density $P(k_x,k_y)$ as its Fourier transform,

$$P(k_x,k_y) = \frac{1}{4\pi^2}\int_{-\infty}^{\infty}\int_{-\infty}^{\infty} C(X,Y)\exp\left[-i(Xk_x+Yk_x)\right]dX\ dY$$

The power spectral moments are

$$m_{ij} = \int_{-\infty}^{\infty}\int_{-\infty}^{\infty} P(k_x,k_y)k_x^i k_y^j\ dk_x\ dk_y \tag{2.2}$$

and the r.m.s. roughness σ is the variance,

$$\sigma^2 = m_{00} = C(0,0) = \int_{-\infty}^{\infty}\int_{-\infty}^{\infty} P(k_x,k_y)\ dk_x\ dk_y$$

A convenient representation of a continuous random surface is of the form [57,67]:

$$z(x,y) = \sum_{n=1}^{\infty} C_n \cos\left(xk_{xn} + yk_{yn} + \varepsilon_n\right) \tag{2.3}$$

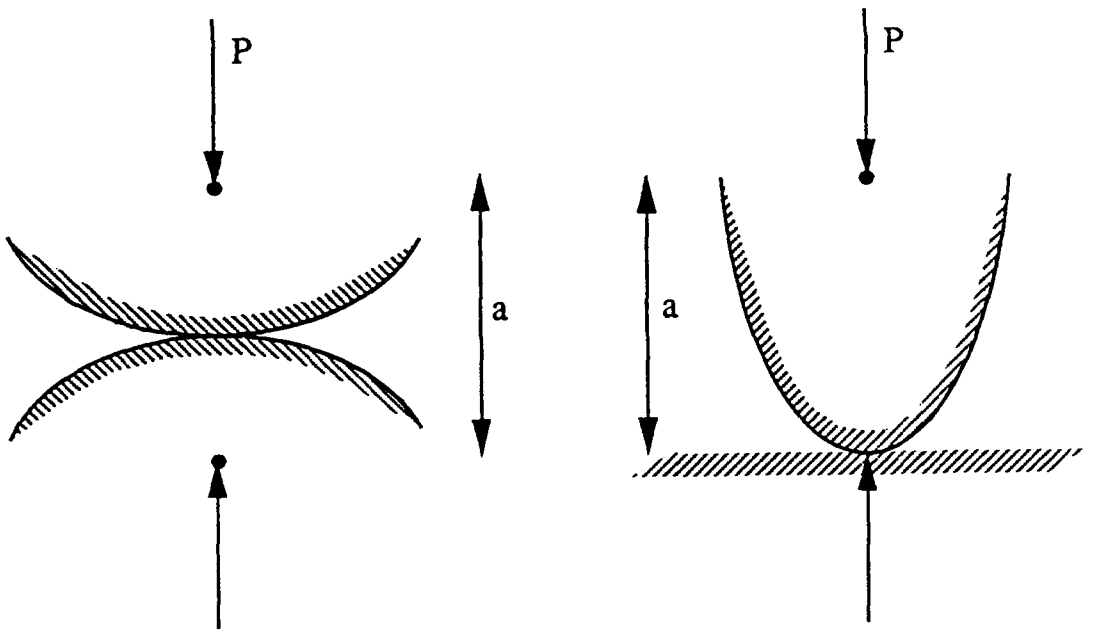

Figure 2.5: Mechanical difference between asperity behavior and sum surface model.

where amplitudes C_n, wave numbers k_{xn} and k_{yn}, and phase ε_n are random variables. It is assumed that there are an infinite number of wave vectors in any area $dk_x dk_y$ and that ε has a uniform probability density in the range $(0, 2\pi)$. The power spectral density is related to representation (2.3) by

$$P(k_x, k_y)\, dk_x dk_y = \frac{1}{2} \sum_{\Delta k} C_n^2$$

the summation being over all terms with (k_{nx}, k_{ny}) lying in the area $dk_x dk_y$ around (k_x, k_y). The power spectral moments m_{pq} can then be expressed as

$$m_{pq} = \frac{1}{2} \sum_n k_{xn}^p k_{yn}^q C_n^2 \tag{2.4}$$

Similar definitions and representations as above can be introduced for arbitrary surface profile $z(s)$, s being a parameter on the surface. Of particular interest are spectral moments of a profile m_0, m_2, and m_4.

2.3 Calculation of Surface Statistics From Profile Data

Information about the statistics of a two–dimensional surface can be effectively obtained from profilometric data for one or more profiles on the surface. This greatly simplifies the homogenization procedure because both experimental measurements and statistical post-processing are much easier for one–dimensional profiles. In this section we discuss details of these computations for both isotropic and anisotropic surfaces.

2.3.1 Profiles on Gaussian Isotropic Surfaces

It was shown by Lonquet-Higgins [56, 57] and Nayak [67] that for random isotropic surfaces the mean surface height and non-zero spectral moments are expressed in terms of mean profile height and profile spectral moments:

$$\begin{aligned} \overline{z}_{\text{surface}} &= \overline{z}_{\text{profile}} \\ m_{00} &= m_0 \\ m_{20} = m_{02} &= m_2 \\ 3m_{22} = m_{04} = m_{40} &= m_4 \end{aligned}$$

Therefore, in order to calculate surface statistics it suffices to perform measurements for one profile on the surface. The spectral moments of the profile can be calculated in several ways:

- from the definition as moments of power spectral density
- from statistical postprocessing (sampling) of profile data
- from counting zeros and extrema of the profile

Calculation from definition:

$$m_i = \int_{-\infty}^{\infty} \Phi(k) k^i dk$$

where k is a wave number and $\Phi(k)$ is a power spectral density. This particular method is rather expensive because it requires evaluation of the autocorrelation function and the power spectral density as its Fourier transform.

It is much easier to calculate profile spectral moments if one reinterprets them as standard deviations $\sigma, \dot{\sigma}, \ddot{\sigma}$ of profile heights z, slopes $\dot{z}$, and curvatures $\ddot{z}$, respectively:

$$\begin{aligned} m_0 &= \sigma^2 \\ m_2 &= \dot{\sigma}^2 \\ m_4 &= \ddot{\sigma}^2 \end{aligned}$$

Assuming that the profile data was sampled at n points separated by the interval Δs (see Fig. 2.6), the profile statistics can be calculated from the following sampling formulas [16]:

(a) mean height, slope and curvature:

$$\begin{aligned} \overline{z} &= \frac{1}{n}\sum_{i=1}^{n} z_i \\ \overline{\dot{z}} &= \frac{1}{n}\sum_{i=1}^{n} \dot{z}_i \\ \overline{\ddot{z}} &= \frac{1}{n}\sum_{i=1}^{n} \ddot{z}_i \end{aligned}$$

(b) variations of height, slope and curvature:

$$\begin{aligned} \sigma^2 &= \frac{1}{n-1}\sum_{i=1}^{n} (z_i - \overline{z})^2 \\ \dot{\sigma}^2 &= \frac{1}{n-1}\sum_{i=1}^{n} \left(\dot{z}_i - \overline{\dot{z}}\right)^2 \\ \ddot{\sigma}^2 &= \frac{1}{n-1}\sum_{i=1}^{n} \left(\ddot{z}_i - \overline{\ddot{z}}\right)^2 \end{aligned}$$

The values of first and second derivatives can be calculated from a second order approximation of the profile shape, discussed in Appendix A.1 in reference [94]. Note that the mean slope and mean curvature of a perfect Gaussian profile should be zero. For real profiles they may slightly differ from zero. Also note that for the above procedure, shorter wavelengths can be automatically filtered out by appropriate selection of the sampling interval Δs.

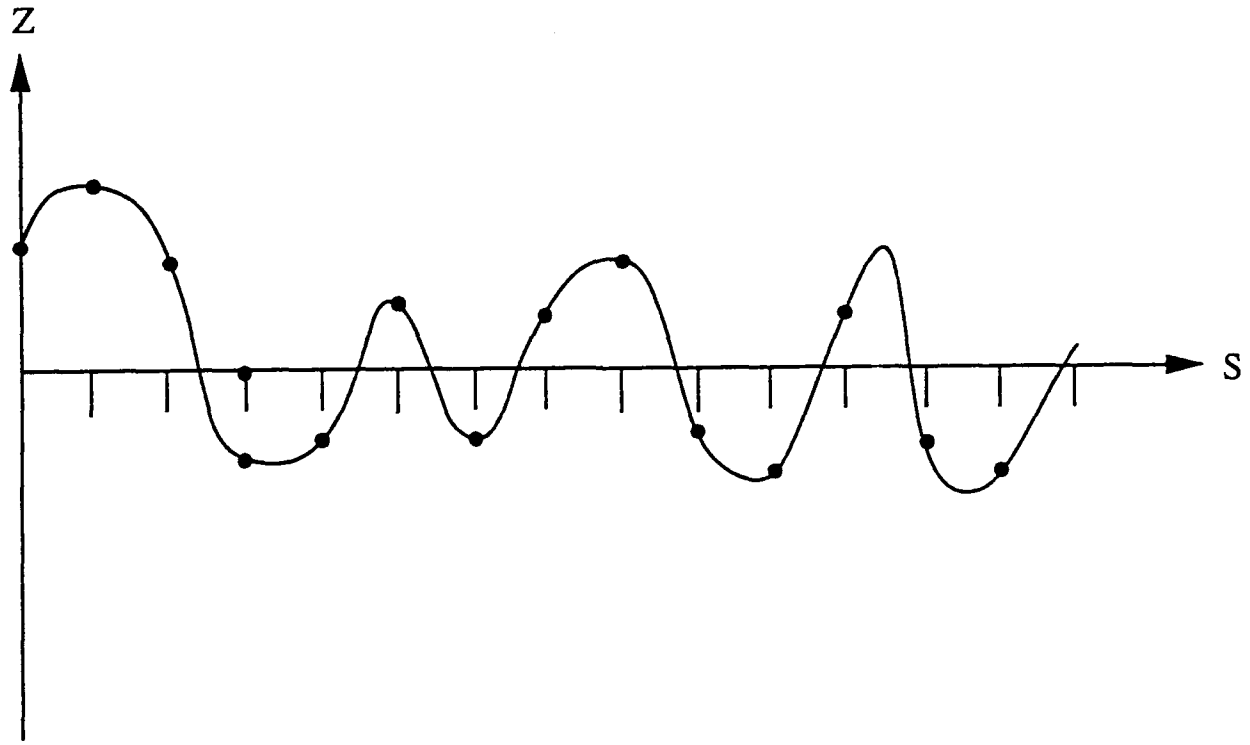

Figure 2.6: Sampling of profilometric data.

An ingenuous alternative way of calculating m_2 and m_4 was proposed by Lonquet-Higgins [57], see also Nayak [67]. The densities of zeros and of extrema of the profile are expressed through spectral moments as:

$$D_{\text{zero}} = \frac{1}{\pi}\left(\frac{m_2}{m_0}\right)^{\frac{1}{2}} = \frac{1}{\pi}\frac{\dot{\sigma}}{\sigma}$$

$$D_{\text{extr}} = \frac{1}{\pi}\left(\frac{m_4}{m_2}\right)^{\frac{1}{2}} = \frac{1}{\pi}\frac{\ddot{\sigma}}{\dot{\sigma}}$$

By zero point we mean here the point where $z(s) = \bar{z}$. The counting of zeros and extrema can be performed simultaneously with the sampling procedure described above. Then, after calculation of the variation σ, variations of slopes and curvatures can be obtained as:

$$\dot{\sigma} = \pi\sigma D_{\text{zero}}$$
$$\ddot{\sigma} = \pi\dot{\sigma} D_{\text{extr}}$$

In practice, both sampling and counting methods can be easily implemented in the same sampling program. Practical comparisons of these procedures are presented in our previous report [94].

Another parameter necessary for the homogenization procedure is a density of peaks on the surface, defined for homogenous surfaces as:

$$D_p = \lim_{\substack{dx\to\infty \\ dy\to\infty}} \frac{N_p}{dA}$$

where $dA = dx\ dy$ is the surface area and N_p is the number of asperity peaks within this area. The density of surface peaks can be calculated from profile parameters [67] as:

$$D_p = \frac{1}{6\pi\sqrt{3}}\frac{m_4}{m_2}$$

2.3.2 Profiles on Gaussian Anisotropic Surfaces

Basic statistical information for anisotropic random surfaces consists of nine moments of the power spectral density: $m_{00}, \ldots, m_{40}$. However, since the properties of the surface do not depend on the orientation of the x, y axes, only certain invariant combinations appear in the probability distribution of the surface statistics [58,67]. These invariants are:

1. m_{00}
2. $m_{02} + m_{20}$
3. $m_{20}m_{02} - m_{11}^2$
4. $m_{40} + 2m_{22} + m_{04}$

5. $m_{40}m_{04} - 4m_{13}m_{31} + 3m_{22}^2$

6. $(m_{40} + m_{22})(m_{22} + m_{04}) - (m_{31} + m_{13})^2$

7. $\left\{m_{40}(m_{22}m_{04} - m_{13}^2) - m_{31}(m_{31}m_{04} - m_{13}m_{22}) + m_{22}(m_{31}m_{13} - m_{22}^2)\right\}$

From three profiles in three nonparallel directions $\theta_i, i = 1,2,3$ nine parameters can be defined: $m_{0(i)}, m_{2(i)}, m_{4(i)}, i = 1,2,3$. However, since $m_{0(1)} = m_{0(2)} = m_{0(3)}$, then these three profiles define seven constants—invariants described above. This means that three nonparallel profiles suffice to define surface statistics for Gaussian anisotropic surfaces. (Detailed equations will not be derived here.)

2.4 Calculation of Asperity Statistics From Surface Statistics

The primary idea of asperity-based interface models is to calculate interface parameters (normal force, friction force, etc.) for a family of asperities of certain deterministic shapes and to obtain expected values of these parameters for the interface from a statistical distribution of asperities. This requires the calculation of probability density of surface asperities. For random surfaces, this probability density can be expressed in terms of surface statistics. This problem will be addressed in this section.

2.4.1 Asperity Statistics for Gaussian Isotropic Surfaces

For Gaussian isotropic surfaces two random variables are assumed to govern the distribution of asperities: asperity peak height z_p and mean curvature κ. The joint probability density function of these parameters was derived by Nayak [66] and recast in a different form by Francis [41]. Here we present the formula due to Francis:

$$f_{\xi\eta}(\xi,\eta) = \frac{\sqrt{3}}{\pi\sqrt{1-\beta^2}}\left\{\eta^2 - 1 + e^{-\eta^2}\right\} e^{\frac{-1}{2(1-\beta^2)}\left(\xi^2 - 2\beta\xi^2\eta + \eta^2\right)}$$

where

$$\xi = \frac{z_p}{\sigma} \qquad \text{nondimensional peak height}$$

$$\eta = \sqrt{1.5}\,\frac{\kappa}{\ddot{\sigma}} \qquad \text{nondimensional peak curvature}$$

$$\beta = \sqrt{1.5}\,\frac{\dot{\sigma}^2}{\sigma\ddot{\sigma}} \qquad \text{wavelength spectrum parameter}$$

The wavelength spectrum parameter varies for random surfaces between 0 and 1; zero corresponds to the widest wavelength spectrum (asperity heights and wave numbers are not correlated), and one corresponds to the narrow spectrum (longer asperities have bigger heights). Note that deterministic surfaces may have $\beta > 1$, see Section 2.6.1.

2.4.2 Asperity Statistics for Gaussian Anisotropic Surfaces

For Gaussian anisotropic surfaces the representative asperities are no longer of axisymmetric shape. Instead, one should consider asperities with elliptic horizontal cross sections, shown in Fig. 2.7b.

The peaks of these asperities can be characterized by four parameters:

1. z_p — peak height
2. κ_1, κ_2 — principal curvatures
3. α — orientation of the main axis of curvature

Equivalently, peak height z_p and three Cartesian curvatures (second derivatives of z) κ_{xx}, κ_{xy}, κ_{yy} can be used. The joint probability density function based on all these parameters should be defined as $f_{\xi\eta_1\eta_2\alpha}\ (\xi, \eta_1, \eta_2, \alpha)$. In principle, this function can be defined from surface statistics, in particular spectral moments $m_{00}, \ldots, m_{40}$ [58,67]. To the author's knowledge, no such formula is presently available in a closed form.

2.4.3 Asperity Statistics for Deterministic Surfaces

Some special types of finish may produce surfaces of non-Gaussian random distribution or deterministic distribution. For such arbitrary surfaces the distribution of asperity peaks cannot be obtained from profile data and need to be calculated directly from a surface map. In this section we present a simple sampling procedure to calculate asperity statistics from surface data.

We assume that:

- The surface is homogenous.
- The function $z(x, y)$ (surface height) for the surface is given. This can be obtained from two–dimensional sampling, holography or other methods.
- Asperity peaks are characterized by the peak height z_p and mean curvature κ.

The probability density of asperity height and curvature $f_{z_p\kappa}(z_p, \kappa)$ can be obtained from the following sampling procedure: Cover the domain Ω with a regular mesh of points $(x_i, y_i), i = 1, n$ presented in Fig. 2.8.

The mesh spacing h can be defined so as to filter out high–frequency noise. The sampling is performed by looping through the points $(x_i, y_i), i = 1, n$ and for each point:

1. Check if the point is a peak or near a peak within resolution h. The peak is identified as a peak if its height $z(x_p, y_p)$ is greater than all its nearest neighbors (eight for interior points). Alternatively, more elaborate criteria may be used.

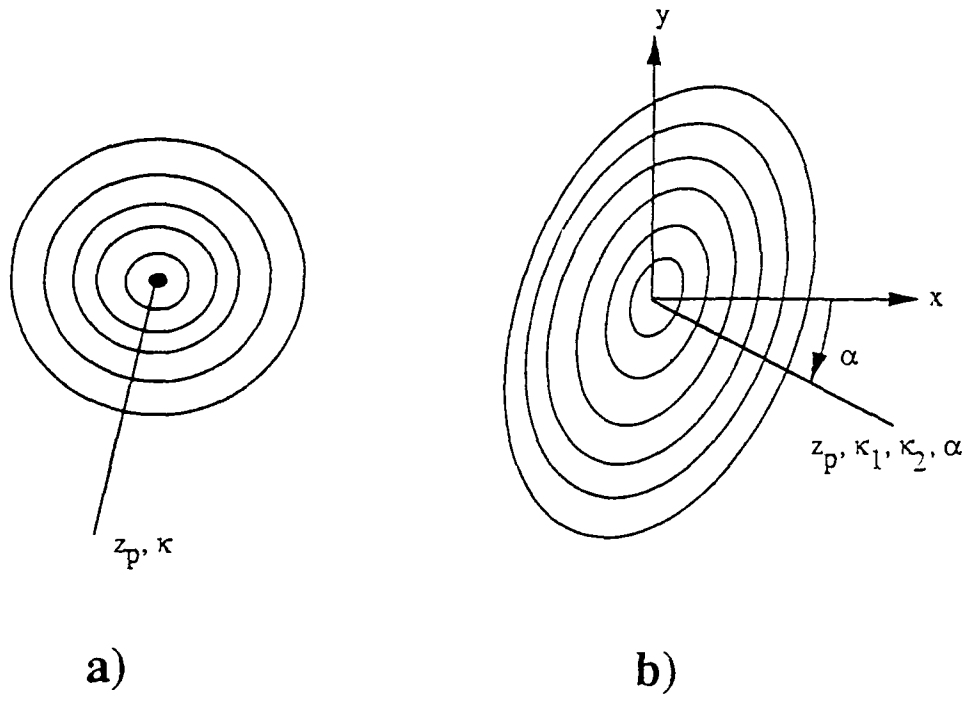

Figure 2.7: Typical asperity: (a) isotropic random surface, (b) anisotropic random surface.

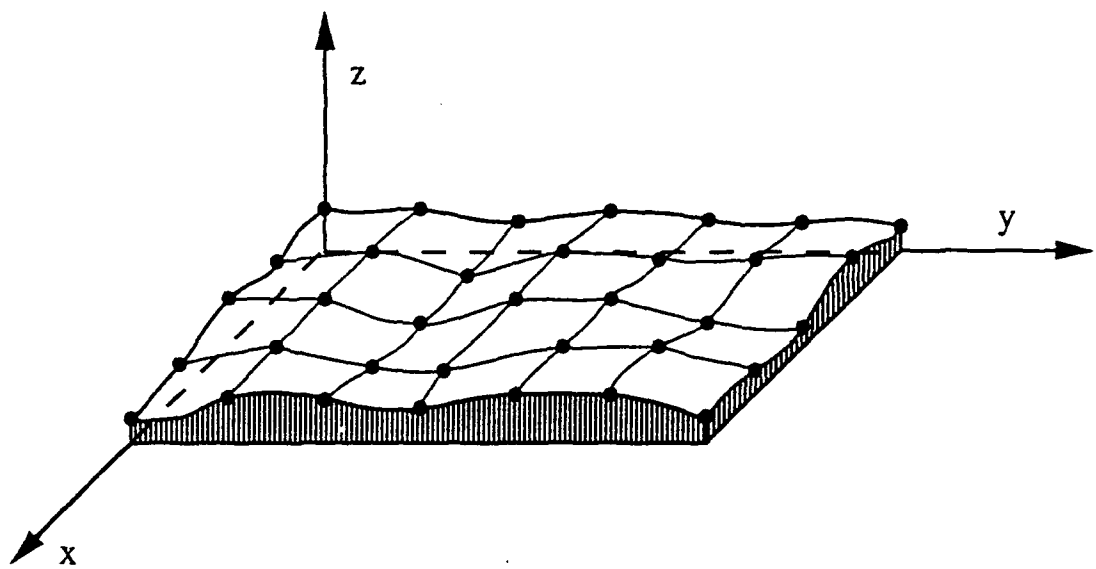

Figure 2.8: Sampling of arbitrary surface.

2. If the point is a peak, then calculate the second derivatives z_{xx}, z_{yy} and z_{xy}. Here simple finite difference formulas may be used or a generalized minimization procedure as presented in Appendix A.

The mean surface height and standard deviation of the surface height are calculated as:

$$\begin{aligned} \overline{z} &= \frac{1}{n}\sum_{i=1} z_i \\ \sigma^2 &= \frac{1}{n-1}\sum_{i=1}^{n}(z_i - \overline{z})^2 \end{aligned}$$

The joint probability density of asperity peak heights and curvatures can be calculated after locating all the peaks by dividing the range of peak heights and curvatures $[z_{p\,\min}, z_{p\,\max}] \times [\kappa_{\min}, \kappa_{\max}]$ into area elements $\Delta z_p \Delta\kappa$ (see Fig. 2.9).

Then for each area element with a center point (z_{pi}, κ_j) define

$$f_{z\kappa}(z_{pi}, \kappa_j) = \frac{1}{N_p} n_p(i,j)$$

Here N_p is the total number of peaks and $n_p(i,j)$ is the number of peaks within the area element $\Delta z_p \Delta\kappa$, identified by:

$$\begin{aligned} z_{p\,\min} + (i-1)\Delta z \le z_p &< z_{p\,\min} + i\Delta z \\ \kappa_{\min} + (j-1)\Delta\kappa \le \kappa_p &< \kappa_{\min} + j\Delta\kappa \end{aligned}$$

The values above define the discrete values of the joint probability density function of asperity peak heights and curvatures. This function may then be regularized by an application of appropriate approximation techniques. A similar procedure can be used if one chooses to characterize asperity peaks with more than two parmeters, such as z_p, κ_1, κ_2 and α for anisotropic surfaces.

2.5 Calculation of Macrocontact Expectations of Interface Parameters

Once we know the probability distribution of asperity heights and shapes as well as the values of any parameter X for single asperity, it is possible to calculate the expected value of X for the interface. This procedure varies somewhat depending on the classification of surface type. In this section we present a detailed procedure of the expectation calculation for Gaussian isotropic surfaces and outline its extensions to other surface types.

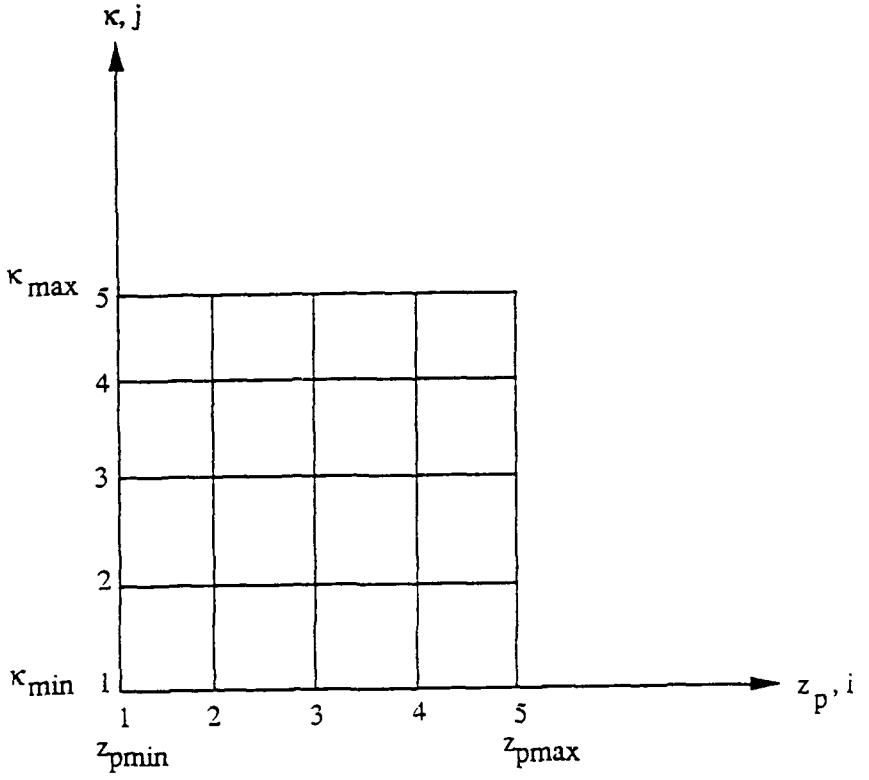

Figure 2.9: Accumulation of joint probability density $f_{z\kappa}(z_p, \kappa)$ for arbitrary surfaces.

2.5.1 Expectation Calculation for Gaussian Isotropic Surfaces

For Gaussian isotropic surfaces, the following parameters are needed to calculate the expected value of the macroscopic interface parameter X:

i) N_p — The number of peaks within the contact area A_0.

ii) $f_{\xi\eta}(\xi,\eta)$ — Probability density of asperity peaks of (nondimensional) height ξ and mean curvature η. By a simple change of variables one can define $f_{\xi\eta}(z_p,\kappa)$.

iii) $X(z_p,\kappa,a,d)$ — The value of parameter X for different peak heights z_p and curvatures κ, subjected to a normal approach a and sliding distance d.

iv) $\sigma,\dot{\sigma},\ddot{\sigma}$ — Deviations of profile heights, slopes, and curvatures used to nondimensionalize peak heights and curvatures.

The expected value of X per asperity is calculated as

$$E\Big(X(a,d)\Big) = \int_{-\infty}^{\infty}\int_{0}^{\infty} X(z_p,\kappa,a,d) f_{\xi\eta}(z_p,\kappa)\, d\kappa\, dz_p \tag{2.5}$$

and the macrocontact expectation of X is

$$\widehat{X}(a,d) = N_p\, E\Big(X(a,d)\Big)$$

Note that even for Gaussian isotropic surfaces there exist asperities of non-axisymmetric cross sections. However, due to isotropy, it suffices to consider only axisymmetric representatives of certain mean peak curvature κ. In this project we choose the asperity to be a cosine hill defined in a local coordinate system as:

$$z(x,y) = C\cos kx \cos ky$$

For this asperity the peak height and mean curvature are defined as

$$\begin{aligned} z_p &= C \\ \kappa &= Ck^2 \end{aligned}$$

The above shape is consistent with a generic representation of a Gaussian surface presented in formula (2.3). This is different than approaches presented to date in the literature, in which asperity peaks were usually assumed to be spherical or paraboloidal. This was because these works were based on analytical solutions for asperity deformation, such as Hertz' solution. In this work we are modeling the asperity by the finite element method, so it is possible to use the model which does not suffer from inconsistencies of spherical or paraboloidal asperity peaks.

Although for Gaussian isotropic surfaces the probability density of asperity heights and curvatures is analytic, the values of $X(z_p,\kappa,\ldots)$ that we obtain from finite element computations are not. Therefore the expected value of X must be calculated using numerical quadrature. This quadrature was implemented under the following assumptions:

(a) The domain of integration is truncated to the subregion $[z_{\min}, z_{\max}] \times [\kappa_{\min}, \kappa_{\max}]$, where the probability density $f_{\xi\eta}$ is large enough to effectively contribute to the final integral $E(X)$. This region is defined adaptively (see Section 2.6.2).

(b) The parameter values $X(z_p, \kappa, \ldots)$ are given (calculated by FEM) for certain selected values of peak heights and curvatures in the domain of integration. These points are not necessarily regularly distributed within the domain of integration.

The numerical procedure for the calculation of the integral consists of the following steps:

1. Divide area $[z_{\min}, z_{\max}] \times [\kappa_{\min}, \kappa_{\max}]$ into area elements $\Delta z \times \Delta\kappa$ (see Fig. 2.10).

2. Calculate the integral by looping over cells and applying numerical quadrature (trapezoidal, Simpson, Gauss, or any other) according to the formula

$$E(X) = \sum_{i=1}^{N} \left[\sum_{\alpha=1}^{m} \left\{ X\left(z_{p(\alpha)}, \kappa_{(\alpha)}, \ldots\right) f_{\xi\eta}\left(z_{p(\alpha)}, \kappa_{(\alpha)}\right) w_\alpha \Delta z \Delta\kappa \right\} \right] \tag{2.6}$$

where i is the number of integration cells, α is the number of quadrature points within a cell, and w_α is the corresponding weight factor.

Note that this integration requires the value of X at integration points $(z_{p(\alpha)}, \kappa_{(\alpha)})$ within each cell. Since it may be difficult to perform finite element analysis for values of z_p and κ corresponding exactly to all the integration points, these values are calculated from the original data points using the error minimization procedure presented in our previous report [94]. The quadrature rule currently implemented for integration are the trapezoidal and four-point Gauss rule.

Note that the above procedure introduces error due to truncation of the integration domain and due to numerical integration. This leads to a rather unwelcome result that even for constant X, the calculated expected value $E(X)$ would be different than X. In order to compensate for this error, we additionally calculate the integral of the probability density (which should be one):

$$I = \sum_{i=1}^{N} \left[\sum_{\alpha=1}^{m} f_{\xi\eta}\left(z_{(\alpha)}, \kappa_{p(\alpha)}\right) w_\alpha \Delta z \Delta\kappa \right]$$

Then the corrected value of expectation of X is calculated as:

$$\hat{E}(X) = E(X)/I \tag{2.7}$$

This procedure assures that for constant X the expected value $\hat{E}(X)$ is equal to X.

2.5.2 Expectation Calculation for Random Anisotropic Surfaces

As mentioned previously, for anisotropic Gaussian surfaces one has to consider asperities of random peak heights z_p, principal curvatures κ_1 and κ_2, and orientations of the principal

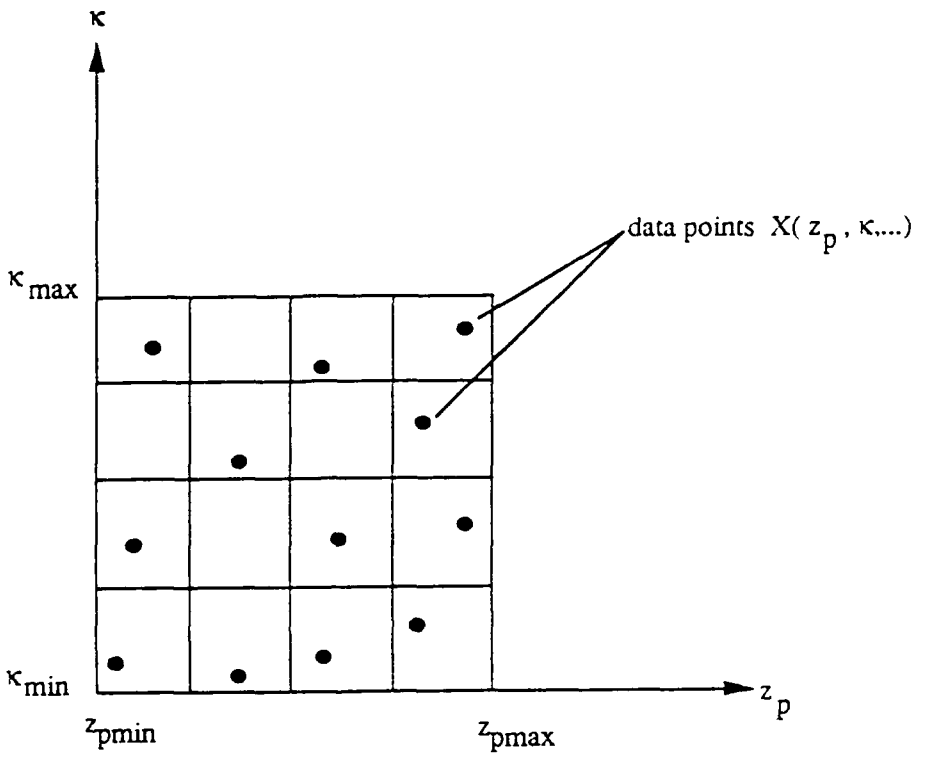

Figure 2.10: Numerical integration of expectation value $E(X)$.

axis α. The calculation of expected values of the interface parameters is similar to equation (2.5):

$$E\left(X\left(z_p, \kappa_1, \kappa_2, \alpha, a \ldots\right)\right) = \int_{-\infty}^{\infty}\int_{0}^{\infty}\int_{0}^{\infty}\int_{0}^{2\pi} X\left(z_p, \kappa_1, \kappa_2, \alpha \ldots\right) f_{\xi\eta_1\eta_2\alpha}\left(z_p, \kappa_1, \kappa_2, \alpha\right) d\alpha d\kappa_1 d\kappa_2 dz_p \tag{2.8}$$

Note that presently there exist no closed form solution for the probability density $f_{\xi\eta_1\eta_2\alpha}$ of asperity peaks of random heights, principal curvatures and orientations. Also note that in order to span the integration space, one would need to obtain finite element solutions for a large family of asperities, corresponding to various combinations of z_p, κ_1, κ_2, and α. This would be a very expensive task computationally, and will not be considered in this project.

2.5.3 Expectation Calculation for Deterministic Surfaces

The calculation of expectation values $E(X)$ for non–random surfaces follows essentially the same numerical procedure as for Gaussian isotropic or anisotropic surfaces. Depending on the surface type, the peak height z_p, curvature κ and other parameters may be selected to represent typical asperities. The joint probability density $f_{\xi\eta\ldots}(z_p, \kappa, \ldots)$ can be obtained from surface sampling as discussed in Section 2.4.3.

2.6 Numerical Verification of Statistical Postprocessing

The homogenization procedures discussed in the previous section for Gaussian isotropic surfaces were used as the basis for the implementation of specialized software for this purpose. Verification tests of this software were presented in our last yearly report [94]. In this report, we used the above approach to simulate Greenwood-Williamson contact model (Section 7).

3 Deformation Mechanics of a Single Asperity

We now focus on the analysis of a typical asperity in contact with a rigid flat. The asperity is a body of revolution, symmetric about its $z = x_3$-axis, and subjected to adhesion pressures q on its exterior surfaces that are not in contact with the rigid flat, and to contact pressures due to its indentation into the rigid flat (see Fig. 3.12). The equations governing the deformation of the asperity are discussed below.

3.1 Momentum and Geometric Equations

The momentum equations for the asperity are:

$$\sigma_{ij,j} = 0 \tag{3.9}$$

where σ_{ij} is the Cauchy stress tensor at a point $\boldsymbol{x} = (x_1, x_2, x_3) \in \Omega$, Ω being the open material domain of the asperity and $\sigma_{ij,j}$ is the divergence of the stress σ_{ij}.

In rate–dependent viscoplastic applications a rate form of the equilibrium equations is used:

$$\dot{\sigma}_{ij,j} = 0 \tag{3.10}$$

where the dot denotes the time derivative.

Geometric equations express strains in terms of displacements:

$$\varepsilon_{ij} = \frac{1}{2}(u_{i,j} + u_{j,i})$$

Strains can be decomposed into elastic and nonelastic strains:

$$\varepsilon_{ij} = \varepsilon_{ij}^{(e)} + \varepsilon_{ij}^{(n)}$$

Similarly as for the momentum equations, the rate form of geometric equations will also be used:

$$\dot{\varepsilon}_{ij} = \frac{1}{2}(\dot{u}_{i,j} + \dot{u}_{j,i})$$

3.2 Constitutive Equations

Surface asperities for typical engineering surfaces consist of the same material as the bulk body with possible contaminations and structure change from oxidation and surface finish processes. Therefore, for general surfaces a variety of material classes should be considered, such as elastic, hypoelastic, elastoplastic, etc. In this project two major material classes are considered, namely:

- linearly elastic (isotropic or anisotropic) for some metal surfaces, ceramics, composites, and hard rubbers, and
- viscoelastoplastic models for metallic surfaces and modern ductile ceramics.

3.2.1 Linearly Elastic Constitutive Models

The general linearly elastic constitutive relations are given as:

$$\sigma_{ij} = E_{ijkl}\varepsilon_{kl}$$

where E_{ijkl} are the components of the fourth order elasticity tensor. It has up to 36 independent coefficients for general anisotropic materials. However, for most material classes, the number of material coefficients is much smaller and, for isotropic materials, there are

only two coefficients, E and ν. The specific forms of tensor $\boldsymbol{E}$ for various materials are well known and will not be presented here.

3.2.2 Elasto–Viscoplastic Constitutive Model With Damage

We now describe the Bodner-Partom constitutive equations [10,11] used in the modeling of viscoelastoplastic asperities. The elastic–viscoplastic analysis is based on decomposition of strain rates

$$\dot{\varepsilon}_{ij} = \dot{\varepsilon}_{ij}^{(e)} + \dot{\varepsilon}_{ij}^{(n)} \tag{3.11}$$

where superscripts (e) and (n) denote elastic and nonelastic strain components, respectively. The constitutive relations are

$$\dot{\sigma}_{ij} = E_{ijkl}(\dot{\varepsilon}_{kl} - \dot{\varepsilon}_{kl}^{(n)}) \tag{3.12}$$

A nonelastic deformation is governed by the flow rule:

$$\begin{aligned} \dot{\varepsilon}_{ij}^{(n)} &= f_{ij}(\sigma_{ij}, z_k, \omega_k) \\ \dot{z}_i &= g_i(\sigma_{ij}, z_k) \\ \dot{\omega}_i &= h_i(\sigma_{ij}, \omega_i) \end{aligned}$$

where f_{ij}, g_i and h_i are constitutive functions, z_i are internal state variables, and ω_i are damage variables. These functions and state variables characterize the viscoplastic response of the material with continuum damage effects.

In the particular version of the Bodner-Partom theory applied in this work, the nonelastic flow rule is of the form:

$$\dot{\varepsilon}_{ij}^{(n)} = \lambda s_{ij}$$

where s_{ij} are the deviatoric components of a stress tensor

$$s_{ij} = \sigma_{ij} - \frac{1}{3}\sigma_{ij}\delta_{ij}$$

The current value of parameter λ is given by

$$\lambda^2 = \frac{1}{J_2} D_0^2 \exp\left[-\left(\frac{z^2(1-\omega^2)}{3J_2}\right)^n\right] \quad , \lambda > 0$$

where J_2 is the second invariant of a deviatoric stress tensor

$$J_2 = \frac{1}{2} s_{ij} s_{ij}$$

D_0 is a limiting strain rate in shear, n is a material constant and z and ω are state variables which evolve during deformation. In particular, z is the hardness variable, which represents viscoplastic hardening (or softening) of a material. The variable ω is the damage variable. This variable represents weakening of the material due to nucleation and propagation of microscopic voids and cracks in the material. The micro-cracks considered here are in the range of 0.01 mm in length. The rupture criterion is $\omega = 1$, which corresponds to the saturation of the material with voids. Alternatively, a single crack may grow to a size on the order of 1 mm. In the latter case, crack is too big to be treated in a continuum sense, and its propagation should be followed using the methods of fracture mechanics.

In the framework of materials science the value of ω is usually interpreted as ratio of the area of voids to the total area of a certain cross section of a sample:

$$\omega = \frac{A_{\text{void}}}{A}$$

The state variables z and ω evolve according to the specific equations of the viscoplastic theory:

1. Evolution equations of hardness variable

The internal state variable z consists of isotropic and directional components,

$$z = z^I + z^D$$

The evolution equation proposed for the isotropic hardening component [10,11,24,25] is

$$\dot{z}^I(t) = m_1[z_1 - z^I(t)]\dot{W}_p(t) - A_1 z_1 \left[\frac{z^I(t) - z_2}{z_1}\right]^{r_1} \tag{3.13}$$

with the initial condition, $z^I(0) = z_0$. In the first term, z_1 is the limiting (saturation) value of z^I, m_1 is the hardening rate, and the plastic work rate is

$$\dot{W}_p = \sigma_{ij}\dot{\varepsilon}_{ij}^{(n)}$$

which is taken as the measure of hardening. z_2 is the minimum value of z^I at a given temperature, and A_1 and r_1 are temperature dependent material constants. The evolution form of the directional hardening component (Refs. [10,11,24,25]) is defined as

$$z^D(t) = \beta_{ij}(t) u_{ij}(t)$$

where u_{ij} are the direction cosines of the current stress state,

$$u_{ij}(t) = \sigma_{ij}(t)/[\sigma_{kl}\sigma_{kl}]^{\frac{1}{2}} \tag{3.14}$$

The evolution equation for $\beta_{ij}(t)$ has the same general form as that for isotropic hardening but has tensorial character,

$$\dot{\beta}_{ij} = m_2[z_3 u_{ij}(t) - \beta_{ij}(t)]\dot{W}_p(t)$$
$$- A_2 z_1 \left\{ \frac{[\beta_{kl}(t)\beta_{kl}(t)]^{\frac{1}{2}}}{Z_1} \right\}^{r_2} v_{ij}(t)$$

where

$$v_{ij}(t) = \beta_{ij}(t)/[\beta_{kl}(t)\beta_{kl}(t)]^{\frac{1}{2}}$$

and

$$\beta_{ij}(0) = 0$$

As in Eq. (3.13), m_2 is the hardening rate. A_2 and r_2 are temperature dependent material constants.

2. Evolution of damage

The damage parameter consists, in general, of isotropic and directional components,

$$\omega = \omega^I + \omega^D$$

The evolution of isotropic damage proposed in reference [11] is of the form

$$\dot{\omega}^I = \frac{P}{H} \left\{ \left[ln \left(\frac{1}{\omega^I} \right) \right]^{\frac{p+1}{p}} \right\} \omega^I Q \tag{3.15}$$

In the above P and H are material constants, Q is the stress intensity function. given by

$$Q = \left[A\sigma^+_{\max} + B\sqrt{3J_2} + CI_1^+ \right]^{\nu}$$

where $\sigma^+_{\max}$ is the maximum principal tensile stress, I_1^+ is the first stress invariant (nonnegative) and J_2 is the previously introduced second invariant of deviatoric stress.

A, B, C, and ν are material constants. A, B, C must satisfy the condition

$$A + B + C = 1$$

Clearly, the actual proportion of these constants selects the factor for stress state which is most important in the development of internal damage.

The initial condition for isotropic damage is $\omega^I(0) = 0$. In practical analyses the coefficient ν is of the order 10 (compare ref. [11]). Thus, when SI (metric) units are used in the analysis, the factor Q as well as the constant H reach extremely high values, beyond the limit of real number capacity on some computers. Thus, for numerical analysis, equation (3.15) was recast in the equivalent, but more convenient form:

$$\dot{\omega}^I = \hat{p} \left\{ \left[ln \left(\frac{1}{\omega^I} \right) \right]^{\frac{p+1}{p}} \right\} \left(\frac{\hat{Q}}{\hat{H}} \right)^{\nu}$$

where:

$$\hat{Q} = Q^{\frac{1}{\nu}} = A\sigma^{+}_{\max} + B\sqrt{3J_2} + CI_1^{+}$$

$$\hat{H} = (H\tfrac{1}{\sec})^{\frac{1}{\nu}}$$

$$\hat{p} = p \cdot \tfrac{1}{\sec}$$

The additional advantage of this formulation is that both $\hat{Q}$ and $\widehat{H}$ are in the stress units (MPa) instead of the somewhat cumbersome $(MP_a)^{\nu}$. The directional damage is defined in a manner very similar to directional hardening, namely

$$\omega^D = \omega^D_{ij} u_{ij}$$

where u_{IJ} are directional cosines defined in equation (3.14) and the components of a tensor ω^D evolve according to equation

$$\omega^D_{ij} = \frac{q}{M}\left\{\left[ln\left(\frac{1}{\omega^D}\right)\right]^{\frac{q+1}{q}}\right\}\omega^D Q u_{ij}$$

where q and M are material constants. The initial condition is

$$\omega^D_{ij}(0) = 0$$

Note that there are several problems with practical application of directional damage, reliability of the above model and conducting experiments relevant for the evolution of necessary parameters. Even the extensive experiments presented in references [11,24,25] did not provide all the necessary data and, hence, the damage model is usually limited to the isotropic damage.

3.3 Boundary Conditions

The asperity can be viewed as a protuberance of a deformable half space (see Fig. 3.12). It is subject to boundary conditions resulting from its support, contact with the opposing surface, adhesion and sliding resistance.

3.3.1 Support Conditions

If the asperity is viewed as the protuberance on a deformable half space, the support conditions are defined as zero displacements at infinity:

$$\lim_{\substack{\|\boldsymbol{x}\|\to\infty \\ x_3\leq 0}} \boldsymbol{u} = \mathbf{0}$$

In practical computations we will usually consider only a certain section of the bulk material surrounding the asperity. Then the support condition will be:

$$\boldsymbol{u} = 0 \text{ on } \Gamma_u$$

on the cut–off boundary Γ_u.

3.3.2 Contact Condition

Let the position of the rigid flat (see figure 3.2) be defined by:

- a point $\boldsymbol{P}_o(x_o, y_o, z_o)$ which belongs to the flat, where x_o, y_o, z_o are its coordinates in the initial configuration,
- unit vector $\boldsymbol{N}$, normal to the flat,
- displacement w of the flat in direction $\boldsymbol{N}$.

Separation of material point in the deformable body from the flat is then given by the following formula

$$s = \boldsymbol{x} \cdot \boldsymbol{N} + \boldsymbol{u} \cdot \boldsymbol{N} - \boldsymbol{P}_o \cdot \boldsymbol{N} - w$$

where:

$\boldsymbol{x}$ - initial position of a material point,
$\boldsymbol{u}$ - displacement of this point.

The condition that the asperity can not penetrate the rigid flat is:

$$s \geq 0 \qquad \text{on } \Gamma$$

The actual contact region is $\Gamma_c = \{\boldsymbol{x} \in \Gamma,\ s(\boldsymbol{x}) = 0\}$. The difficulty associated with the contact condition in the above form is that it results in the weak formulation of the problem in the form of variational inequality, rather than the equation. In order to avoid difficulties involved in solving variational inequalities, the contact condition is usually regularized. In this work we will use the penalty-type regularization of the form:

$$t_N^c = t_N^c(a) \text{ on } \Gamma_c$$

where $a = -s$ is the approach (penetration) and t_N^c is the value of traction normal to the flat which defines resistance of the surface to penetration. Because we will be using rate formulation in viscoelastoplastic analysis, it is beneficial to introduce a continuously differentiable penalty function, for example in the form presented graphically in Fig. 3.11:

$$t_N^c = \begin{cases} 0 & \text{if} \quad a < 0 \\ \dfrac{H}{2\varepsilon}\, a^2 & \text{if} \quad 0 \le a < \varepsilon \\ H\left(a - \dfrac{\varepsilon}{2}\right) & \text{if} \quad a \ge \varepsilon \end{cases}$$

Here H is a large number (normal stress) and ε is a small number (penetration). The above penalty function guarantees continuous derivative of the normal traction with respect to a, which greatly improves practical performance of the numerical computations.

3.3.3 Adhesion

In the case of the surface asperity, an important contribution to the total normal force comes from adhesion due to intermolecular reactions (see Fig. 2.3).

According to the theory discussed in our previous report [94], the traction boundary condition due to adhesion is effective *outside* the contact zone:

$$\begin{aligned} t_N^a &= q(s) \quad \text{if } s > 0 \\ t_N^a &= 0 \quad \text{if } s = 0 \end{aligned}$$

where t_N^a is the value of normal traction $\sigma_{ij} N_j N_i$ resulting from adhesion. The actual value of the pressure q is a strongly nonlinear function of the separation s between surfaces and according to the Lennard-Jones theory discussed in reference [65] is defined by:

$$q(s) = \frac{8\Delta\gamma}{3\varepsilon}\left[\left(\frac{\varepsilon}{s}\right)^3 - \left(\frac{\varepsilon}{s}\right)^9\right] \tag{3.16}$$

where ε is an intermolecular distance (generally $\varepsilon = 0.3 - 0.5nm$) and $\Delta\gamma$ is the surface energy of adhesion.

3.3.4 Shear Resistance

In addition to normal stresses on the contact zone, formation of metallic bonds provides shear resistance of the junction. The corresponding surface traction can be expressed in the general form:

$$\boldsymbol{t_F} = t_S \boldsymbol{S} + t_T \boldsymbol{T}$$

where $\boldsymbol{S}$ is a vector parallel to the rigid flat and $\boldsymbol{T} = \boldsymbol{N} \times \boldsymbol{S}$. It is convenient to assume that the vector $\boldsymbol{S}$ defines a direction of prescribed sliding motion of the surface.

The components of the traction vector depend upon the normal load (or, equivanlently penetration) and relative sliding distance:

$$t_S = f(a, b_S)$$
$$t_T = f(a, b_T)$$

where

- a - penetration
- b_S, b_T - relative sliding on the plane in the $\boldsymbol{S}$ and $\boldsymbol{T}$ directions correspondingly
- $b_S = \delta - \boldsymbol{u} \cdot \boldsymbol{S}$
- $b_T = -\boldsymbol{u} \cdot \boldsymbol{T}$
- δ - prescribed sliding of the flat in the direction of vector $\boldsymbol{S}$ (see figure 3.12)

The specific form of functions f (.,.) depends on the actual model of shear resistance on the asperity tip. For example, shear resistance governed by regularized [53,59,92,93] Coulomb's friction law is defined as:

$$f(a, b) = \mu t_N^c \phi(b)$$

where μ is a coefficient of friction and ϕ is a regularization function, defined as:

- μ - friction coefficients
- ϵ - penalty parameter in normal contact (see section 3.3.2)

$$\phi(b) = \begin{cases} -1 & \text{for} \quad b \leq \epsilon_b \\ 2\dfrac{b}{\epsilon_b} + \dfrac{b^2}{\epsilon_b^2} & \text{for} \quad \epsilon_b < b \leq 0 \\ 2\dfrac{b}{\epsilon_b} - \dfrac{b^2}{\epsilon_b^2} & \text{for} \quad 0 < b < \epsilon_b \\ 1 & \text{for} \quad b \geq \epsilon_b \end{cases}$$

where ϵ_b is a small number (regularization parameter). The form of the regularization function ϕ is shown in figure 3.13.

Note that in practical modeling of surface asperities the shear resistance is often defined by the strength of metallic junctions between asperities. The detailed forms of corresponding resistance models will be studied in year 3 on this project.

3.3.5 Initial Conditions

Smooth functions $\boldsymbol{u}^0(\boldsymbol{x})$ and $\boldsymbol{z}^0(\boldsymbol{x})$ are prescribed such that for $\boldsymbol{x} \in \Omega$,

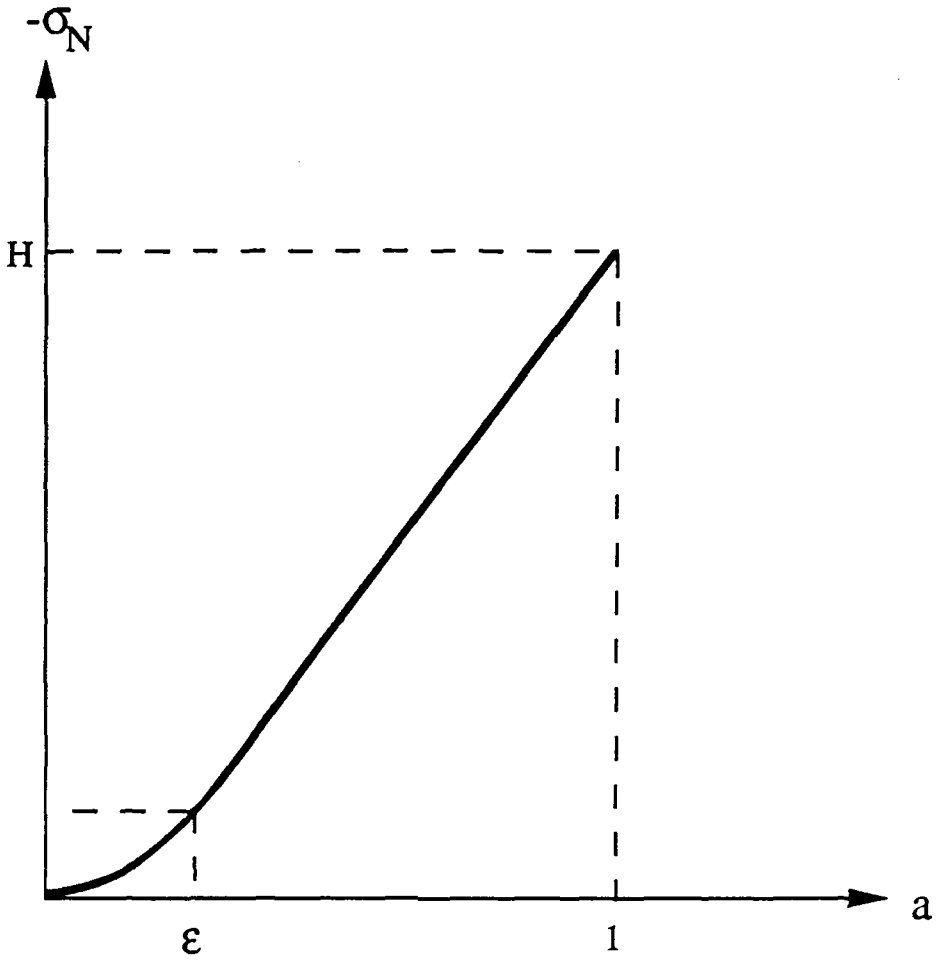

Figure 3.11: Penalty function for contact condition.

$$
\begin{aligned}
u_i(\boldsymbol{x}, 0) &= u_i^0(\boldsymbol{x}) \\
z_i(\boldsymbol{x}, 0) &= z_i^0(\boldsymbol{x}) \\
\omega_i(\boldsymbol{x}, 0) &= 0
\end{aligned}
$$

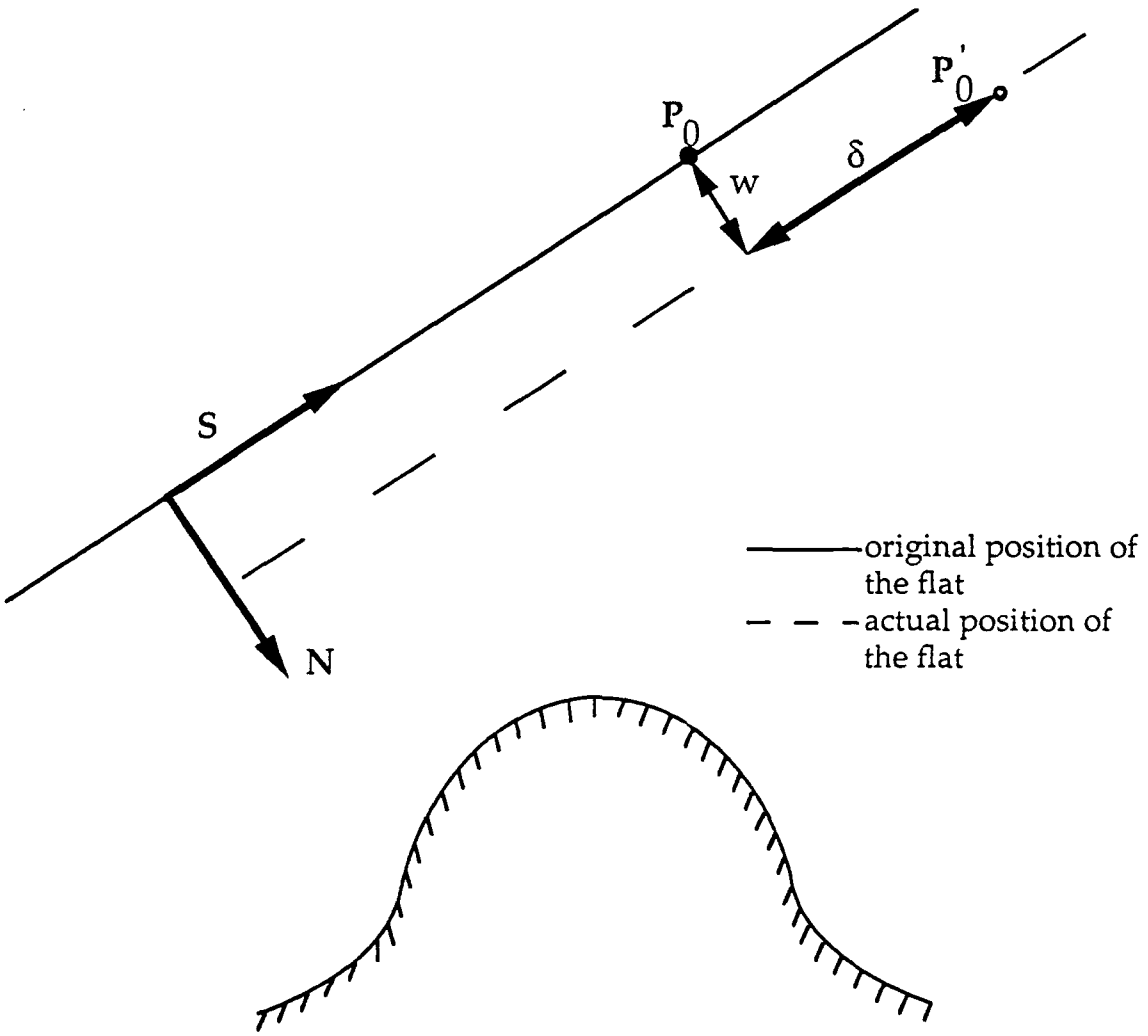

Figure 3.12: Surface asperity in contact with a rigid flat (a section).

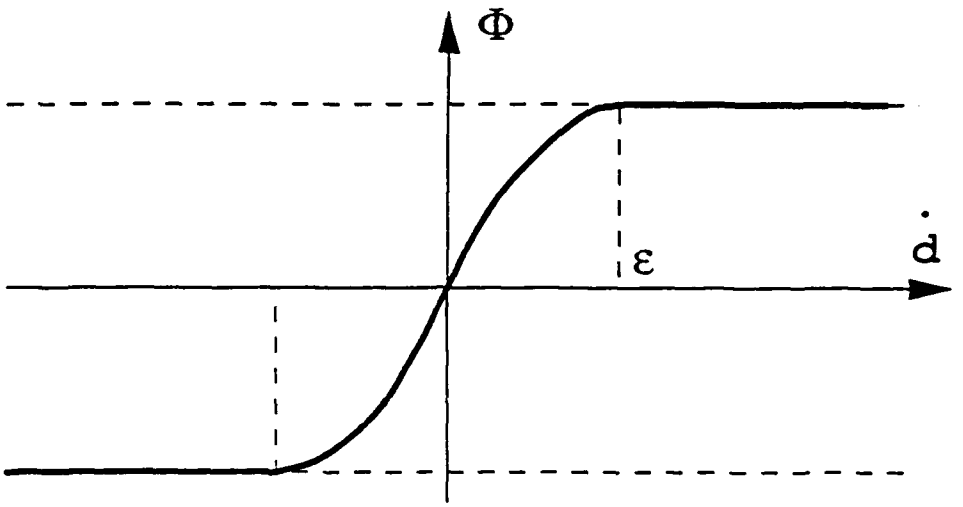

Figure 3.13: A regularization function ϕ

3.4 Variational Formulation

In order to obtain a weak formulation of a boundary–value problem we introduce the space of functions

$$V = \left\{ \boldsymbol{v} \in [W^{m,q}(\Omega)]^N \ , \ \boldsymbol{v}(\boldsymbol{x}) \to \mathbf{0} \text{ as } \|\boldsymbol{x}\| \to \infty \right\}$$

where Ω is a computational domain, N is the dimension of the physical space (2 or 3), and $W^{m,p}(\Omega)$ is the Sobolev space, where specific values of m, p and q depend on the particular form of constitutive equations.

Multiplying the equilibrium equation (3.10) by a test function and integrating over Ω we obtain the weak form of the rate equilibrium equations:

$$\int_\Omega \dot{\sigma}_{ij,j} v_i \, d\Omega = 0 \qquad \forall \, \boldsymbol{v} \in V$$

After the substitution of the constitutive equations, application of the divergence theorem and a grouping of terms the following variational problem is obtained:

Find a displacement rate field $t \rightarrow \dot{\boldsymbol{u}}(\boldsymbol{x}, t) \in V$ such that

$$\begin{aligned} \int_\Omega E_{ijkl}\dot{u}_{k,l}v_{i,j}d\Omega \;\; &+ \int_{\Gamma_c}(\dot{t}_N^c N_i + \dot{t}_S S_i + \dot{t}_T T_i)v_i ds = \\ &= \int_\Omega E_{ijkl}\dot{\epsilon}_{k,l}^{(n)}v_{i,j}d\Omega + \int_{\Gamma_t}\dot{\hat{t}}_i v_i ds \qquad\qquad \forall\, \boldsymbol{v} \in V \end{aligned} \tag{3.17}$$

Note that the values of the rates of normal and tangential stress on the contact zone need to be expressed in terms of displacements using formulas presented in previous sections (contact condition, and sliding resistance). After doing this, we obtain a more detailed formulation of the problem:

$$\begin{aligned} &\int_\Omega E_{ijkl}v_{i,j}\dot{u}_{k,l}d\Omega \;\; + \;\; \int_{\Gamma_c} v_i(B_{ij}^N + B_{ij}^S + B_{ij}^T)\dot{u}_j ds\; ds = \\ &\int_\Omega E_{ijkl}v_{i,j}\dot{\epsilon}_{k,l}^{(n)}d\Omega \;\; + \;\; \int_{\Gamma_C} v_i(G_i^N + G_i^S + G_i^T)\; ds + \\ &\int_{\Gamma_t} v_i\dot{\hat{t}}_i\; ds \qquad\qquad\qquad\qquad \forall\, \boldsymbol{v} \in V \end{aligned} \tag{3.18}$$

where

$B_{ij}^n = \frac{1}{\epsilon}N_i N_j$

$B_{ij}^S = \frac{\partial f}{\partial a}(a, b_S)N_i S_j + \frac{\partial f}{\partial b}(a, b_S)S_i S_j$

$B_{ij}^T = \frac{\partial f}{\partial a}(a, b_T)N_i T_j + \frac{\partial f}{\partial b}(a, b_T)S_i T_j$

$G_i^N = \frac{1}{\epsilon}\dot{w}N_i$

$G_i^S = [\frac{\partial f}{\partial a}(a, b_S)\cdot\dot{w} + \frac{\partial f}{\partial b}(a, b_S)\cdot\dot{\delta}]S_i$

$G_i^T = \frac{\partial f}{\partial a}(a, b_T)\dot{w}T_i$

$\hat{\boldsymbol{t}}$ = traction from static boundary conditions.

The rates of nonelastic strains $\dot{\epsilon}_{kl}^{(n)}$ can be obtained from the relevant constitutive theory (see Section 3.2.2). For elastic materials they are identically equal to zero.

For elastic materials it is also possible and computationally more efficient to use a total formulation of the problem which is as follows.

Find a displacement field $\boldsymbol{u}(x)\epsilon V$, such that

$$\int_\Omega E_{ijkl}v_{i,j}u_{k,l}d\Omega + \int_{\Gamma_c} v_i\frac{1}{\varepsilon}N_iN_ju_jds = \int_{\Gamma_c} v_i\frac{1}{\varepsilon}N_i(w - x_k\cdot N_k + P_{0k}\cdot N_k)ds + \int_{\Gamma_t} v_i\hat{t}_ids \quad \forall\, \boldsymbol{v}\in V \tag{3.19}$$

3.5 Solution Method for Elastic Contact Problems

Formulation of the contact problem is nonlinear even in the case of contact with an elastic body because the area of contact depends on displacements ($\Gamma_c = \Gamma_c(\boldsymbol{u})$). Generally, variational equation (3.19) for $\boldsymbol{u}$ can be written in the following form

$$\boldsymbol{L}(\boldsymbol{u}) - \boldsymbol{R} = 0, \tag{3.20}$$

where $\boldsymbol{L}$ stands for the left-hand side and $\boldsymbol{R}$ for the right-hand side.

This equation is obtained from (3.19) by requiring that it be satisfied for any $\boldsymbol{v}$ belonging to V. Because the condition is nonlinear it results in a nonlinear system of equations. In aim to solve the problem effectively, Newton-Raphson iteration technique was used. The idea of the method is to substitute a nonlinear functional by its linear part. Linearization is made at a series of points. Each point is the solution of the problem linearized at the previous point. If the series is convergent it is convergent to a solution of the nonlinear problem. For a simple case of a nonlinear equation with one unknown two steps of Newton-Raphson method are shown in Fig. 3.14.

Basic formulas of the Newton-Raphson method are presented below. Let us assume that we know a field $\boldsymbol{u}_n$ which is an approximate solution of the equation 3.20. $\boldsymbol{u}_o \equiv 0$ can be assumed. First two components of the Taylor series evolution of left hand side of equation 3.20 give

$$\boldsymbol{L}(\boldsymbol{u}^n) - \boldsymbol{R} - \mathbf{grad}_{\boldsymbol{u}}[\boldsymbol{L}(\boldsymbol{u}^n) - \boldsymbol{R}]\delta\boldsymbol{u} \approx 0$$

Assuming that $\delta\boldsymbol{u} = \boldsymbol{u}^{n+1} - \boldsymbol{u}^n$ we obtain

$$\boldsymbol{L}(\boldsymbol{u}^n) - \boldsymbol{R} + \mathbf{grad}_{\boldsymbol{u}}\boldsymbol{L}(\boldsymbol{u}^n)(\boldsymbol{u}^{n+1} - \boldsymbol{u}^n) = 0$$

Equation 3.20 is a linear equation for $\boldsymbol{u}^{n+1}$. We use this equation to compute a sequence of approximate solutions $\boldsymbol{u}^1, \ldots, \boldsymbol{u}^M$. The process is stopped when $||\boldsymbol{u}^M - \boldsymbol{u}^{M-1}||$ and $||\boldsymbol{L}(\boldsymbol{u}^M) - \boldsymbol{R}||$ are small enough.

For contact with elastic bodies, equation (3.20) has the following form

$$\int_\Omega E_{ijkl}v_{i,j}u^{n+1}_{k,l}d\Omega + \int_{\Gamma_c(\boldsymbol{u}^n)} v_i\frac{1}{\varepsilon}N_iN_ju^{n+1}_jds = \int_{\Gamma_c(\boldsymbol{u}^n)} v_i\frac{1}{\varepsilon}(P_{ok}\cdot N_k - x_k\cdot N_k + w)N_ids + \int_{\Gamma t} v_i\hat{t}_ids$$

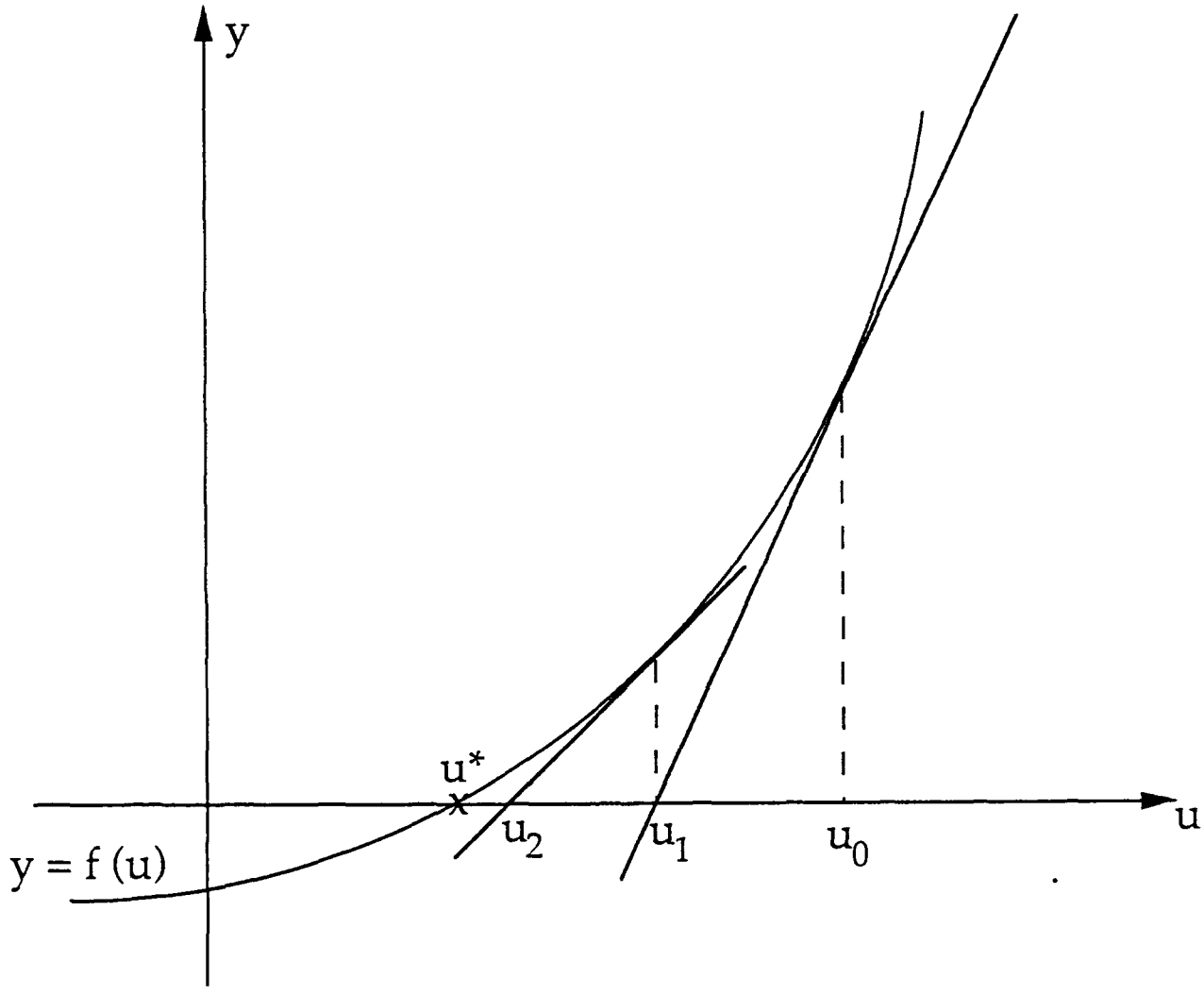

Figure 3.14: Graphical presentation of construction of a series $u_0, u_1, u_2, \ldots$ convergent to a solution u^* of equation f (u) = 0.

Variations were evoluated neglecting dependence $\Gamma_c = \Gamma_c(\boldsymbol{u})$. The above linearized problem is solved by the standard FEM.

In order to provide automatic control of the performance of nonlinear procedures, an expert system-like approach has been applied. This application is based on our previous research on automation of computational procedures [4], and employs several heuristic rules to monitor and control the performance of nonlinear iterations. While in the original implementation discussed in reference [4] the specialized knowledge engineering software was used to develop the expert system, in this project the essential features of the expert system were coded in FORTRAN and included in the code. The expert system is activated at each time step after completing a prescribed number of iterations (sufficient to estimate trends in error histories). The decisions of the expert system are used to control the solution process and obtain a converged solution at minimum cost.

3.6 Solution Method for Viscoplastic Contact Problems

Formulation of the problem in this case is time-dependent.

The strategy employed in the solution of this problem is as follows: with the initial distribution of stress, temperature and internal variables specified use the rate form of the equilibrium condition (Eq. (2.23)) to obtain the nodal displacement rates. Then integrate the constitutive equations forward in time at the element Gauss integration points. With updated value of the stress, temperature and internal variables at the new time, the equilibrium equation is solved again. This sequence of determining the nodal displacement rates, then advancing the constitutive equations in time is continued until the desired history of the initial boundary-value problem has been obtained.

Thus, the algorithm proceeds through the following steps:

1. At time t, initialize σ_{ij}, Z_i for each element;
2. Calculate $\dot{\epsilon}^n_{ij} = f_{ij}(\sigma_{ij}, Z_k)$ for each element;
3. Assemble and solve $[K]\dot{U} = \dot{F}$;
4. Calculate $\dot{\epsilon}_{ij}$ for each element, $\dot{\epsilon} = [B]\dot{U}$;
5. Calculate $\dot{\sigma}_{ij}$ for each element, $\dot{\sigma} = [E]\dot{\epsilon} - \dot{\epsilon}^n$;
6. Calculate $\dot{Z}_i$ for each element, $\dot{Z}_i = g_i(\sigma_{ij}, Z_k)$;
7. Integrate $\dot{\sigma}_{ij}, \dot{Z}$ forward for each element to get σ_{ij} and Z_i at $t + \Delta t_s$;
8. If $t + \Delta t_s < t_{\text{final}}$ go to 2, otherwise stop.

The computational method above has been presented for a constant time step Δt_S. Computational experience by several investigators (see refs. [7,8,54]) indicates that a very

small time step can be required because of the "stiff" nature of the ordinary differential equations describing the internal state variables. To gain improved efficiency and reliability a variable time step algorithm has been implemented. The basic idea of this variable time step algorithm is presented below for a scalar evolution equation.

The solution is advanced using a predictor-corrector scheme. The predictor phase consists of an Euler step:

$$\dot{y} = f(y, t) \tag{3.21}$$

The solution is advanced using a predictor-corrector scheme. The predictor phase consists of an Euler step:

$$y^P_{t+\Delta t} = y_t + \Delta t \dot{y}_t \tag{3.22}$$

$$\dot{y}^P_{t+\Delta t} = f\left(y^P_{t+\Delta t}, t + \Delta t\right) \tag{3.23}$$

An error indicator E [15,24] is then computed from

$$E = \frac{\left|\Delta t \left(\dot{y}^P_{t+\Delta t} - \dot{y}_t\right)\right|}{2\left|y^P_{t+\Delta t}\right|} \tag{3.24}$$

The error indicator is next compared with a preset error criterion and if the criterion is met, the time step is small enough to proceed to the corrector stage. Otherwise, the predictor phase for Eqs. (3.22)–(3.23) is repeated with a smaller time step. For the viscoplastic evolution equations with damage modeling, the control variables used to calculate the error indicator were the components of a stress tensor σ_{ij}, internal state variables Z_i, and the damage variables ω_i, with the maximum of these selected as the controlling error.

The corrector phase is the modified Newton scheme,

$$\dot{y}_{avg} = \left(\dot{y}_t + \dot{y}^P_{t+\Delta t}\right)/2$$

$$\dot{y}^C_{t+\Delta t} = y_t + \Delta t \dot{y}_{avg}$$

A flowchart depicting the adaptive scheme is shown in Fig. 5.18.

4 Finite Element Analysis of Contact Problems with Friction

4.1 General Information About the 3D Finite Element Code

The development of asperity modeling capabilities was based on existing, state-of-the-art three-dimensional adaptive finite element kernel code, which consists of several separate modules organized around the common data structure and execution supervisor. Figure 4.15 shows a general structure of the code directories. The most important modules are:

- an object-based data structure designed specifically for the *h-p* adaptive finite element method,
- an execution supervisor controlling the overall execution of the computations,
- pre– and postprocessors,
- an adaptive package,
- linear equation solvers, and
- a solver for a specific boundary value problem (in this case, asperity modeling).

Importantly, the elements of the finite element data structure, adaptive package, graphical interfaces and linear equations solvers were designed to be applicable to a general class of problems, and relatively easy customizable to specific problems in solid mechanics or fluid mechanics. Below, selected modules of the above kernel are discussed in more detail.

Object-based Data Structure

A new state-of-the-art data structure was designed and implemented in the kernel to avoid typical limitations of traditional finite element codes, such as:

- fixed size common blocks and arrays,
- predefined limits on problem size,
- element information spread throughout memory in variety of arrays.

The object-based data structure was coded in C computer language, which allows for dynamic memory allocation and more flexible handling of objects and structures. Typical examples of objects handled by this data structure are:

- elements,

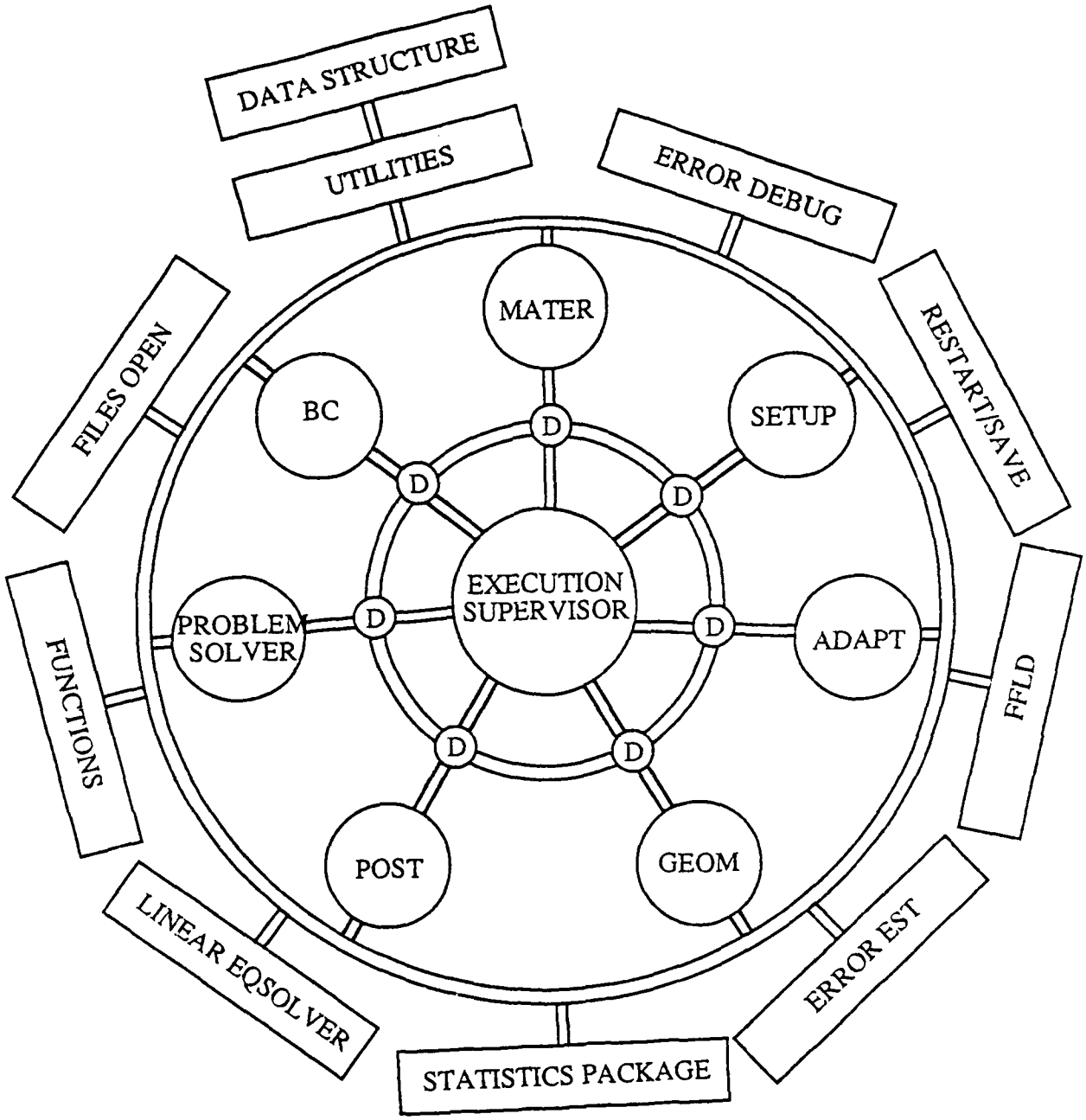

Figure 4.15: A general finite element code structure

- nodes,
- boundary condition data,
- set of degrees of freedom, etc.

The major advantages of object-based handling of these structures are listed below:

- the objects are created only when needed,
- all related information is contained in one structure, and closely packed in memory,
- all the objects are automatically saved/restarted,
- the memory is reused when object is deleted, say during mesh refinement.

It is of importance to note here, that the elements in the above data structure are grouped and colored in order to facilitate vector and parallel processing. The basic idea of this vectorization and parallelization is presented in figure 4.16. Importantly, all the elements in a batch are of the same type, so that the generation of element stiffness matrices and right-hand sides can be effectively vectorized by putting loop over elements as the innermost loop. On the other hand, since the elements in different colors have no common nodes or sides, the generation of element of element matrices and assembly for different colors can be performed in parallel.

Adaptive three-dimensional finite element meshes

The finite element kernel is designed to handle h-p adaptive finite element meshed for three- and two- dimensional problems. By h-p adaption we understand a finite element technique, wherein the elements can be automatically subdivided into smaller elements (h-refinement /unrefinement) and the polynomial order of approximation can be locally increases or reduced. A major advantage of properly designed h-p mesh is that it can achieve a higher order of accuracy with much less degrees of freedom than traditional finite element methods. Moreover, the optimal mesh is designed automatically by adaptive procedure driven by appropriate error estimators.

For three-dimensional problems, anisotropic h-refinement can offer a wide improvement in computational effort over more conventional isotropic refinement schemes. This is primarily true because anisotropic refinement allows for selected refinement in the directions of interest only (i.e., directions of high error). Thus, anisotropic refinement may greatly reduce the total number of unknowns in many problems, in turn reducing the required computational effort.

Isotropic refinement implies that an element is identically refined in each local direction. For a hexahedral element, an isotropic refinement is a division into two along each of the three local directions, which results in eight sub-elements. In contrast, an anisotropic refinement of a hexahedral element is a division into two along a single local direction, resulting, of course, in only two sub-elements. Thus, if solution phenomena is oriented with respect to

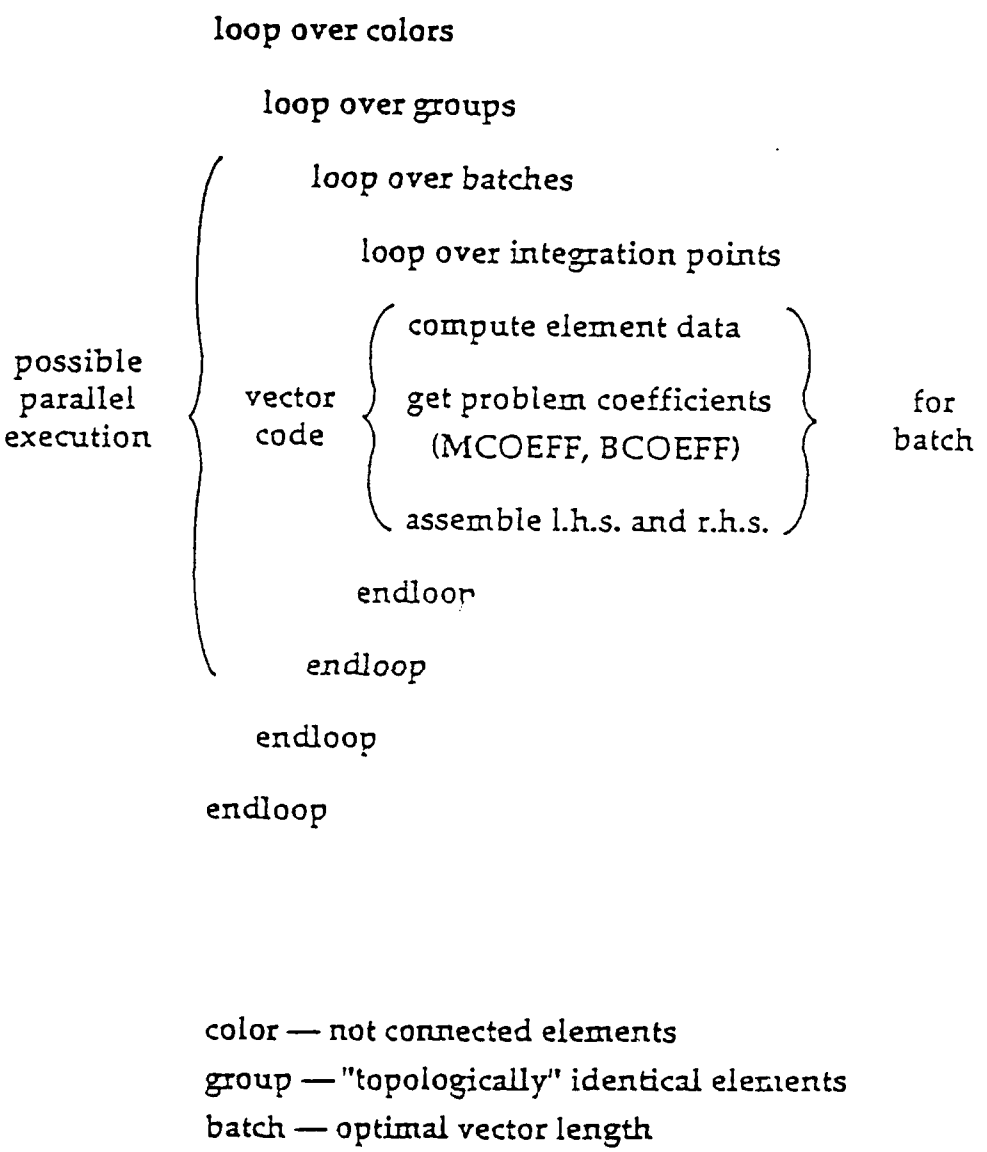

Figure 4.16: Vectorization and parallelizaton for groups and colors

a particular local direction, then anisotropic refinement allows for degrees of freedom to be introduced only in the direction which actually reduces the total error. Isotropic refinement, on the other hand, would have introduced degrees of freedom in all directions, many of them providing little improvement to the overall solution. Anisotropic refinement can, therefore, provide a higher level of accuracy than isotropic refinement using the same number of degrees of freedom.

Several examples of h-adapted meshes in three dimensions will be shown in Section 6. Note that the mesh refinement introduces several theoretical and numerical complications into the algorithm, such as:

- constrained or "hanging" nodes between elements of different refinement level,
- propagation of constraints and possible "deadlocks" in the case of directional refinements for complex geometries,
- complications of unrefinement due to one-to-two approximation rule.

Detailed discussion of these issues is beyond the scope of this report. It is sufficient to note, that before application of the above kernel to asperity modeling all these difficulties have been successfully resolved and the existing kernel offers operational unique automated directional refinement capability for three-dimensional hexagonal meshes.

Interactive user's interface and graphical postprocessing

have been implemented in the adaptive kernel to enable user-friendly operation of the code and viewing of three-dimensional result. The interactive graphic interface is based on a window environment, with a menu-driven selection of options. A sample view of the screen with several windows open is presented in figure 4.17.

The graphic interface can be customized for specific applications, such as contact and friction modeling, so that the solution process and essential data can be controlled interactively by the user.

The most important feature of the graphical user interface is a three-dimensional interactive postprocessing capability. For two-dimensional models, such visualization is rather trivial as all of the computational domain is always visible and it is a simple matter to zoom and/or pan through the mesh to closely review the results. The real challenge comes from the need to visualize phenomena in three-dimensional domains where most of the numerical data is actually hidden from the observer and one needs to enter the domain to view the local structure of the solution.

The postprocessing capability implemented in the kernel is capable of displaying solution obtained on structured and unstructured meshes, with both h-refinement and p-enrichment present in the mesh. The package is fully interactive and operates efficiently on high-end workstations. The basic graphic features displayed include:

- mesh plots,

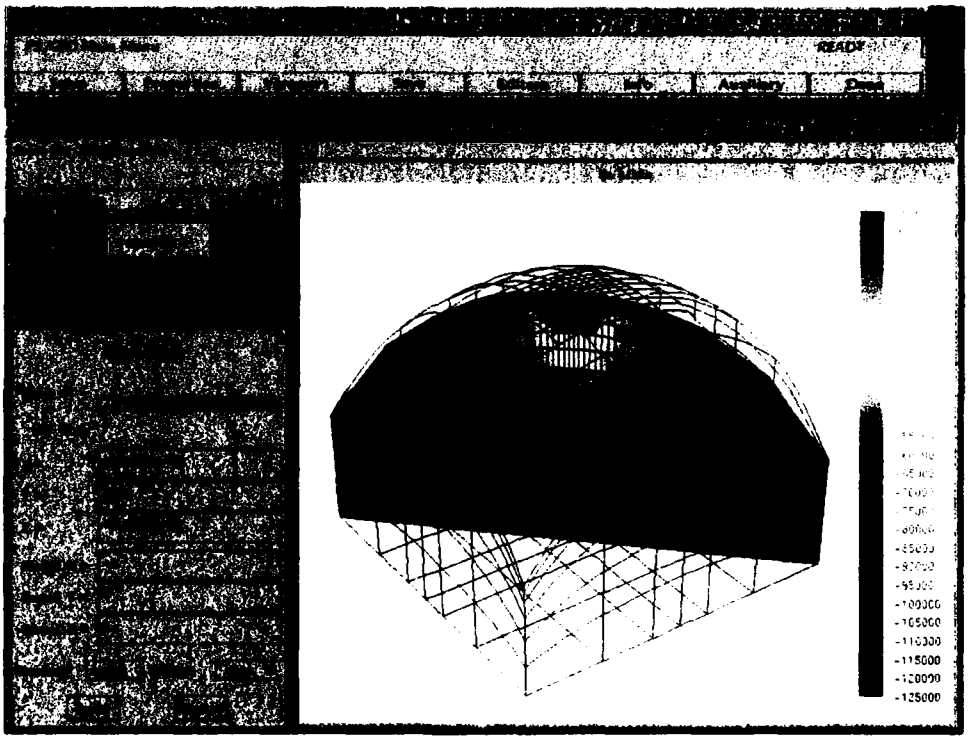

Figure 4.17: Sample screen with interactive window environment

- isosurfaces of selected quantities,
- slicing planes with overlaying isolines,
- deformed configurations,
- three-dimensional cursor for picking pointwise values of the solution,

All the above displays are available with interactive translation, rotation and zoom options, hidden line removal, panning, etc.

Importantly, the graphics package is designed to take advantage of specialized graphic hardware and software available on many platforms. The primary platform for the package is the SGI Iris family, which is also a primary platform in this project. Alternatively, X-windows graphics is supported, which is operational on most Unix workstations.

4.2 Formulation of a Structural Deformation Problem in the 3D Code

In the second year of the friction project, the 3D kernel was customized to solve contact problems. It was supplemented with over 5,000 instructions. They enable to run specialized drivers when a contact problem is to be solved. The drivers solve the contact problem using either total formulation or incremental formulations (see section 3.4). The first one uses Newton-Raphson iterative method and calls the FEM linear solver at each iteration step. The second driver uses Euler predictor corrector integration method with automatic time step control and calls the FEM linear solver twice at each time step.

To solve solid mechanics problems with contact, additional customization of the kernel FEM code had to be implemented. They define, in a special format, coefficients of the volume and boundary integrals introduced in previous section. As regards the contact condition, it was assumed that contact can take place at any point of the boundary on which static boundary conditions are applied. Therefore, while the integrals over this part of boundary are evaluated, the program examines whether an integral point is in contact with the flat. If penetration is greater than zero, then integrals corresponding to contact and friction are added to the coefficients of the stiffness matrix and the right-hand side.

If a problem with contact is to be solved then an additional data file is read. This additional data defines initial position and orientation of the rigid flat, prescribed displacements of the flat, material constants, regularization parameters and error tolerances. The results of each iteration or time step are printed on screen and to a disk file.

To enable automatic generation of meshes, five additional programs were prepared. They generate customized grid files for:

- 3D axisymmetric asperity (cosine hill),
- 3D axisymmetric asperity (spherical),

- 2D asperity (cosine hill),
- 2D asperity (cylindrical),
- 2D trapezoidal asperity.

The first two programs make use of an in-house GAMMA3D mesh generator . All of them provide generation of meshes with first and second order of geometry approximation.

5 Basic Verification of Numerical Models

To confirm reliability of the code and material models several numerical tests were done. Selected tests are described in this section.

The first test was carried out to verify the total formulation. It was uniaxial tension of an elastic body. It was performed for both 3D and 2D problems with both second and first order geometry approximation. The results of tests were compared with analytical solutions of the tension problem. The errors of computed displacements and stresses were less then 0.1 percent.

The objective of the next group of tests was to verify incremental formulation of the viscoplastic problem. They were carried out for alloy B1900+Hf at temperature 871°C. Material constants as well as experimental results for this material are given in reference [10]. For Bodner-Partom model they are as follows:

D_o	=	$10^4\ s^{-1}$	m_1	=	$0.270\ MPa^{-1}$
n	=	1.03	m_2	=	$1.52\ MPa^{-1}$
z_o	=	2400 MPa	r_1	=	$r_2 = 2$
z_2	=	2400 MPa	A_1	=	$A_2 = 0.0055\ s^{-1}$
z_1	=	3000 MPa	E	=	$142\ GPa$
z_3	=	1150 MPa	ν	=	0.0805

Some of these tests are listed below:

(a) Solution of the uniaxial tension for an elastic body by the incremental formulation. The results were the same as obtained by the total formulation.

(b) Solution of the uniaxial tension for an elasto-visco-plastic body. The results were compared with an experiment presented in reference [55]. Certain discrepancy of results was observed (see Fig. 5.19). This discrepancy was caused by an erroneous value of the Young modulus given in reference [55]. After a correction of Young modulus ($E = 132\ GPa$) the numerical and experimental results agreed satisfactorily (see Fig. 5.20). The test verified mathematical and numerical models for this simple loading (uniaxial tension).

(c) Next three tests were carried out in order to examine how the computer program works for more complicated loading histories. The results of those tests were not compared neither with experimental nor with analytical solutions but they look reasonable and they confirmed reliability of the computer code. The tests were the following:

- Uniaxial cyclic tension and compression Fig. 5.21.
- Uniaxial loading for 5,000 s and relaxation for next 5,000 s Fig. (5.22).
- Loading for 1,000 s and creep for next 1,000 s Fig. 5.23.

The above basic tests verified the formulation of the contact problem as well as its applications in the computer code. It was possible to perform further tests and comparisons of results.

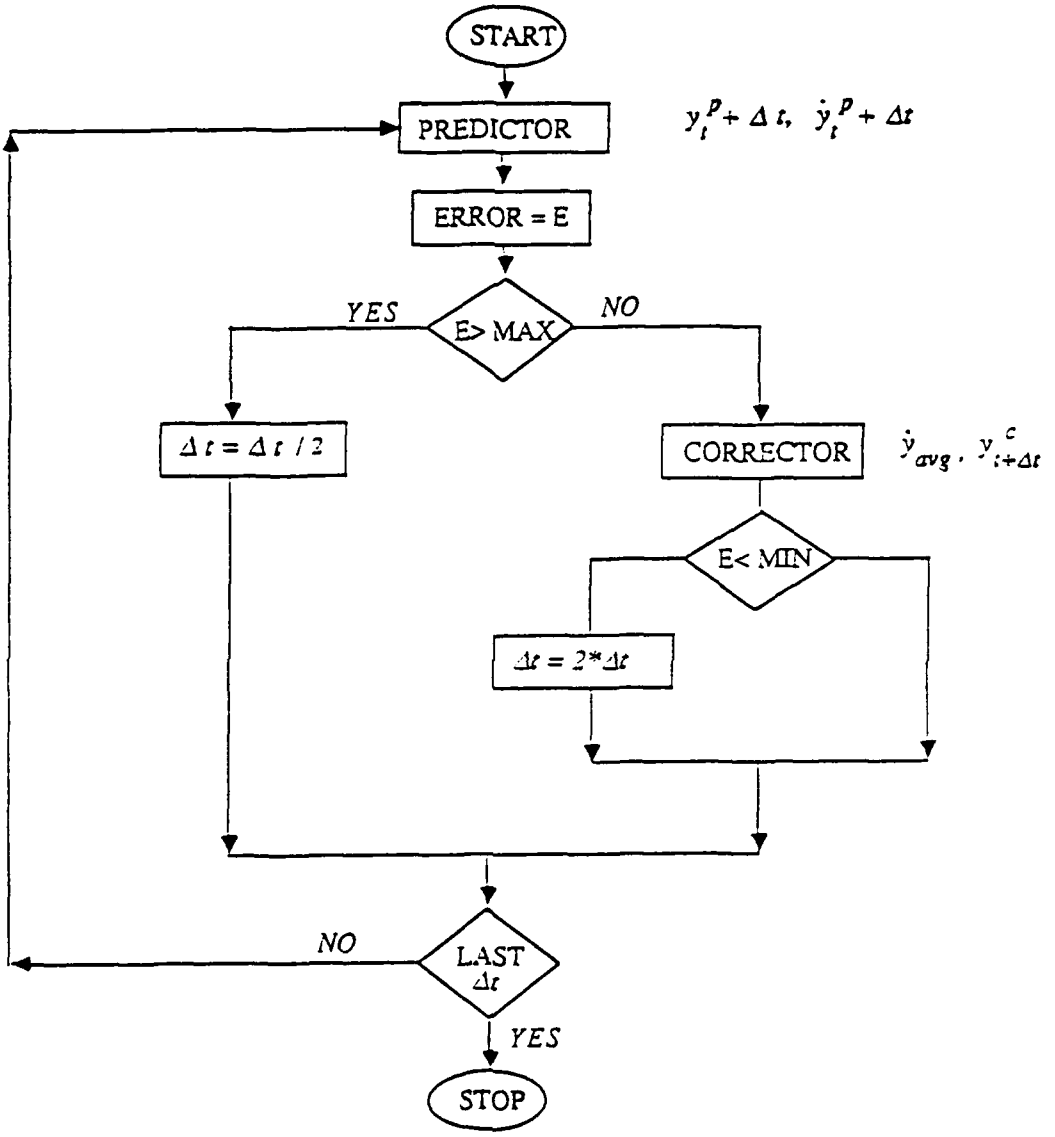

Figure 5.18: Adaptive timestepping algorithm for viscoelastoplastic evolution problems.

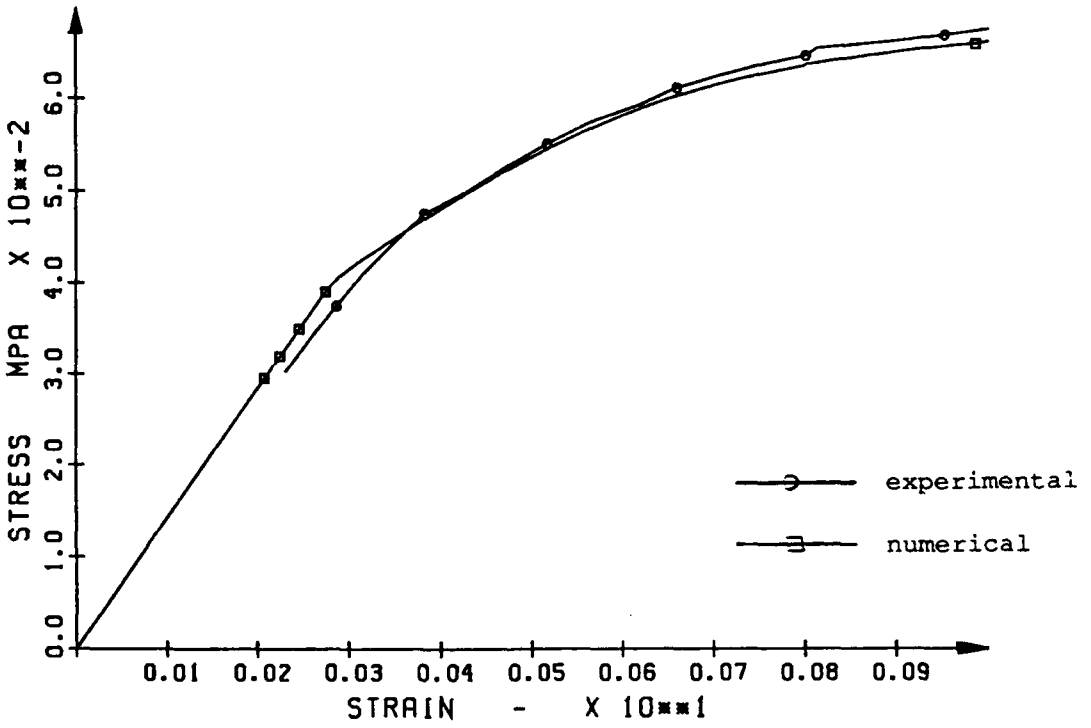

Figure 5.19: Experimental and numerical results of uniaxial tension (incorrect value of Young modulus).

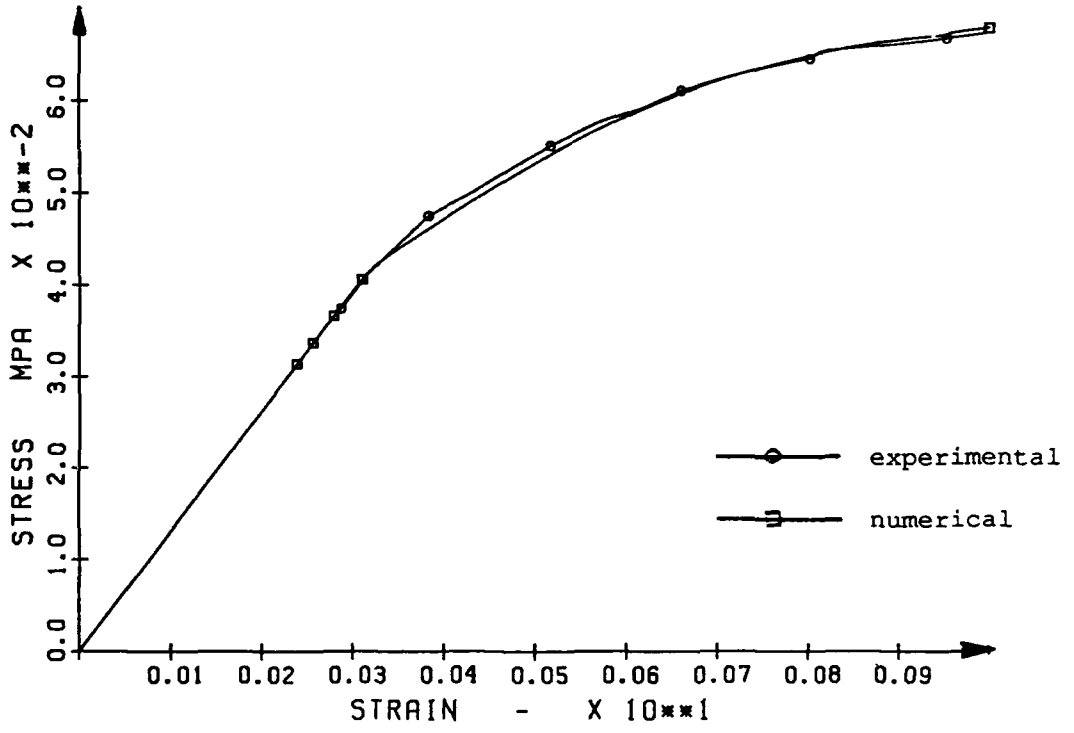

Figure 5.20: Experimental and numerical results of uniaxial tension of a specimen with corrected Young modulus

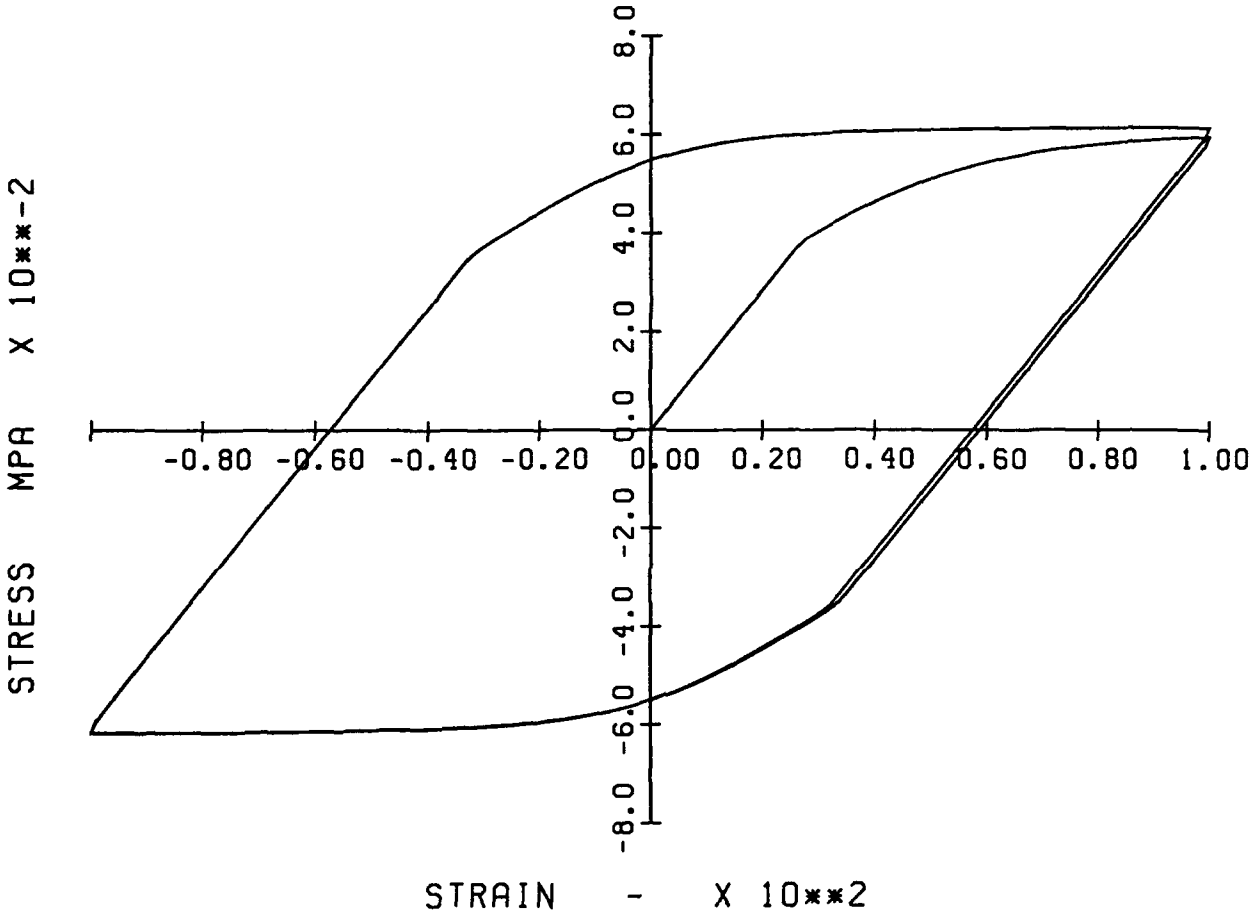

Figure 5.21: Cyclic loading test of the viscoplastic model – 10 cycles.

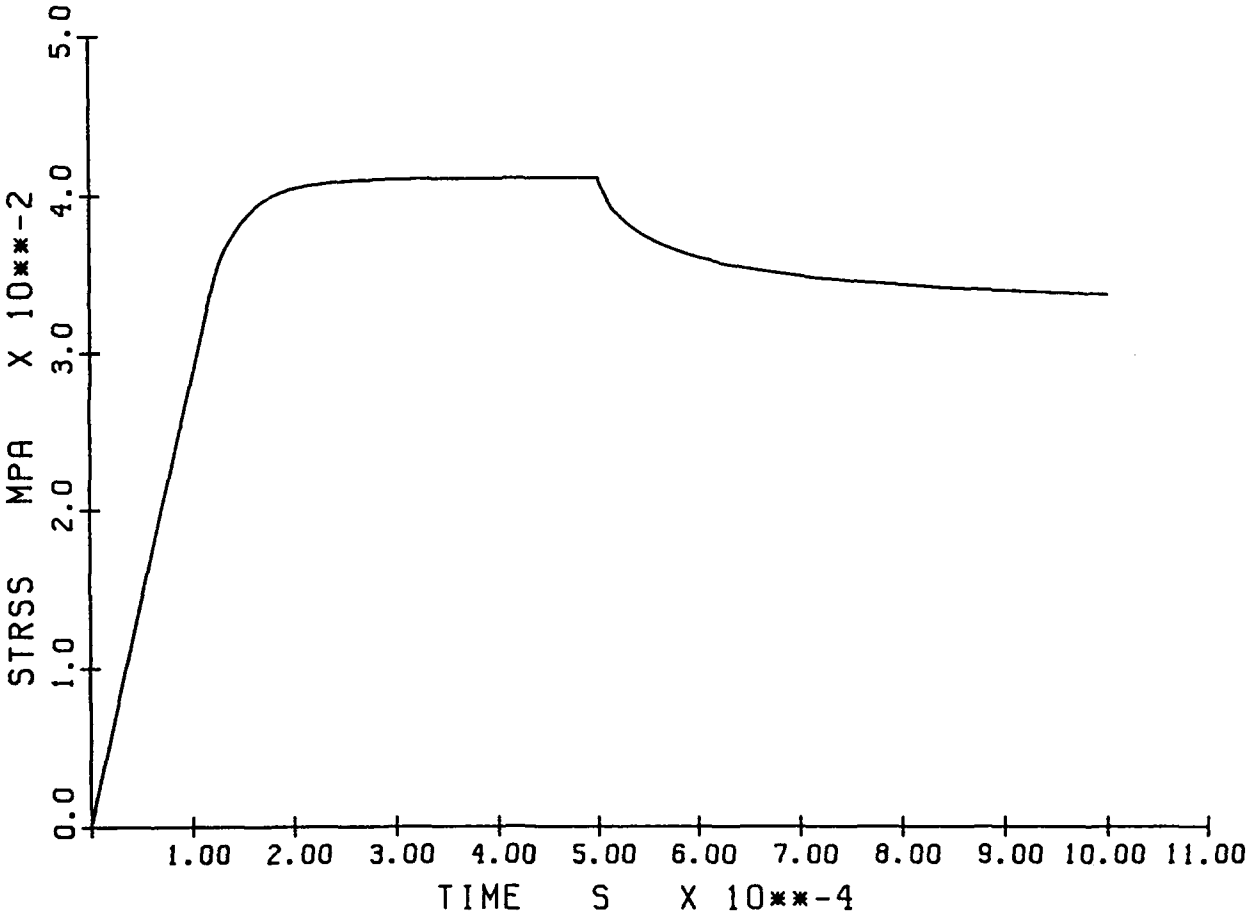

Figure 5.22: Relaxation test of the viscoplastic model

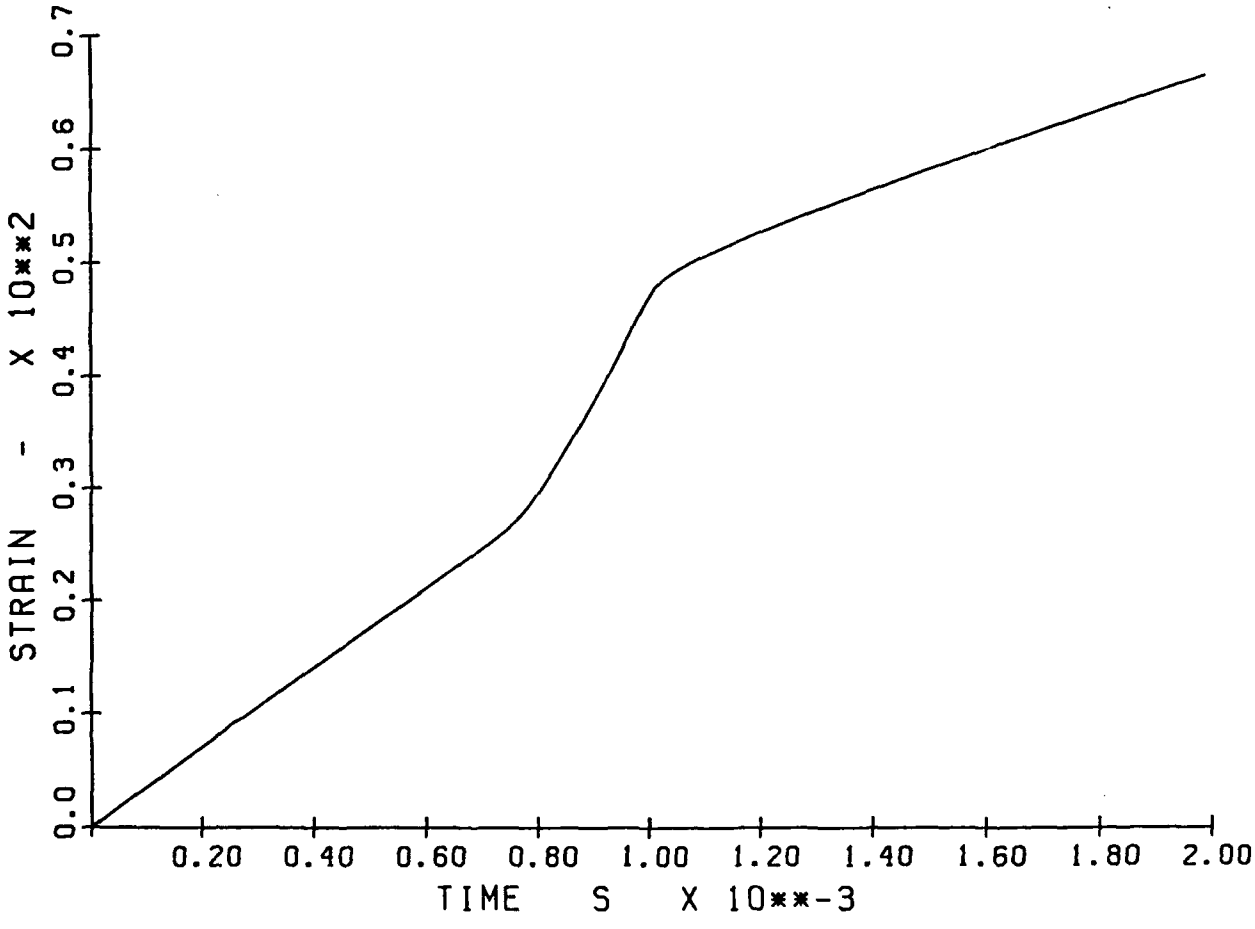

Figure 5.23: Creep test of the viscoplastic model

6 Verification of Numerical Models of Asperity

Numerical modeling of response of surface asperities to contact and friction loads is one of basic components of the new asperity-based interface models developed in this project. In order to verify correctness of our finite element asperity simulations, we performed several tests and comparisons, in particular:

- modeling of elastic sphere in contact with a rigid flat, (Hertz problem). Analytical solution is available for this problem [47,90],
- numerical modeling and experimental measurements for custom-made asperities with strongly pronounced nonelastic properties.

Details of these tests are presented further in this section.

6.1 Elastic Sphere in Contact with a Rigid Flat

In order to verify the contact algorithm and the nonlinear solution procedure, a finite element solution was obtained for the contact of elastic sphere with a rigid flat. The finite element solution of this problem was compared with theoretical solution due to Hertz [47,90]. For a given sphere of radius R and prescribed normal displacements of the flat equal w, the theoretical predictions of the contact radius r, contact area A and total load P are given by:

$$\begin{aligned} \mathrm{r} &= \sqrt{Rw} \\ \mathrm{A} &= \pi Rw \\ \mathrm{P} &= \frac{4}{3}\frac{E}{(1-\nu^2)} R^{\frac{1}{2}} w^{\frac{3}{2}} \end{aligned}$$

The above problem was solved numerically using the following data:

$$\begin{aligned} \mathrm{R} &= 1.0 \\ \mathrm{E} &= 1000. \\ \nu &= 0.3 \\ w &= .001, .002, .005, .01, .02 \end{aligned}$$

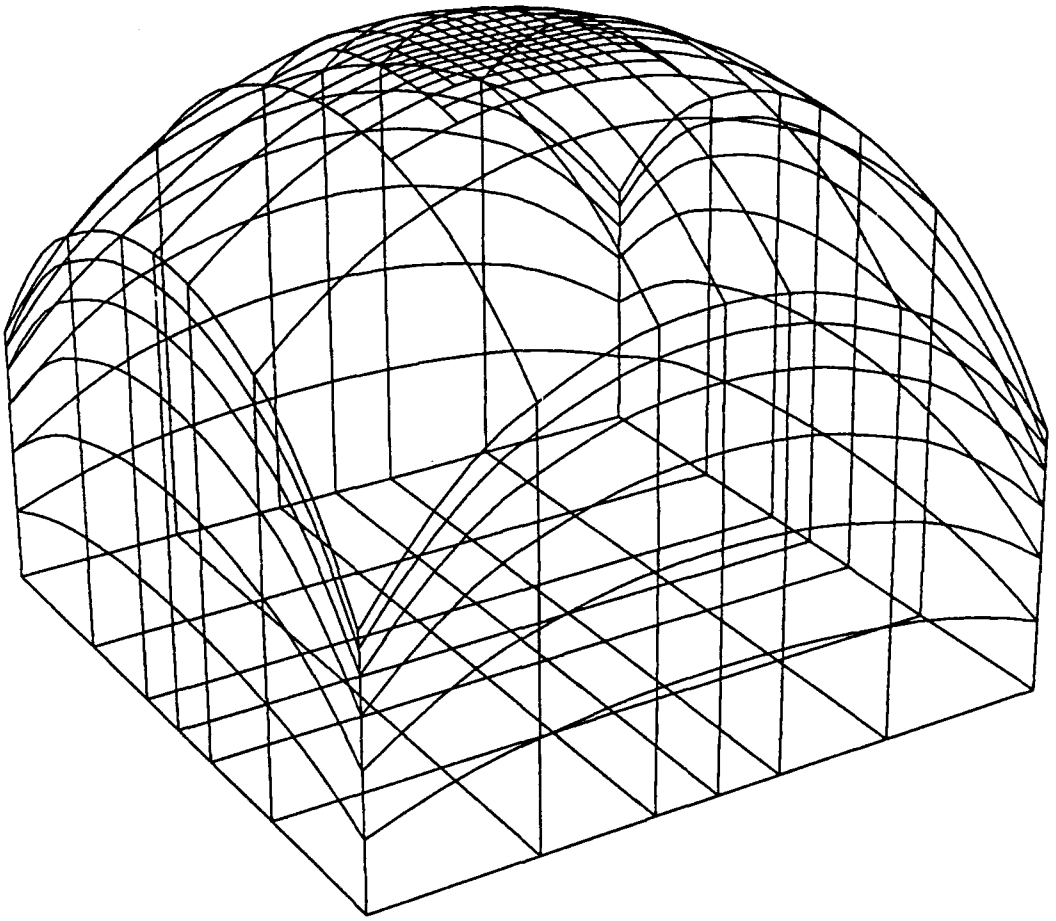

Figure 6.24: Refined mesh for the Hertz problem, w = .02, deformed configuration. Only boundary elements shown.

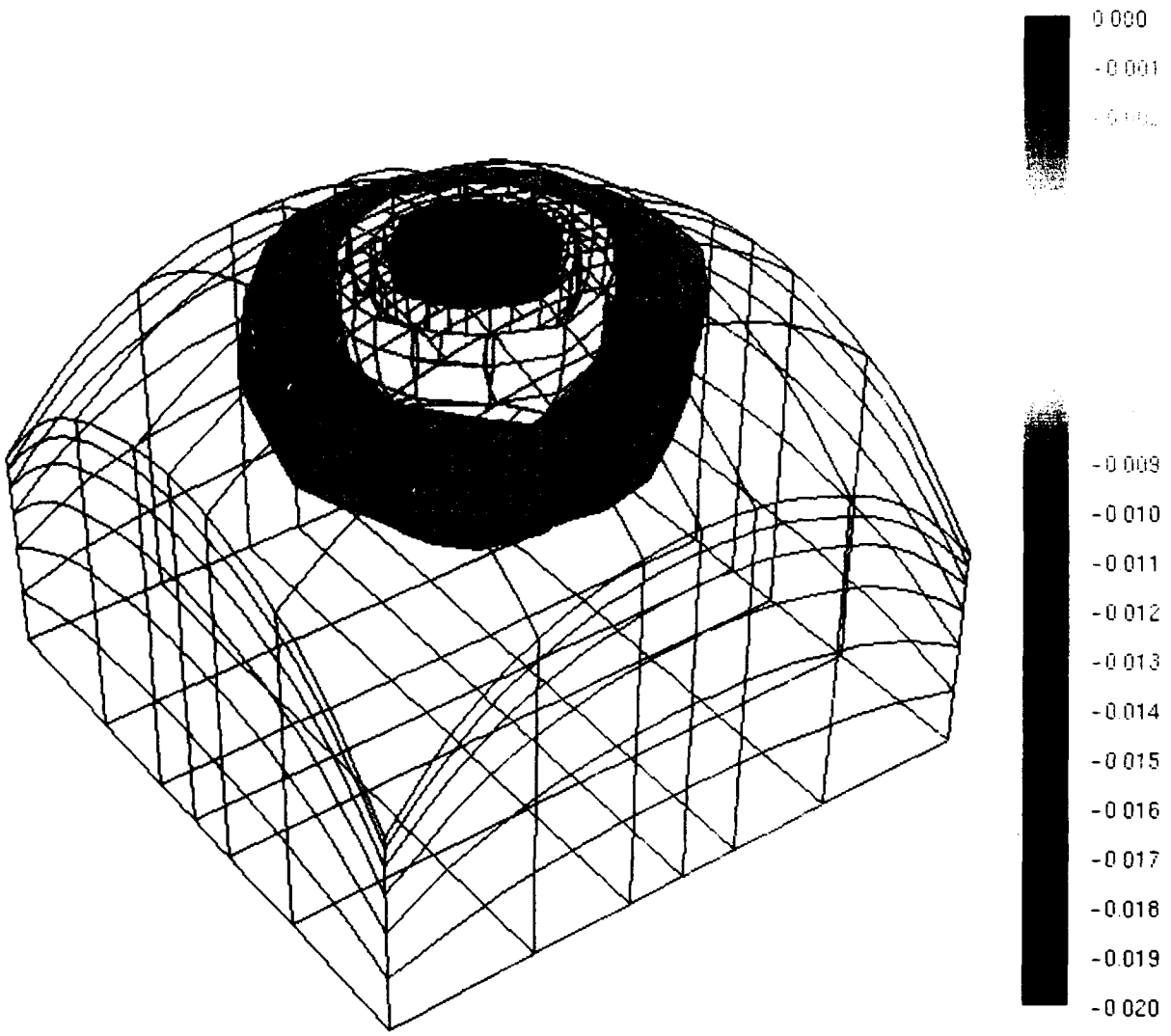

Figure 6.25: Isosurfaces of the vertical displacement for the Hertz problem, w=.02

Due to a localized nature of the contact, the finite element mesh was defined only for a section of the sphere around the contact zone. The problem was solved using the Newton procedure combined with adaptive mesh refinement. An example of the final refined mesh obtained for w=.02 is shown in figure 6.24 (deformed configuration is displayed and only boundary elements are shown for clarity). The same mesh with isosurfaces of vertical displacement is presented in figure 6.25, the slicing plane, with stress σ_{yy}, is shown in figure 6.26, and the error indicators projected on two slicing planes are displayed in figure 6.27.

The results obtained numerically compare favorably with numerical predictions. A detailed comparison of theoretical and numerical results are shown in table 6.28, and the graphical comparisons of predicted contact area and total load are shown in figure 6.29.

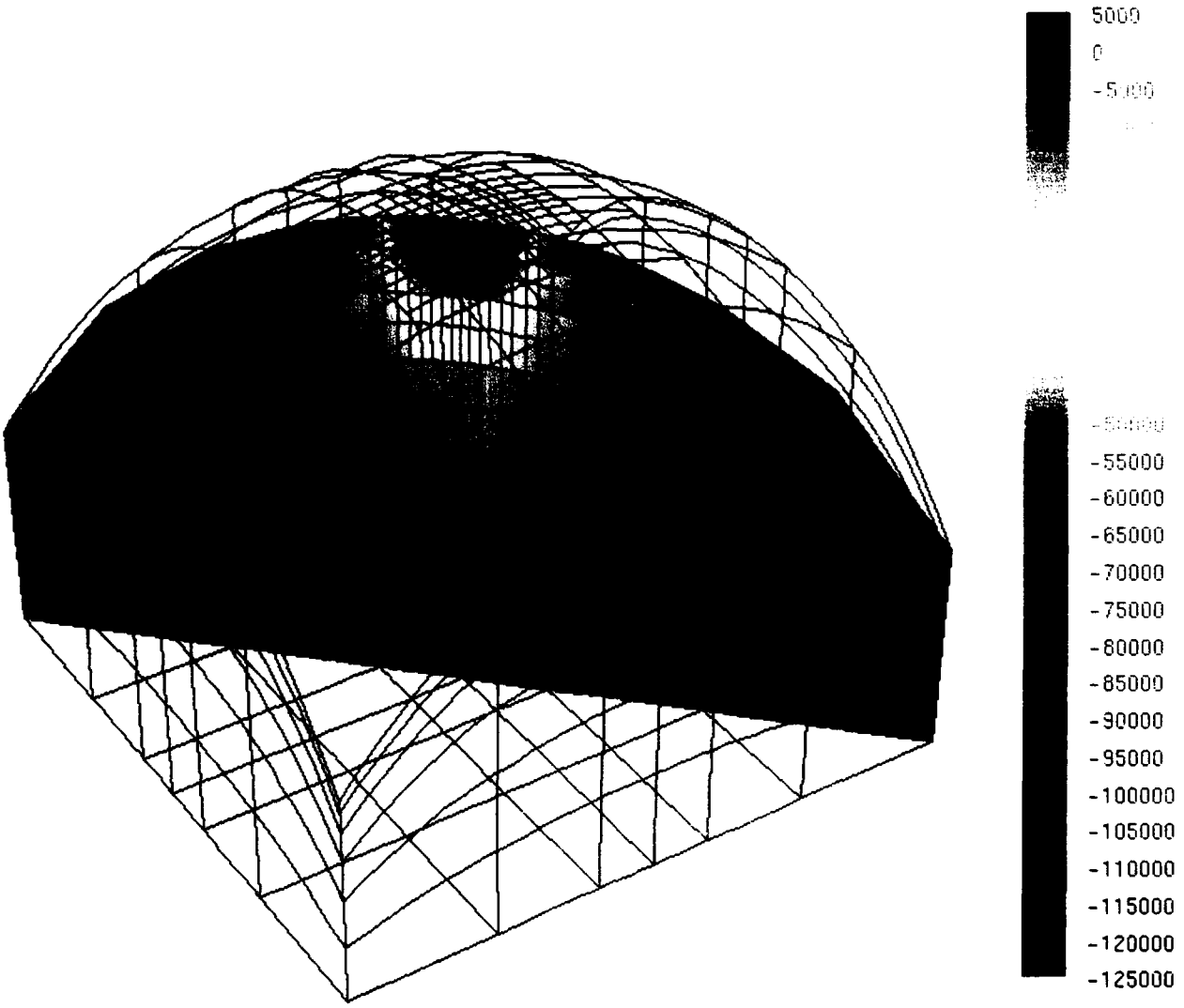

Figure 6.26: Isosurfaces of the σ_{yy} for the Hertz problem, w=.02

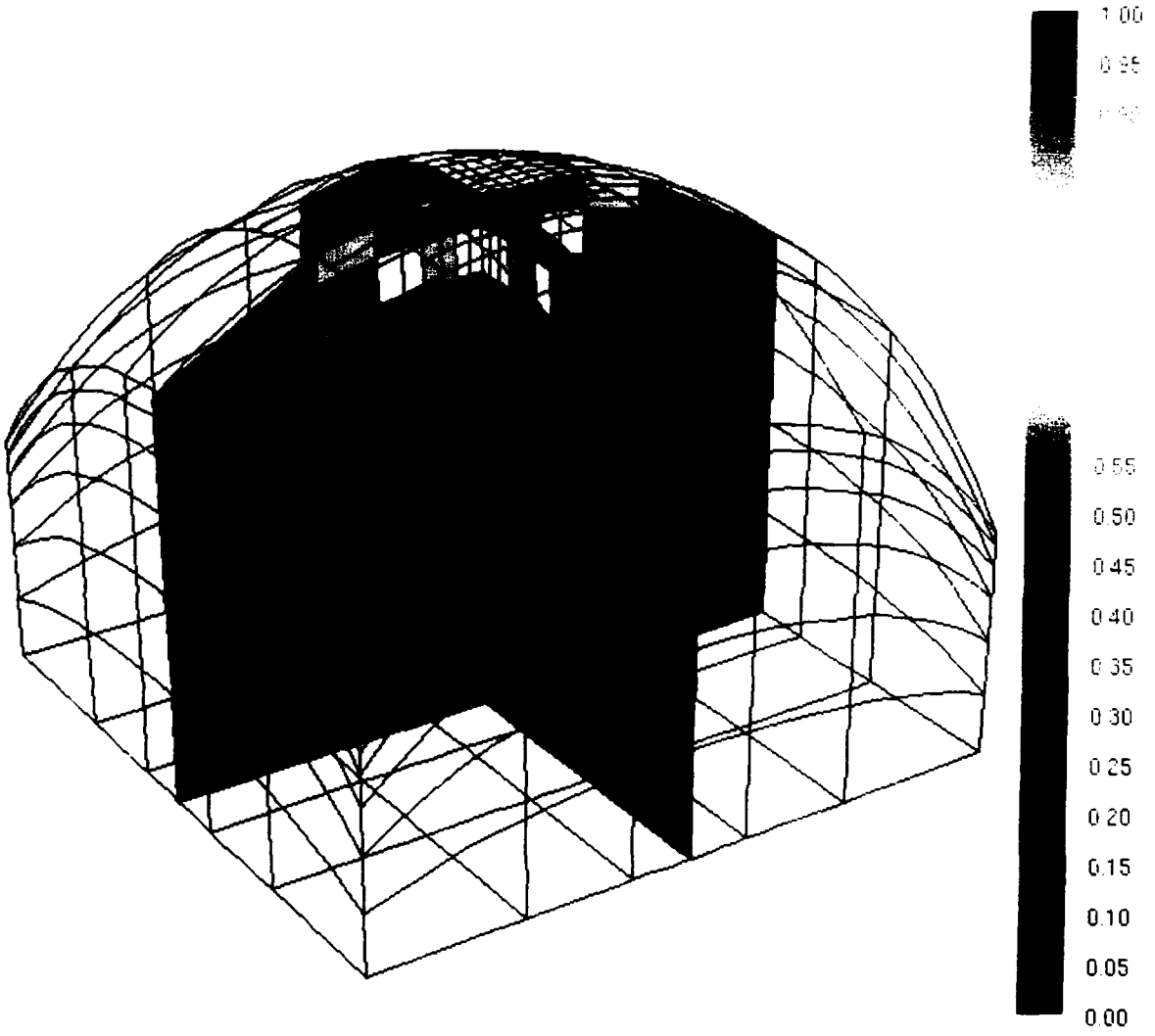

Figure 6.27: Distribution of error indicator for the Hertz problem, w = .02

ELASTIC SPHERE IN CONTACT WITH A RIGID FLAT

E = 1.0000E+03 nu= 0.3000 R= 1.0000

THEORY

Displ	Cont. rad.	Area	Load	Max. pres.
0.00200	0.04472	0.006283	1.3105E-01	3.1286E+01
0.00500	0.07071	0.015708	5.1803E-01	4.9468E+01
0.01000	0.10000	0.031416	1.4652E+00	6.9958E+01
0.02000	0.14142	0.062832	4.1442E+00	9.8936E+01

NUMERICAL

Displ	Cont. rad.	Area	Load	Max. pres.
0.00200	0.04237	0.00564	1.5400E-01	4.3600E+01
0.00500	0.07001	0.0154	5.5400E-01	5.4000E+01
0.01000	0.10092	0.0320	1.5400E+00	7.9200E+01
0.02000	0.14809	0.0689	4.5000E+00	1.0840E+02

Figure 6.28: Comparison of theoretical and numerical results for the Hertz problem

6.2 Experimental Studies of Models of Asperity

In order to verify numerical simulation of nonelastic behavior of asperities, several experimental measurements were performed and then compared with numerical predictions.

These tests included simple tension and compression problems designed to verify nonelastic material constants for aluminum, as well as contact tests for two types of custom-made asperities. In this phase of experiments, which we refer to as Phase I, custom asperities were chosen in order to eliminate random surface factor from the comparisons. In Phase II, which will be performed in the next year of the project, real random surfaces will be considered.

The objective of this Phase I experimental study is to study the deformation of contact surface asperities and to verify the analytical prediction by experimentation. In design of the experimental study, it is initially conceived that the test is to be carried out under a small normal load (500 Lbf) condition. A controlled surface asperities are machined onto both surfaces of an aluminum block. In the test arrangement, the aluminum block is sandwiched between two hardened steel blocks with smooth surfaces, and the steel-aluminum-steel block assembly is compressibly loaded to approximately 500 Lbf. The deformation of asperities on the aluminum block is monitored during loading. After completing the normal loading, a horizontal load is slowly applied to the aluminum block until the block begins to slip. An estimation of the coefficient of friction can thus be made by using the measured normal and horizontal loads, and be compared with that from the analytical prediction. A test apparatus is built for this purpose, and tests are carried out with this apparatus. After reviewing the test results, it is decided that the deformation of surface asperities on the aluminum specimen is too large for the purpose of model verification. The shape of asperity is changed, and the tests are carried out under a normal load of approximately 2.000 Lbf. The results from both arrangements are reported in this section.

6.2.1 The Test Apparatus

A sketch of the apparatus is shown in Fig. 6.30. An aluminum (6061, T4) block of 1' x 1' x 0.25" is sandwiched between two steel blocks of the same dimension as shown in the figure. The V-shaped grooves of angle 45 deg, pitch spacing of 0.1 inch, and depth of 0.125 inch are machined with a specially designed cutter on both surfaces of the aluminum block to simulate the surface asperities. A sketch of the grooves is shown in Fig. 6.31. The surfaces of the steel blocks are machined smooth and (water) quench hardened to RC-30. It should be mentioned that, due to the angle of the cutting tool and the pitch spacing, the tips of the grooves are not in a plane, the heights of tips vary alternatively as shown in the photograph (Fig. 6.31) to be discussed in a later section.

A normal load is applied to the specimen assembly through a mechanical screw jack from the bottom of the apparatus. The normal load is monitored with a small "load transducer" of capacity 500 Lbf. The normal deformation of the simulated asperities on aluminum block is measured with a "proximate sensor" with an operation range from 0 to 0.1 inch. The sandwiched specimen assembly is first installed in position, and an initial load of approximately 50 Lbfs is applied to the specimen prior to "zero adjustment" of the recording instrument

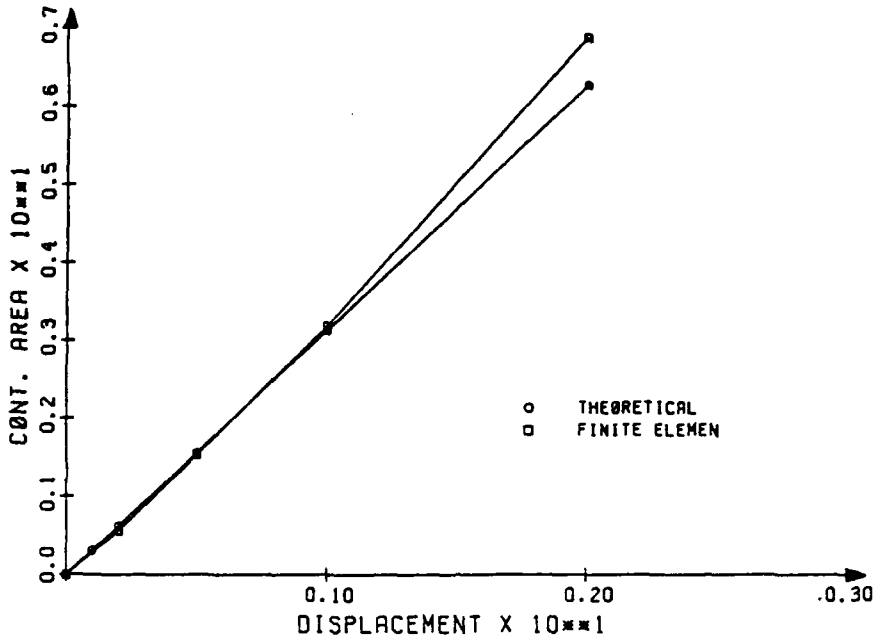

a)

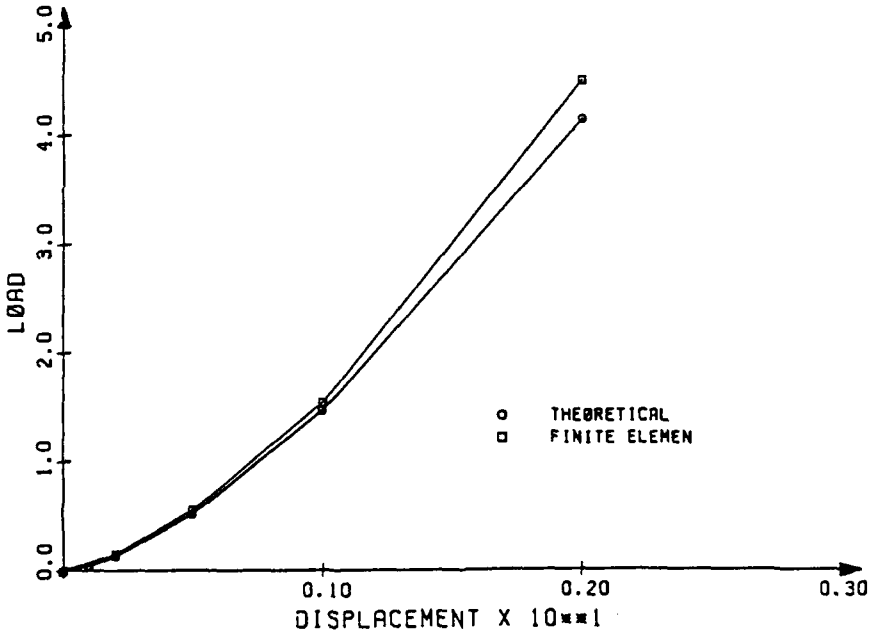

b)

Figure 6.29: Comparison of theoretical and numerical results for the Hertz problem; (a) displacement versus contact area, and (b) displacement versus contact load

(an X-Y plotter). A total normal load of 500 Lbs is then applied to the specimen at a rate of approximately 10 Lbf per minute. After the normal load has reached 500 Lbf, a horizontal load (by lead blocks and beads) is slowly applied to the aluminum block until the block starts to slide. The horizontal load is monitored with a ring-shaped load transducer (laboratory built) as shown in Fig. 6.30.

Note that even with very precise calibration of the test apparatus, certain compliance or "setting in" occurs during loading and pollutes the measurements. This is especially true in case of high loads and very small displacements considered in this experiment. It is a standard practice in experimental tests to discard the initial part of the load curve and appropriately translate the remaining part. In this section, we present results in the "raw" form, but numerical comparisons refer to corrected graphs.

6.2.2 Tests Results From the Above Apparatus

Two tests are carried out. A representative force-deformation plot is shown in Fig. 6.32. It is seen that there is an appreciable amount of plastic deformation of the surface asperities on the aluminum block (neglect the bulk deformation of both aluminum and steel blocks) when the block assembly is loaded to 500 Lbf. A horizontal force is then slowly applied to the aluminum block. It is visually observed that the aluminum block starts to slip when the horizontal load reaches 108 Lbf. Since there are two contact surfaces between the aluminum block (with asperities on both surfaces as shown in Fig. 6.31) and steel blocks (with smooth surfaces) in the test arrangements, the nominal coefficient of friction is $(108/2)/500 = 0.108$.

6.2.3 Deformation of Asperities Under a Larger Normal Load

The asperities shown in Fig. 6.31 have pointed tips, the deformation of tip is difficult to calculate. It is then decided to change the geometry of asperity as those shown in Figs. 6.31(b) and 6.31 (c). In Fig. 6.31 (b), the asperity is modeled as a 45-deg grooved with a truncated tip. In Fig. 6.31 (c), the asperity is modeled by spaced circular rods. The force-deformation relationship for the specimen with asperities as shown in Fig. 6.31 (b) and 6.31 (c) are measured. The test arrangements are the same as that described in the previous section. Since the maximum load in these test are much higher than 500 Lbf, the tests are carried out and the representative force-deformation curves are shown in Figs. 6.33 and 6.34, respectively. A photograph of the cross-section of the deformed grooves is shown if Fig. 6.35. It is seen that only the alternate grooves were deformed. There are seven grooves on each surface of the aluminum block, therefore only eight (four on each surface) of them are deformed. Since the maximum horizontal load required to move the aluminum block in this exceeds the capacity of the ring load cell used in previous section, the horizontal pulling test has yet to be carried out (we need to build a new load cell and loading frame).

Finally, a test for the compressive property of the aluminum used in this study is carried out. The stress-strain curve from a 0.25" dia x 1" long aluminum (6061, T4) specimen is shown in Fig. 6.36. Again, the test is carried out at a slow loading rate (approximately 20 Lbf per minute).

A similar test under tensile stress state was also performed, and the results are shown in Fig. 6.37.

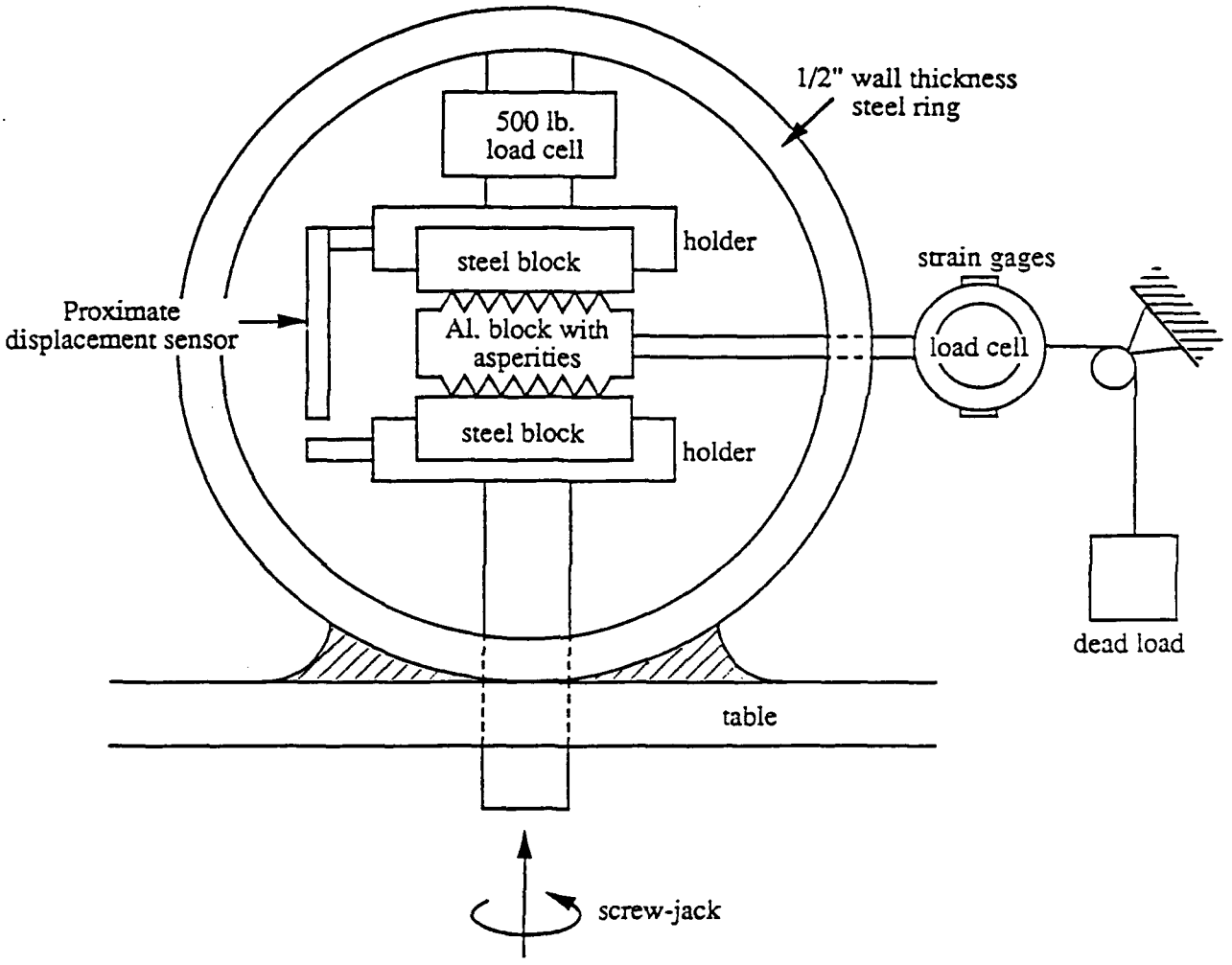

Figure 6.30: A sketch of test apparatus (not to scale).

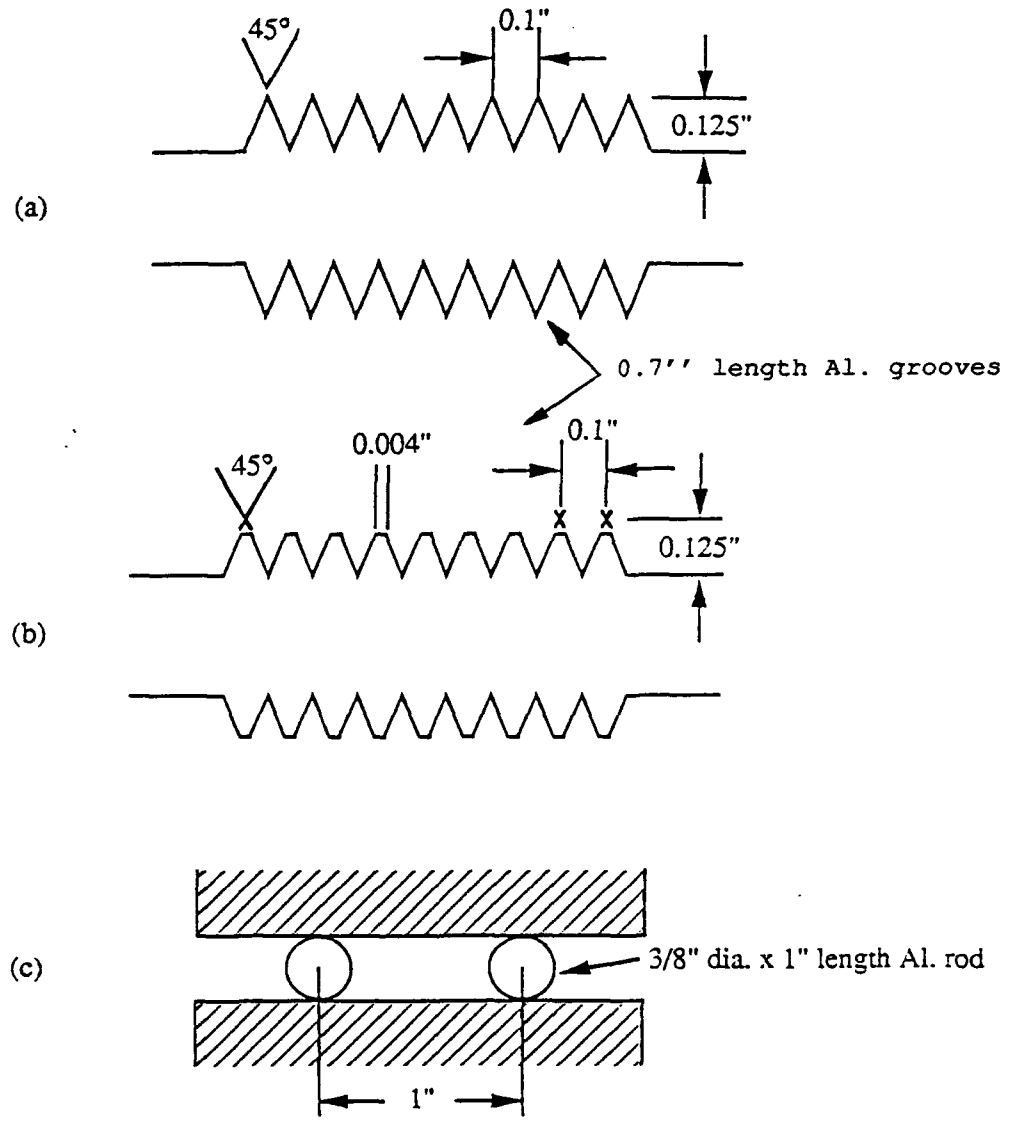

Figure 6.31: Different models of asperities studied experimentally.

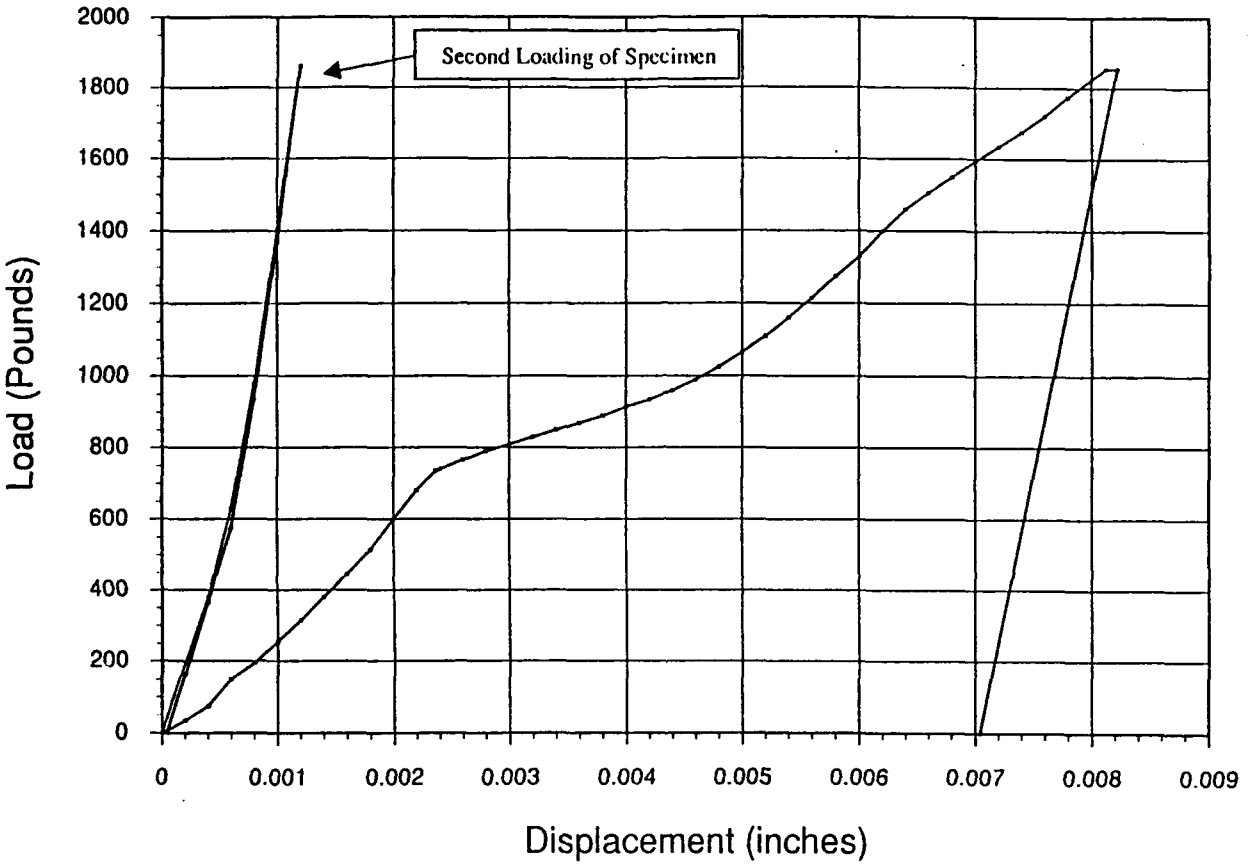

Figure 6.32: Load-displacement curve for V-shaped asperity

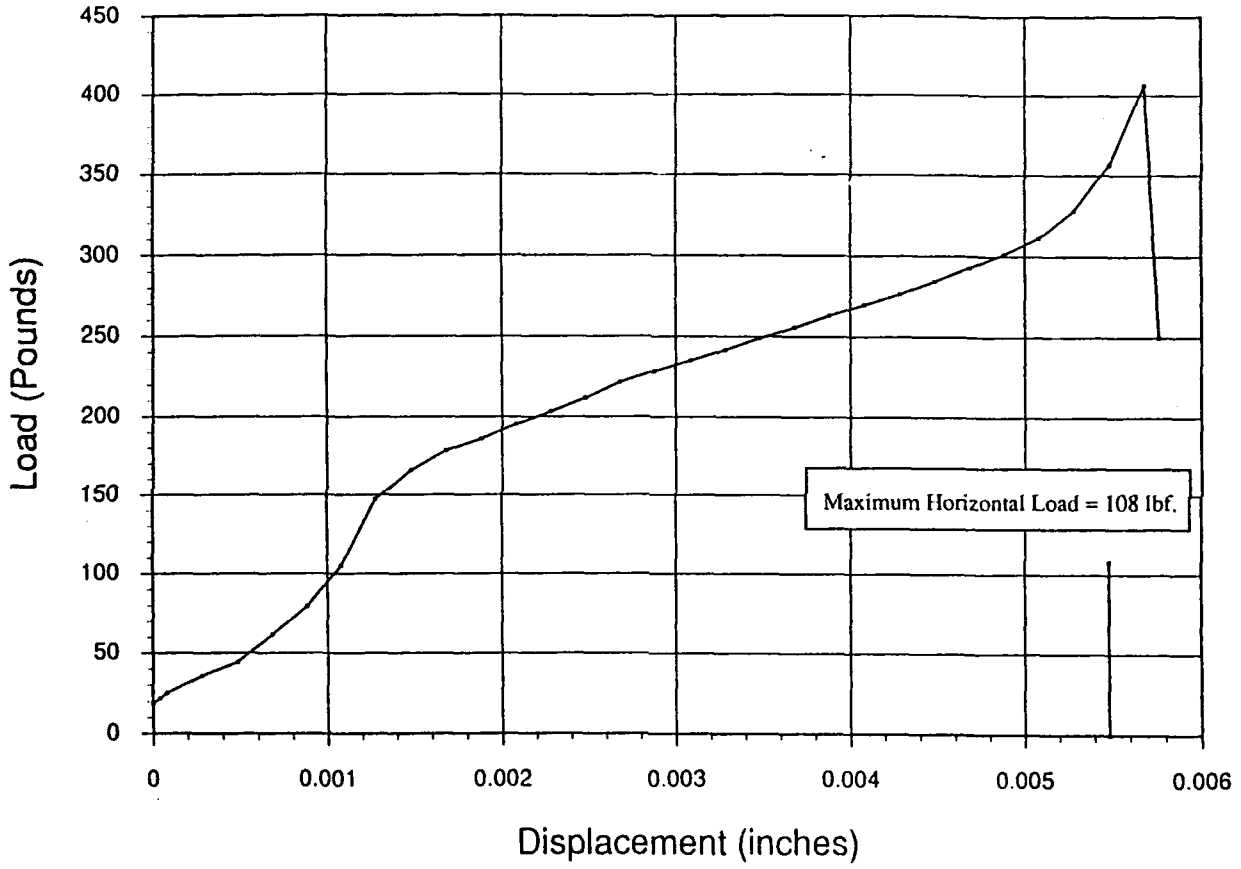

Figure 6.33: Load-displacement curve for truncated asperity

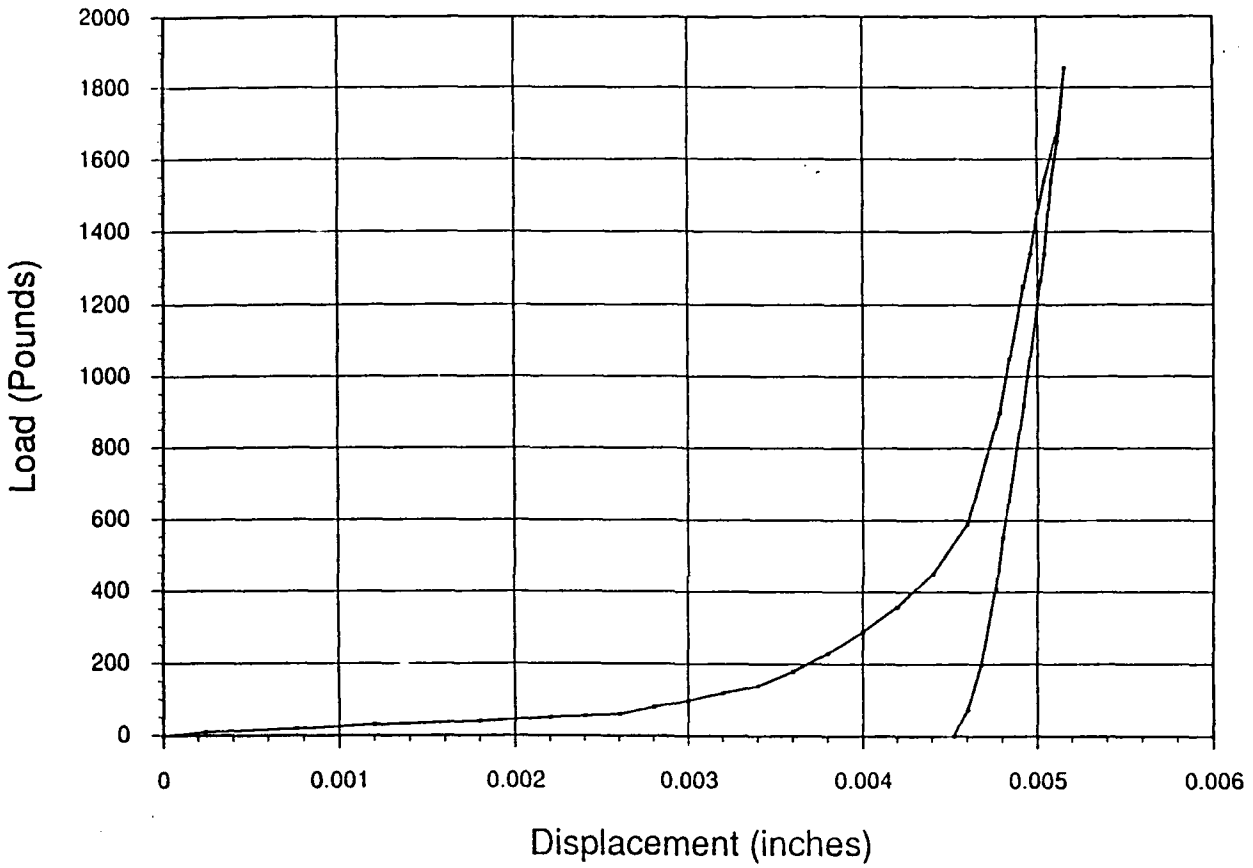

Figure 6.34: Load-displacement curve for cylindrical asperity

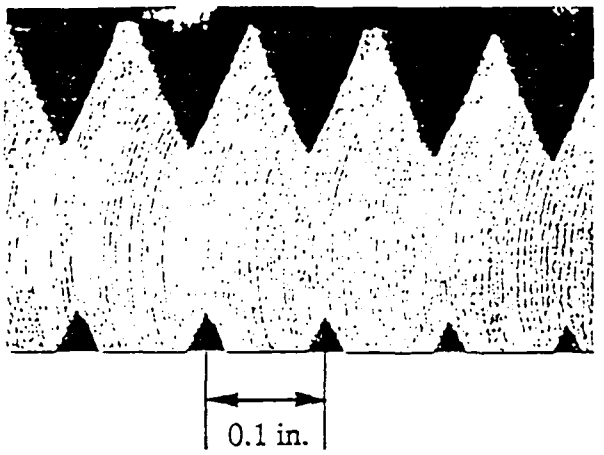

Figure 6.35: A photograph of deformed asperity

6.3 Numerical Simulation of Experimental Measurements

6.3.1 Viscoplastic Uniaxial Stress State Numerical Test

The aim of this test was verification of viscoplastic material constants for aluminum 6061 T4. Bodner-Partom model of viscoplastic materials uses 14 material constants. However, for aluminum alloys at room temperature the model can be simplified and then only 7 material constants are of primary importance. Their values obtained from reference [ ] for slightly different heat treatment (T6) are listed below:

E = 73.9 GPa
ν = 0.33
z_0 = 450 MPa
z_1 = 550 MPa
m_1 = 0.12 MPa^{-1}
D = 10^8
n = 5.0

In order to verify these values, the results obtained with these constants were compared with simple compression and tension experimental tests. The test of uniaxial compression failed to provide any useful data because bifurcation of the specimen was observed and the state of stresses was not uniaxial. The adequate verification of material constants was possible using the results of tensile test. They indicated that the Young modulus was in fact smaller and the yield limit greater than assumed initially (the differences reached about 10 percent). In order to have a more accurate model the Young modulus and the kinematic parameter were changed. The new values are

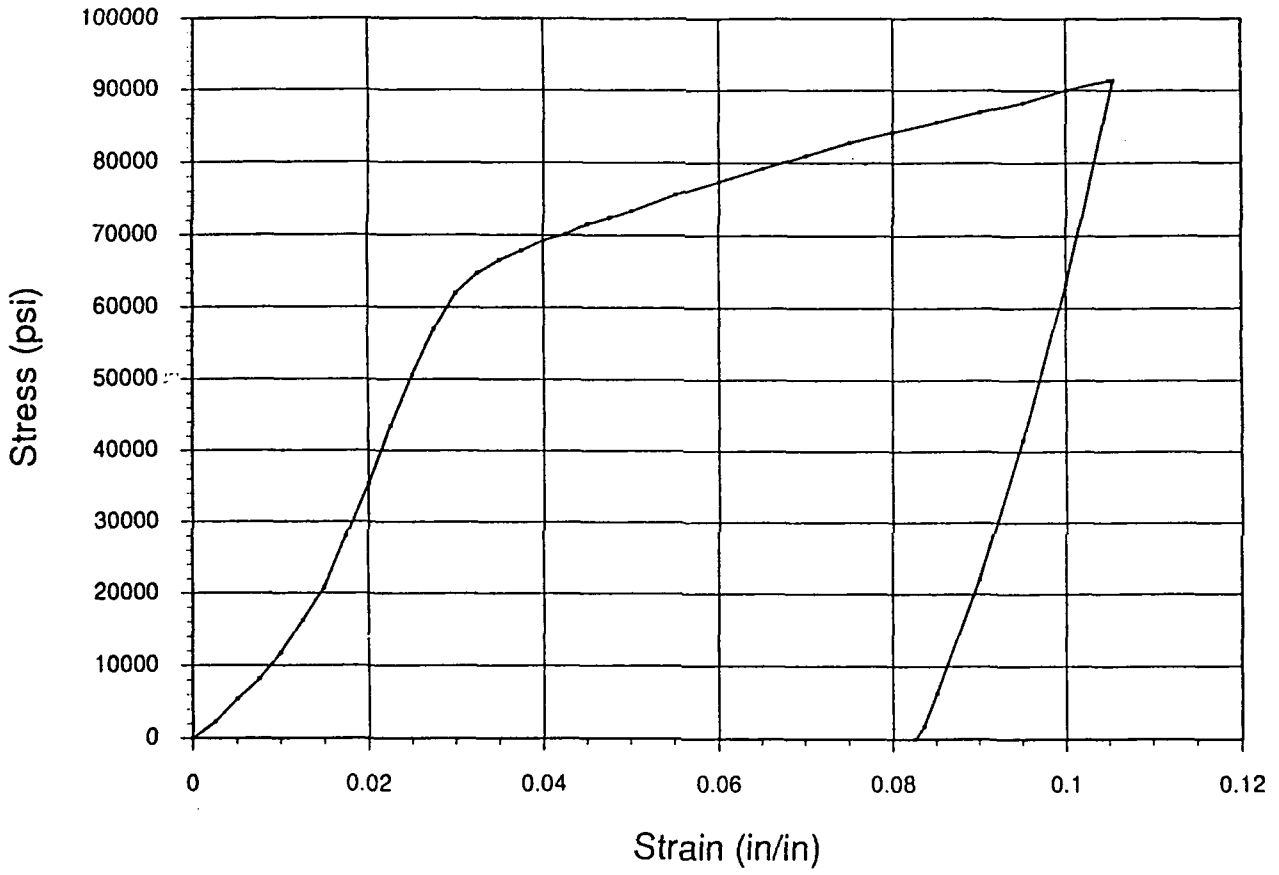

Figure 6.36: A compressive stress-strain curve for aluminum

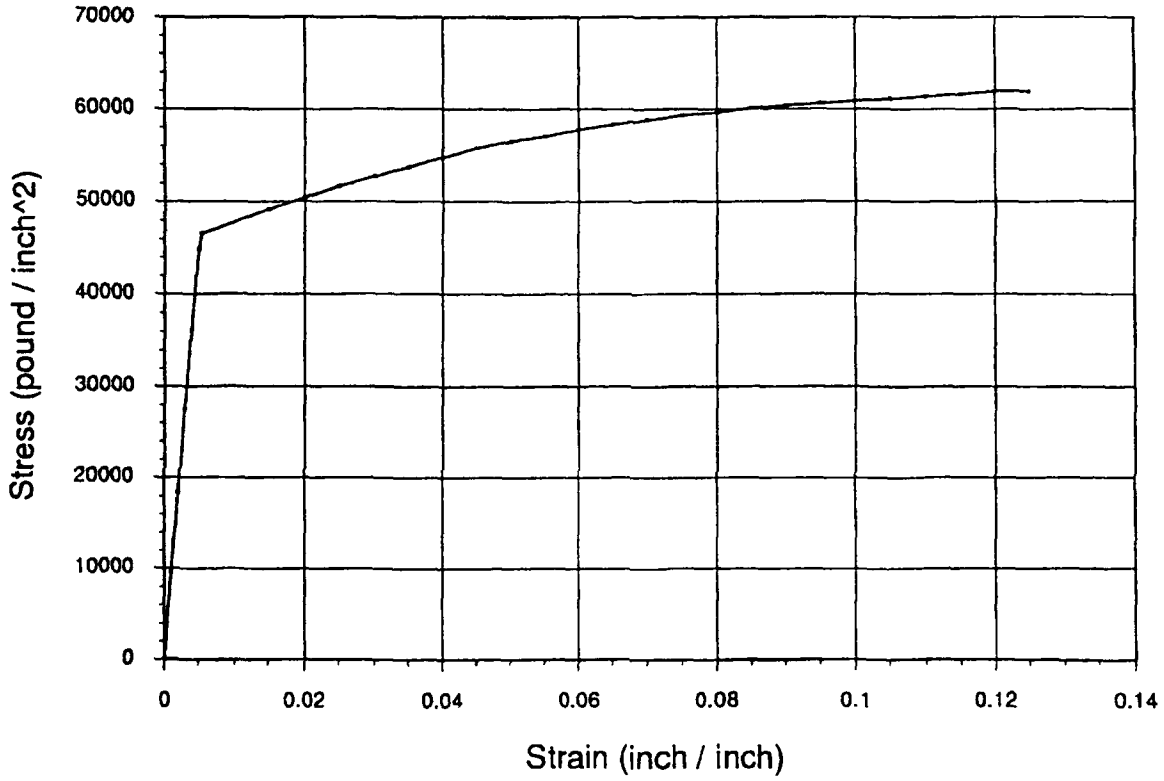

Figure 6.37: A tensile stress-strain curve for aluminum

E = 65.0 GPa
n = 5.8

So modified material constants were used in further computations. Fig. 6.38 shows the plot of stress-strain relation for initial and modified material constants in comparison with the experimental results.

6.3.2 Viscoplastic Cylindrical Asperity

Aluminum cylinder was used as a model of a "macro asperity". Numerical and experimental tests were carried out. It was assumed that the cylinder can be analyzed as a 2D case. Original mesh used for discretization of a fragment of a circle is shown in Fig. 6.39. After the first computation was completed the mesh was automatically refined. It is shown in Fig. 6.40. The viscoplastic results obtained at both meshes as well as an elastic solution for the first mesh are compared in Fig. 6.41. The conclusions are that:

- behavior of the specimen under applied loading is almost elastic,
- viscoplastic solution is reasonable because it gives smaller values of the contact force,
- the second mesh gives results which can be treated as a final numerical solution (the difference between solutions obtained at coarse and fine meshes is small.)

The numerical and experimental solutions are compared in Fig. 6.42. Note that the experimental results have been rescaled. Instead of the total force - total displacement relation measured in the experiment, Fig. 6.42 shows force per unit length for upper half-cylinder (2 times less than measured). Moreover, metric units were used.

It can be observed that the numerical results compare favorably with experimental measurements. Recall, however, that the experimental data were translated, to correct for settling in the apparatus (see Section 6.1).

6.3.3 Viscoplastic Custom Surface Model

Comparisons of results for a model truncated V-shaped of asperity are described in this section. Two meshes which were used for discretization of this specimen are shown in Fig. 6.43 and 6.44. Numerical results for both meshes are shown in Fig. 6.46 and 6.45. While for the cylindrical model the behavior of the material was almost elastic (maximum nonlinear strain was less than 0.4%), in this case the influence of yielding was significant. Maximum nonlinear strain was about 80%. It means that at least locally solution is beyond the theory of small strains which we use. The comparison of numerical results and experimental ones is shown in Fig. 6.47.

A good agreement of results can be observed for both models of asperity.

Some of unevitable sources of discrepancy are the following

- error of experimented measurements,
- error of discretization of the domain,
- error of modeling of inelastic behavior of the material,
- unknown deformation history of the specimens, prior to the experiment,
- errors of time-integration and other numerical errors.

Comparison of numerical and experimental results as well as the basic numerical tests allow to state that the mathematical model and the computer code work properly.

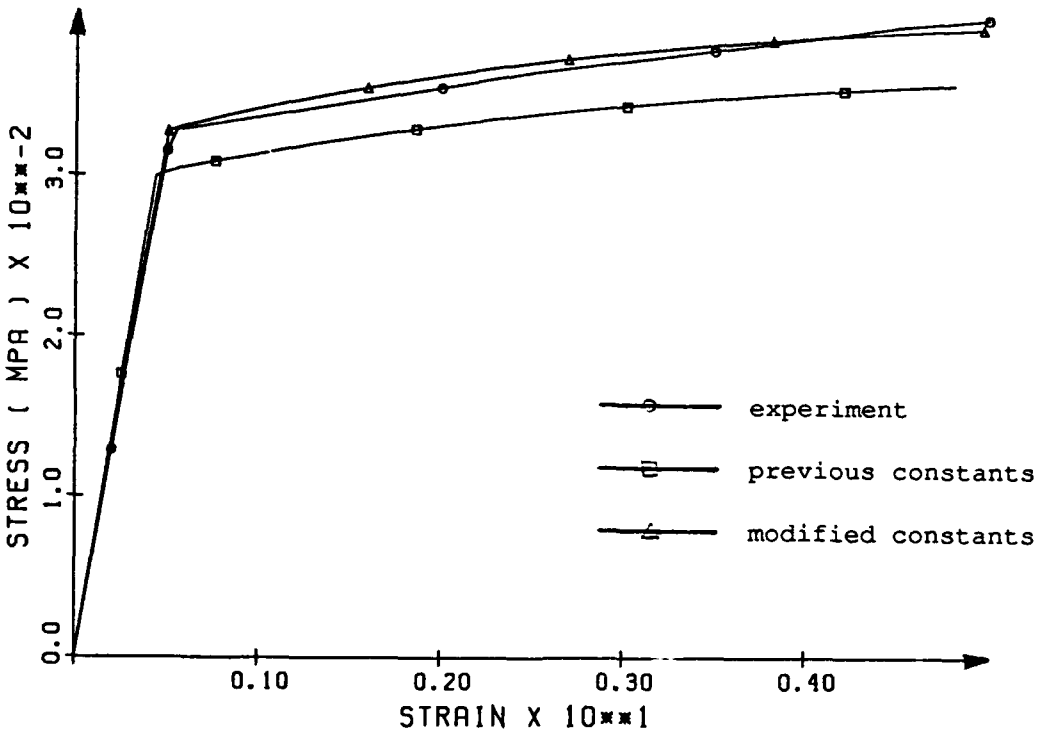

Figure 6.38: Comparison of stress-strain relation behavior for uniaxial tension test.

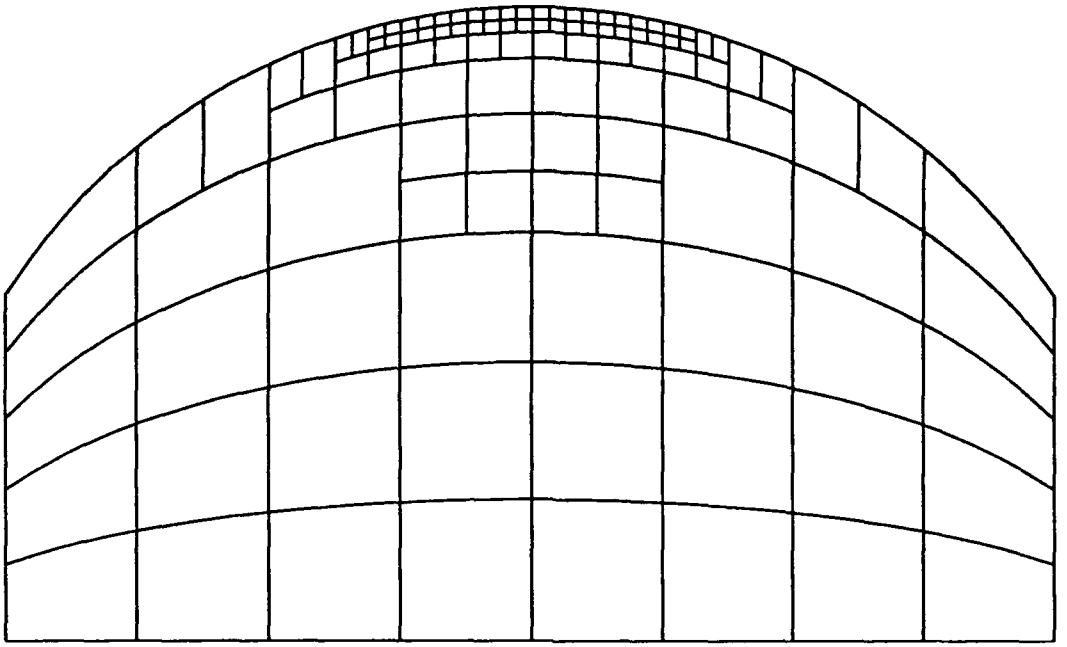

Figure 6.39: Original discretization of the cylinder

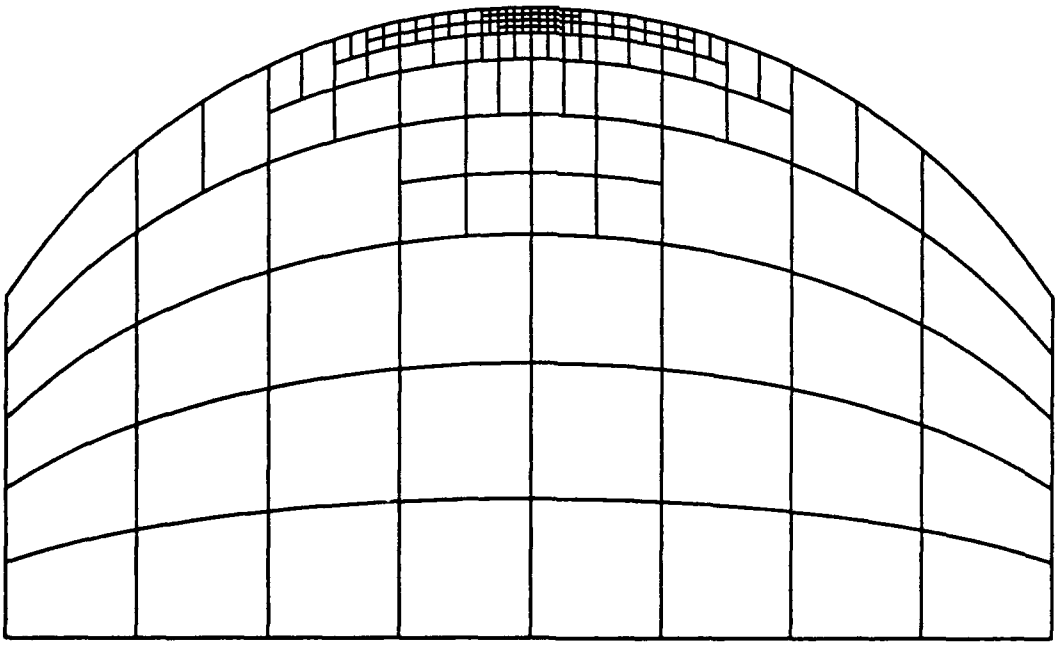

Figure 6.40: Refined discretization of the cylinder

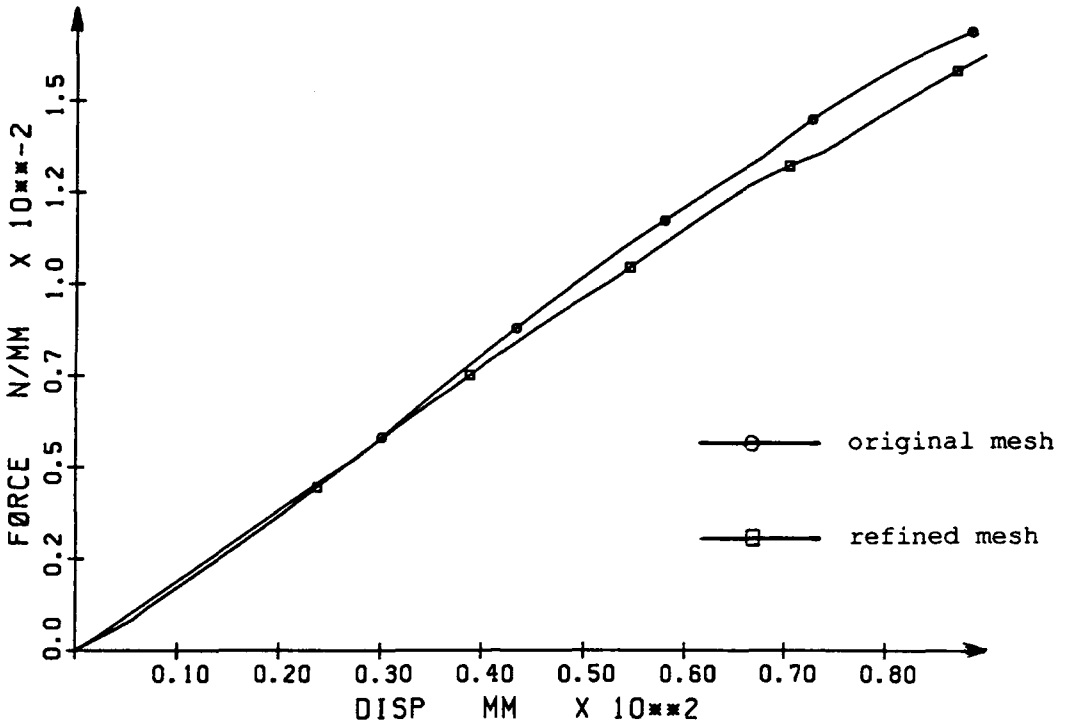

Figure 6.41: Numerical results for the cylinder

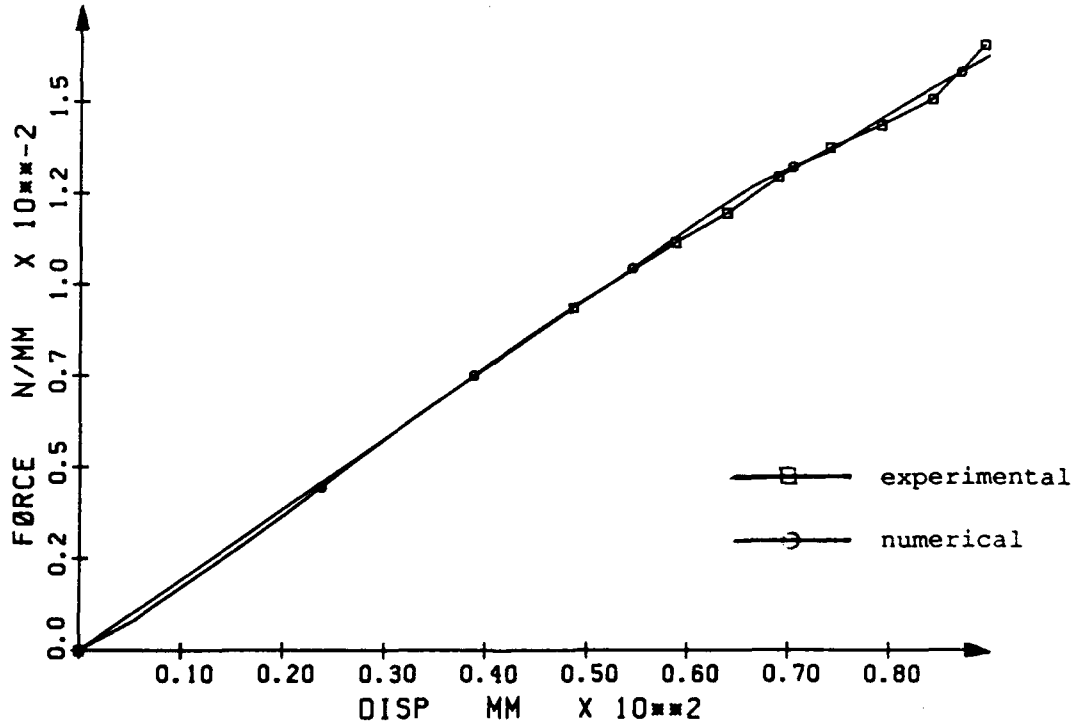

Figure 6.42: Comparison of numerical and experimental results for the cylinder

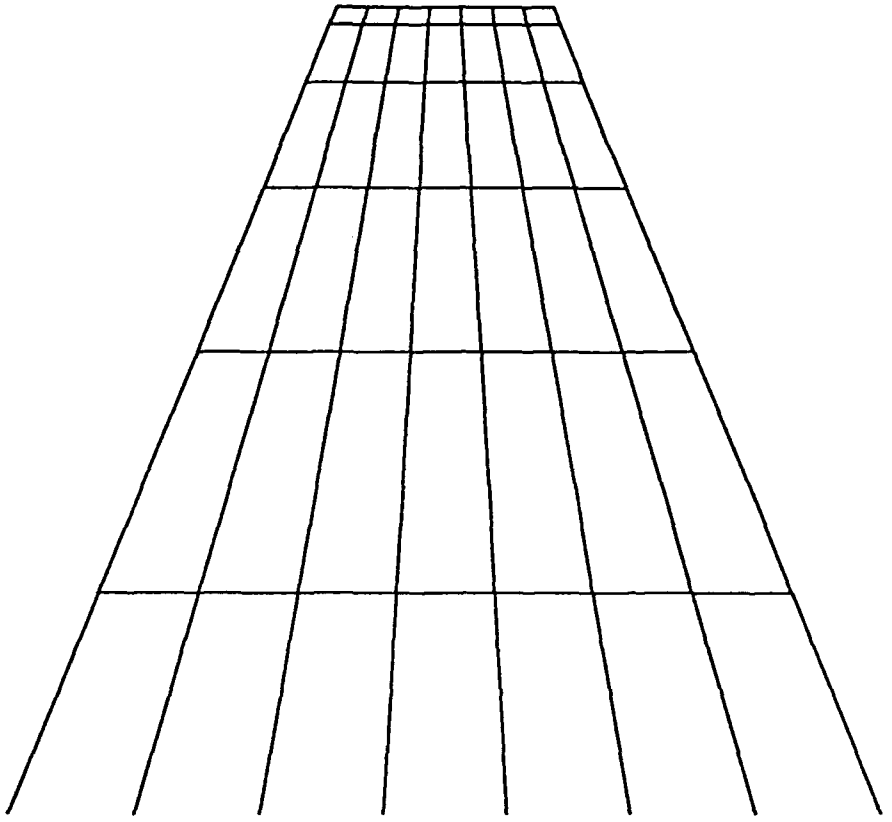

Figure 6.43: Original discretization of the second specimen (truncated V-shaped asperity)

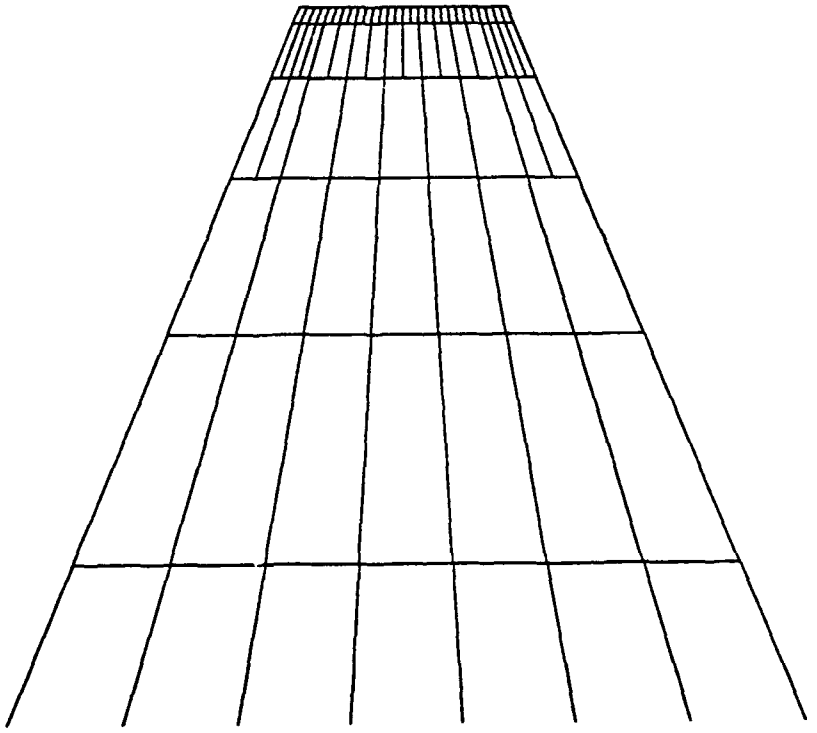

Figure 6.44: Refined discretization of the second specimen

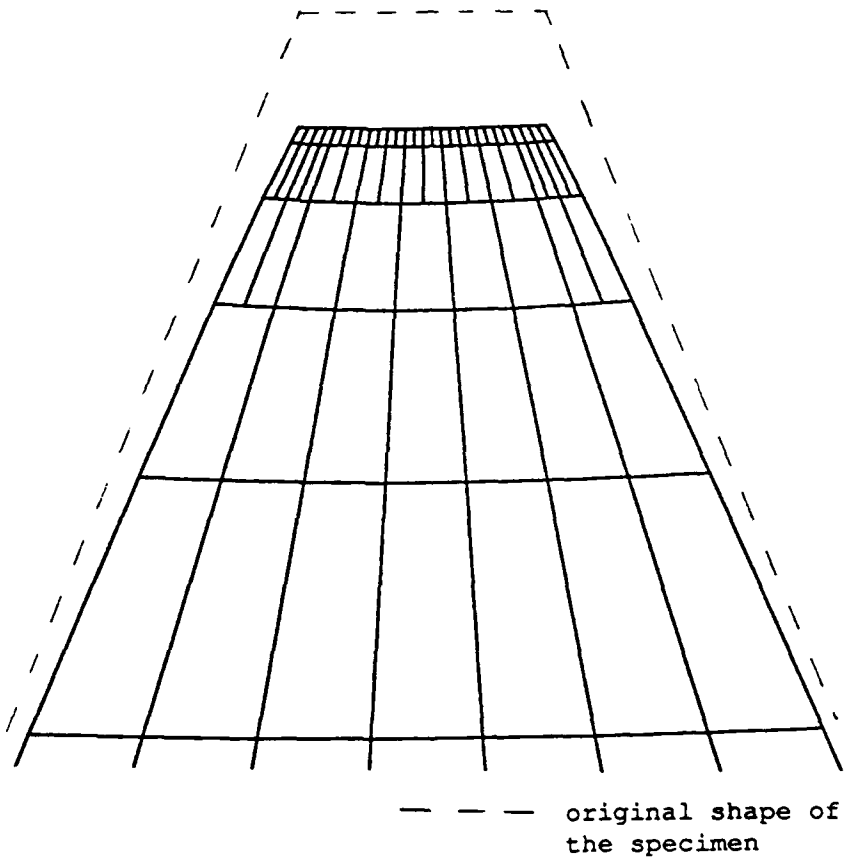

Figure 6.45: Deformation of the second specimen

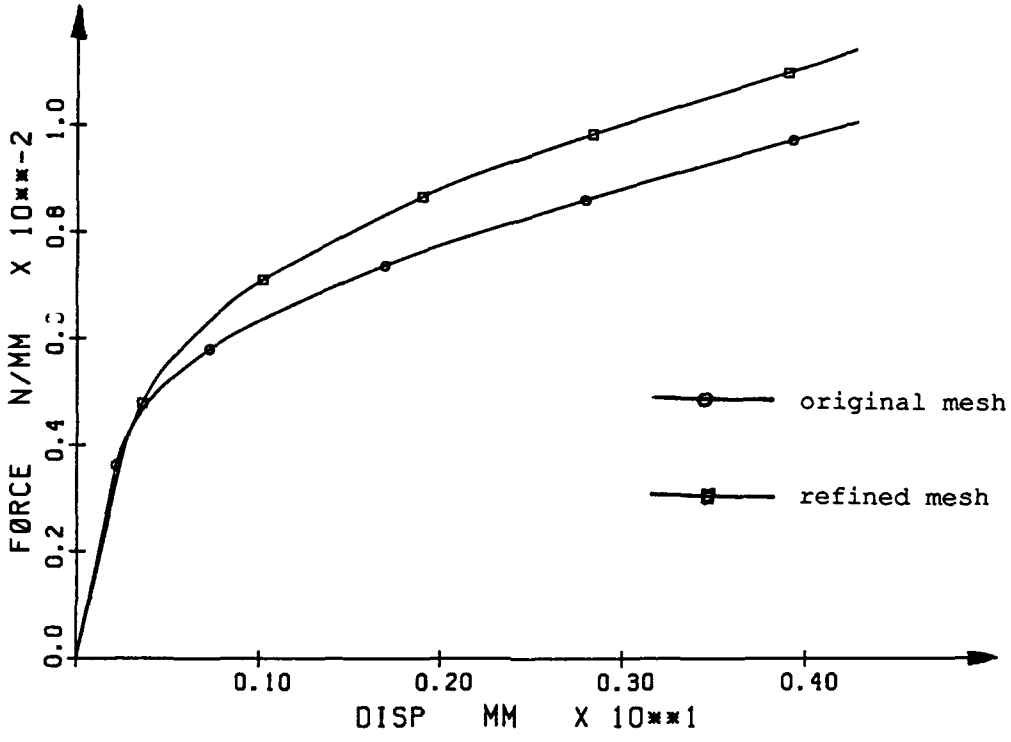

Figure 6.46: Numerical results for the second specimen

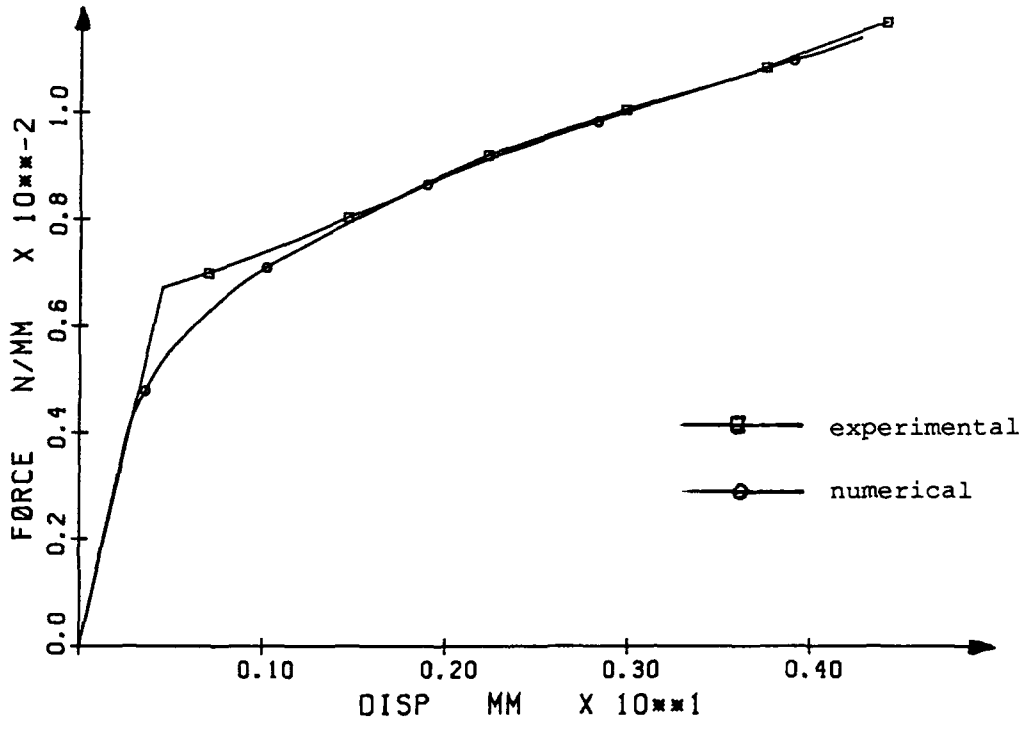

Figure 6.47: Numerical and experimental results for the second specimen

7 A Simple Asperity-Based Contact Model

The results of elastic solution of spherical contact problem were used for initial tests of a complete statistical homogenization procedure. In particular, we compared our finite element based predictions with a classical asperity-based contact model due to Greenwood and Williamson [44]. This is one of historically first asperity-based models, derived under the following simplifying assumptions:

- the tips of asperities are spherical,
- all asperities have the same radius of curvature R,
- asperity height is a random variable with Gaussian distribution,
- contact is elastic and described by the theoretical solution of the Hertz problem.

Note that although this model is much simpler than the ultimate objective of this project (random asperity height and curvature, nonelastic deformation, etc.), it provides a very good initial test for the homogenization procedure. Importantly, our modeling of this problem differs from Greenwood's approach in that:

- solution of elastic contact problem has been obtained from finite element modeling, rather than from Hertz theory,
- expected values of contact load and area have been calculated using numerical quadrature, instead of analytical integration.

Comparison of our results with Greenwood-Williamson theory will provide a good measure of errors introduced by these numerical techniques. Recall, that we are using numerical methods is this work because for real engineering surfaces there exist no closed analytical solutions of the contact problem and of the homogenization procedure.

The simulation of the Greenwood-Williamson model was performed for the following set of parameters:

$$\begin{aligned} R &= 0.1414\ mm \\ \sigma_p &= 7.07106 \times 10^{-4}\ mm \\ \nu &= 0.3 \\ E &= 321.7335\ kG\backslash mm^2 \\ n &= 300\ peaks\backslash mm^2 \end{aligned}$$

where R is the radius of asperity tips, σ_p is the standard deviation of asperity height and n is the surface density of asperity peaks. The results are presented in figure 7.48, which shows respective comparisons of load-separation and load vs.contact area curves. It can be seen that the difference introduced by numerical modeling of asperity and numerical integration of expectation values is within acceptable bounds (note that these differences could be further reduced by application of finer meshes for the asperity contact problem.)

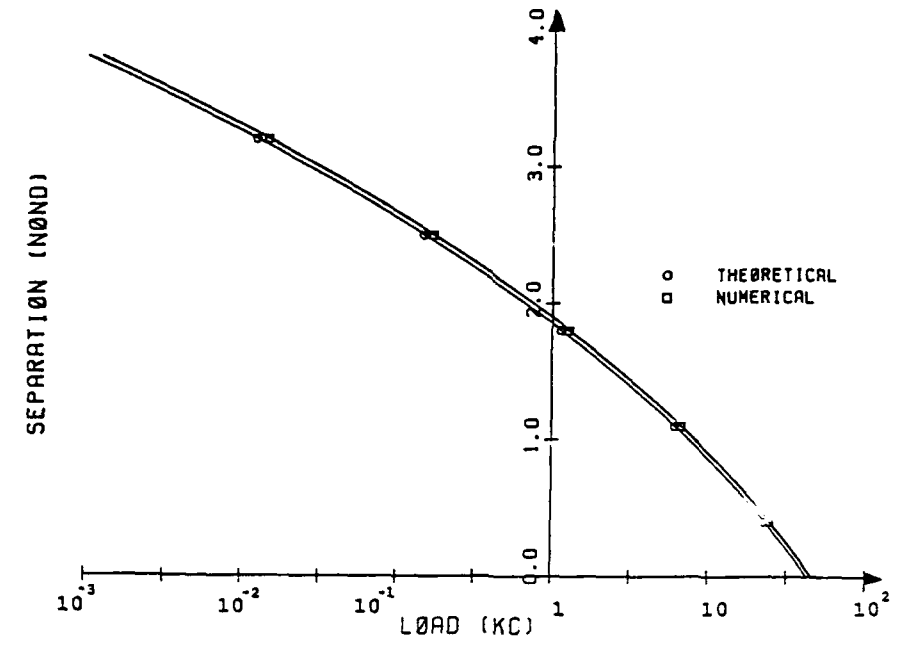

a)

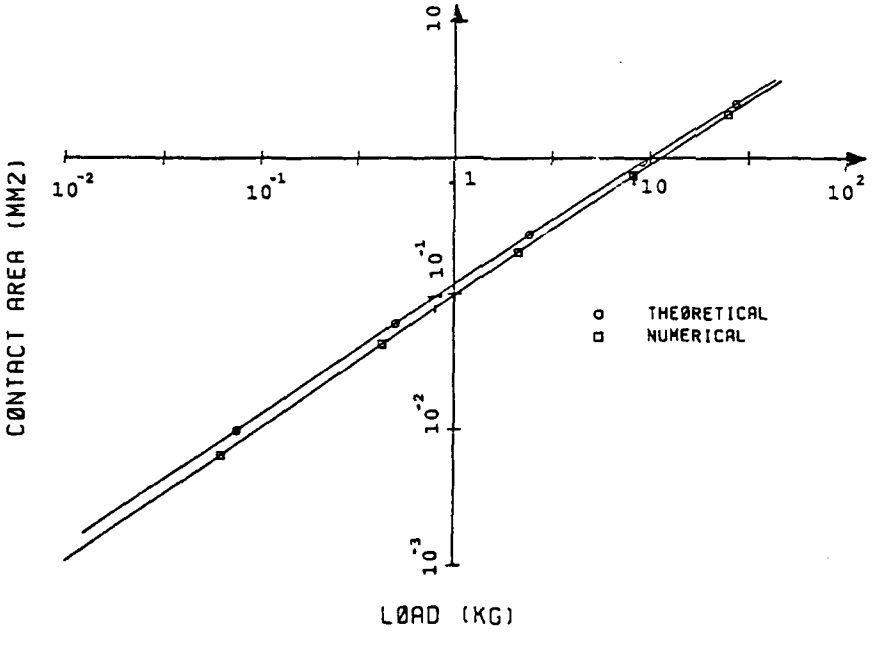

b)

Figure 7.48: Comparison of Greenwood-Williamson theory with numerical predictions; (a) load-separation curve and (b) load-area curve.

8 Conclusions and Research Forecast

In the second year of this project the effort has been focused on the development of a finite element code for modeling nonelastic surface asperities, as well as on the design and performance of the verification experiments. This was followed by theoretical and numerical verifications of the numerical models of surface asperities. To model the deformation of an asperity, a generic h/p adaptive finite element kernel (developed at COMCO) has been customized for the analysis of viscoplastic solids in contact with a rigid flat, including elastic or viscoplastic material properties, contact and sliding resistance.

The comparisons of numerical predictions of asperity response with available analytical solutions and experimental measurements confirms the correctness of the formulation and of the finite element solution procedure. In fact, it appears that the actual experiments require more caution than the numerical solutions, because of calibration difficulties and pollution of the results by the compliance of the apparatus. These experiences will be taken into account in the third year of this project.

The effort in the third year will focus on the actual development of the interface models through the statistical homogenization procedure, as well as on their verification and applications. In particular, the following tasks are planned for the third year:

1. Evaluate the results of comparisons performed up-to-date and implement the necessary corrections in the numerical code and in the experimental apparatus. Design and perform experimental measurements for a random surface corresponding to a typical surface finish (*e.g. sand blasting*).

2. Extend the finite element asperity modeling code to include selected models of adhesion and sliding resistance valid for micro-scale asperities (up-to-date the effort has focused on macro-scale asperities).

3. Combine the finite element asperity analysis with the statistical homogenization software to develop new asperity-based models of contact, adhesion and friction. This will include surfaces documented in the literature as well as the surface which will be studied in the experiment.

4. Evaluate the results of the above comparisons and identify possible sources of discrepancies.

5. Formulate a theory and methodology for the application of the new interface models in the modeling of dynamic friction phenomena, such as friction in presence of vibrations or self-exited oscillations in frictional sliding.

9 References

1. Abbott, E. J., and Firestone, F. A , "Specifying Surface Quality," *Mechanical Engineering*, Vol. 55, p. 569, 1933.

2. Amontons, G., "De la Résistance Causeé dans les Machines," *Memoires de l'Academie Royale*, pp. 275–282, 1699.

3. Andrew, C., Cockburn, J. A., and Waring, A. E., "Metal Surfaces in Contact Under Normal Forces: Some Dynamic Stiffness and Damping Characteristics," *Proc. Instn. Mech. Engrs.*, 182(3K), pp. 92–100, 1968

4. Back, N. Burdekin, M., and Cowley, A., "Review of the Research on Fixed and Sliding Joints," **Proc. 13th Internat. Machine and Tool Design and Research Conference**, pp. 87–97, ed. by S. A. Tobias and F. Koenigsberger, MicMillan, London, 1973.

5. Bank, R. E., Sherman, A. H., and Weisr, A., "Refinement Algorithms and Data Structures for Regular Mesh Refinement," in **Scientific Computing**, R. Stepleman, *et al.* (Eds), IMACS, North Holland, 1983.

6. Bass, J. M., and Oden, J. T., "Adaptive Finite Element Methods for a Class of Evolution Problems in Viscoplasticity," *Int. J. Eng. Sci.*, Vol. 25, No. 6, pp. 623–653, 1987.

7. Bass, J. M., and Oden, J. T., "Numerical Solution of the Evolution Equations of Damage and Rate–Dependent Plasticity," *Int. J. Engng. Sci.*, Vol. 26, No. 7, pp. 713–740, 1988.

8. Bay, N., and Wanheim, T., "Real Area of Contact and Friction Stress at High Pressure Sliding Contact," *Wear*, **38**, pp. 201–209, 1976.

9. Bobrik, P. I., **Effect of the Surface Finish of Metals on Loaded Joints**, Thesis, Moscow Inst. Aircraft Technol. (MATI), 1947.

10. Bodner, S. R., "Review of a Unified Elastic–Viscoplastic Theory," in **Unified Constitutive Equations for Plastic Deformation and Creep of Engineering Alloys** (Edited by A. K. Miller), Elsevier and Applied Science, London, 1985.

11. Bodner, S. R., and Chan, K. S., "Modeling of Continuum Damage for Application in Elastic-Viscoplastic Constitutive Equations," *Engineering Fracture Mechanics*, Vol. 25, Nos. 5–6, pp. 705–712, 1986.

12. Bodner, S. R., and Partom, Y., "A Large Deformation Elastic–Viscoplastic Analysis of a Thick Walled Spherical Shell," *Journal of Applied Mechanics*, **39**, p. 751, 1972.

13. Bowden, F. P., and Tabor, D., **The Friction and Lubrication of Solids**, Clarendon Press, Oxford, 1950.

14. Bowden, F. P., and Tabor, D., **The Friction and Lubrication of Solids, Part II**, Clarendon Press, Oxford, 1964.

15. Boyd, J., and Robertson, B. P., "The Friction Properties of Various Lubricants at High Pressures," *Trans. ASME*, **67**, pp. 51–59, 1945.

16. Brandt, S., "Statistical and Computational Methods in Data Analysis," North Holland, 1976.

17. Briscoe, B. J., Scruton, B., and Willis, F. R., "The Shear Strength of Thin Lubricant Films," **Proc. Roy. Soc. (London)**, A333, pp. 99–114, 1973.

18. Briscoe, B. J., and Tabor, D., "The Effect of Pressure on the Frictional Properties of Polymers," *Wear*, **34**, pp. 29–38, 1975.

19. Brockley, C. A., and Davis, H. R., "The Time Dependence of Static Friction," *Journ. Lubr. Technol.*, **90**, pp. 35–41, 1968.

20. Broniec, Z., and Lenkiewicz, W., "Static Friction Process Under Dynamic Loads and Vibration," *Wear*, **80**, pp. 261–271, 1980.

21. Buckley, D., "The Metal-to-Metal Interface and its Effect on Adhesion and Friction," *Journ. of Colloid and Interface Science*, **58**, pp. 36–53 1977.

22. Burwell, J. T., and Rabinowicz, E., "The Nature of the Coefficient of Friction," *Journ. Appl. Phys.*, **24**, 2, pp. 136–139, 1953.

23. Bush, A. W., Gibson, R. D., and Thomas, T. R., "The Elastic Contact of a Rough Survace," *Wear*, **35**, pp. 87–111, 1975.Cartwright, D. E., Lonquet-Higgins, M. S., "The Distribution of the Maxima of a Random Functions," **Proc. Roy. Soc.**, **237**, Ser. A. pp. 212–232, 1956.

24. Chan, K. S., Lindholm, U. S., Bodner, S. R., Hill, J. R., Weber, R. M., and Meyer, T. G., "Constitutive Modeling for Isotropic Materials (HOST)," *Third Annual Report*, Southwest Research Institute, San Antonio, Texas, NASA Cr-179522, August, 1986.

25. Chan, K. S., Lindholm, U. S., and Bodner, S. R., "Constitutive Modeling for Isotropic Materials (HOST)," *Final Report*, Southwest Research Institute, San Antonio, Texas, NASA CR-182132, June, 1988.

26. Chang, H. T., Etsion, I., and Bogy, D. B., "An Elastic–Plastic Model for the Contact of Rough Surfaces," *University of California Berkeley Report*, No. UCB-MICRO 85–126 #1, March 1986.

27. Chang, W. R., Etsion, I., and Bogy, D. B., "Adhesion Model for Metallic Rough Surfaces," *University of California Berkeley Report*, No. UCB-MICRO 85–126 #2, March 1986.

28. Chang, W. R., Etsion, I., and Bogy, D. B., "Static Friction Coefficient Model for Metallic Rough Surfaces," *University of California Berkeley Report*, No. UCB-MICRO 85-126 #3, March 1986.

29. Choiu, Y. C., Kato, L., and Abe, H., "The Effect of Normal Damping in the Loading System on the Wear of Low Carbon Steel," *Wear*, **114**, pp. 73-84, 1987.

30. Connoly, R., Schofield, R. E., and Thornley, R. H., "The Approach of Machined Surfaces With Particular Reference to Their Hardness," **Advances in Machine Tool Design and Research**, Proc. 8th Intern. M.T.D.R. Conf., Univ. of Manchester, Part 2, ed. by S. A. Tobias and F. Koenigsberger, Pergamon Press, Oxford, pp. 759-775, 1967.

31. Connoly, R., and Thornley, R. H., "The Significance of Joints on the Overall Deflection of Machine Tool Structures," **Advances in Machine Tool Design and Research**, Proc. of the 6th Intern. M.T.D.R. Conf., ed. by S. A. Tobias and F. Koenigsberger, pp. 139-156, Pergamon Press, Oxford, September 1965.

32. Coulomb, C. A., "Theorie des machiens simples," **Memoire de Mathematique et de Physique de l'Academie Royale**, pp. 161-342, 1785.

33. Courtney-Pratt, J. S., and Eisner, E., "The Effect of Tangential Force on the Contact of Metallic Bodies," **Proc. Royal Soc. Lond.**, A238, pp. 529-550, 1957.

34. Demkowicz, L., Oden, J. T., Rachowicz, W., and Hardy, O., "Toward a Universal *h-p* Adaptive Finite Element Strategy. Part 1: Constrained Approximation and Data Structure," *Comp. Meth. in Appl. Mech. and Engrg.*, **77**, pp. 79-112, 1989.

35. Demkowicz, L., and Oden, J. T., "A Review of Local Mesh Refinement Techniques and Corresponding Data Structures in *h*-Type Adaptive Finite Element Methods," **TICOM Report 88-02**, The Texas Institute for Computational Mechanics, The University of Texas at Austin, Texas 78712.

36. Derjaguin, B. V., Muller, V. M., and Toporov, Y. P., "Effect of Contact Deformations on the Adhesion of Particles," *Journal of Colloid and Interface Science*, **53**, pp. 314-326, 1975.

37. Drucker, D. C., "Coulomb Friction, Plasticity and Limit Loads," *J. Appl. Mech.*, Trans. ASME, **21**, pp. 71-74, 1954.

38. Felder, E., "Formulation thermodynamique des interactions superficielles entre deux corps," *Journal de Mecanique Theorique et Appliqueé*, **4**, 2, pp. 283-303, 1985.

39. Ferrante, J., Smith, J., and Rose, J. H., "Metallic Adhesion and Bonding," **Tribology in the 80's**, NASA CP2300, pp. 143-163, 1983.

40. Ferrante, H. A., "Phenomenological Analysis of Plastic Spherical Indentation," *ASME Journal of Engineering Material Technology*, **98**, pp. 272-281, 1976.

41. Francis, H. A., "Application of Spherical Indentation Mechanics to Reversible and Irreversible Contact Between Rough Surfaces," *Wear*, **45**, pp. 261–269, 1977.

42. Fuller, K. N. G., and Tabor, D., "The Effect of Surface Roughness on the Adhesion of Elastic Solids," **Proc. Roy. Soc. (London)**, A345, pp. 327–342, 1975.

43. Greenwood, J. A., and Tripp, J. H., "The Elastic Contact of Rough Spheres," *Journal of Applied Mechanics*, **34**, pp. 134–159, 1967.

44. Greenwood, J. A., and Williamson, J. B. P., "Contact of Nominally Flat Surfaces," **Proc. Roy. Soc. (London)**, Series A295, pp. 300–319, 1966.

45. Gu, J. C., Rice, J. R., Ruina, A. L., and Tse, S. T., "Slip Motion and Stability of a Single Degree of Freedom Elastic System With Rate and State Dependent Friction," *J. Mech. Phys. Solids*, 1983.

46. Halling, J., and Nuri, K. A., in dePater, A. D. and Kalker, J. J. (Eds.) "The Mechanics of the Contact Between Deformable Bodies," **Delft University Press**, Delft, pp. 330–341, 1975.

47. Hertz, H., "Uber die Beruhrun fester elast sche Korper und uber die Harte," **Verhandlungen des Vereins zur Beforderung des Gewerbefleisses Leipzig**, Nov. 1882.

48. Hisakado, T., "Effect of Surface Roughness on Contact Between Solid Surfaces," *Wear*, **28**, pp. 217–234, 1974.

49. Hisakado, T., and Tsukizoe, T., "Effects of Distribution of Surface Slopes and Flow Pressures of Contact Asperities on Contact Between Solid Surfaces," *Wear*, **30**, pp. 213–227, 1974.

50. Johannes, V. I, Green, M. A., and Brockley, C. A., "The Role of the Rate of Application of the Tangential Force in Determining the Static Friction Coefficient," *Wear*, **24**, pp. 384–385, 1973.

51. Johnson, K. L, Kendall, K., and Roberts, A. D., "Surface Energy and the Contact of Elastic Solids," **Proc. Roy. Soc. (London)**, A234, pp. 301–313, 1971.

52. Kato, S., Sato, N., and Matsubayachi, T., "Some Considerations on Characteristics of Static Friction of Machine Tool Slideway," *Journ. Lubr. Technol.*, **94**, pp. 234–247, 1972.

53. Kikuchi, N., and Oden, J. T., **Contact Problems in Elasticity: A Study of Variational Inequalities and Finite Elements**, *SIAM*, Philadelphia, 1988.

54. Kumar, V., Morjaria, M., and Mukherjee, S., "Numerical Integration of Some Constitutive Models of Inelastic Deformation," *J. Engineering Materials and Technology*, Vol. 102, pp. 92–96, Jan. 1980.

55. Lindholm, U.S., Chan, K.S., Bodner, S.R., Weber, R.M., Walker, V.P., Bassenti, B.N., "Constitutive Modelng for Isotropic Materials", annual report NASA CR 174980, Contract No. NAS3-23925, 1985.

56. Lonquet-Higgins, M. S., "The Statistical Analysis of a Random Moving Surface," **Phil. Trans. of Roy. Soc., 249**, Ser. A, pp. 321–387, 1957.

57. Lonquet-Higgins, M. S., "Statistical Properties of an Isotropic Random Surface," **Phil. Trans. of Roy. Soc., 250**, Ser. A, pp. 157–174, 1957.

58. Lonquet-Higgins, M. S., "The Statistical Geometry of Random Surfaces," in *Hydrodynamic Stability*, **Proc. 13th Symp. on Appl. Math.**, American Math. Society, 1962.

59. Martins, J. A. C., "Dynamic Frictional Contact Problems Involving Metallic Bodies," *Ph.D. Dissertation*, The University of Texas, Austin, Texas, 1985.

60. McCool, J. J., "Predicting Microfracture in Ceramics Via a Microcontact Model," **Trans. ASME**, *Journal of Tribology*, **108**, pp. 380–386, 1986.

61. McFarlane, J. S., and Tabor, D., "Adhesion of Solids and the Effect of Surface Films," **Proc. Roy. Soc.** (London), A202, pp. 224–243, 1950.

62. Michalowski, R., and Mroz, Z., "Associated and Non–Associated Sliding Rules in Contact Friction Problems," *Archives of Mechanics*, **30**, pp. 259–276, 1978.

63. Mindlin, R. D., "Compliance of Elastic Bodies in Contact," *Journal of Applied Mechanics*, **16**, pp. 259–268, 1949.

64. Moore, D. F., **Principles and Applications of Tribology**, Pergamon Press, Oxford, 1975.

65. Muller, V. M., Derjaguin, B. V., and Toporov, Y. P., "On Two Methods of Calculation of the Force of Sticking of an Elastic Sphere to a Rigid Plane," *Colloids and Surfaces*, **7**, p. 251, 1983.

66. Muller, V. M., Yushchenko, V. S., and erjaguin, B. V., "On the Influence of Molecular Forces on the Deformation of an Elastic Sphere and Its Sticking to a Rigid Plane," *Journal of Colloid and Interface Science*, **77**, pp. 91–101, 1980.

67. Nayak, P.R., "Random Process Model of Rough Surfaces," *ASME Journal of Lubrication Technology*, **93**, pp. 398–407, 1971.

68. Nolle, H., and Richardson, R. S., "Static Friction Coefficient for Mechanical and Structural Joints," *Wear*, **28**, pp. 1–13, 1974.

69. Oden, J. T., Demkowicz, L., Rachowicz, W., and Westermann, T. A., "Toward a Universal *h-p* Adaptive Finite Element Strategy. Part 2: *A Posteriori* Error Estimation," *Comp. Meth. in Appl. Mech. and Engrg.*, **77**, pp. 113–180, 1989.

70. Oden, J. T., and Martins, J. A. C., "Models and Computational Methods for Dynamic Friction Phenomena," *Computer Methods in Applied Mechanics and Engineering*, **52**, pp. 527–634, 1985.

71. Oden, J. T., Martins, J. A. C., and Tworzydlo, W. W., "Computational Methods for Nonlinear Dynamic Problems in Solid and Structural Mechanics: Progress in the Theory and Modeling of Friction and in the Control of Dynamical Systems With Frictional Forces," COMCO Technical Report, Bolling Air Force Base, AFOSR Contract F49620-86-C-0051, 1989.

72. Pashley, M. D., "Further Consideration of the DMT Model for Elastic Contact," *Colloids and Surfaces*, **12**, pp. 59–77, 1984.

73. Pashley, M. D., and Pethica, J. B., "The Role of Surface Forces in Metal – Metal Contacts," *Journal Vac. Sci. Tech.*, A3, pp. 757–761, 1985.

74. Pashley, M. D., Pethica, J. B., and Tabor, D., "Adhesion and Micromechanical Properties of Metal Surfaces," *Wear*, **100**, pp.. 7–31, 1984.

75. Rabier, P., Martins, J. A. C., Oden, J. T., and Campos, L., "Existence and Local Uniqueness of Solutions to Contact Problems in Elasticity with Nonlinear Friction Laws," *International Journal of Engineering Science*, Vol. 24, No. 11, pp. 1755–1768, 1986.

76. Rabinowicz, E., "The Nature of the Static and Kinetic Coefficients of Friction," *Journ. Appl. Physics*, 11, **22**, pp. 1373–1379, 1951.

77. Rabinowicz, E., "The Intrinsic Variables Affecting the Stick-Slip Process," *Proc. Phys. Soc.*, **71**, pp. 668–675, 1958.

78. Rabinowicz, E., "The Determination Between Solids in Vacuum; II. Deformation and Interfacial Energy," *Journal of Physics*, Vol. 11, pp. 39–54, 1978.

79. Rice, J. R., and Ruina, A. L., "Stability of Steady Frictional Slipping," **ASME Applied Mechanics, Bioengineering, and Fluids Engineering Conference**, Paper No. 83-APM-16, Houston, Texas, June 1983.

80. Richardson, R. S. H., and Nolle, H., "Surface Friction Under Time–Dependent Loads," *Wear*, **37**, pp. 87–101, 1976.

81. Ruina, A. L., **Friction Laws and Instabilities: A Quasistatic Analysis of Some Dry Frictional Behavior**, Ph.D. Thesis, Brown University, Providence, R.I., 1980.

82. Ruina, A. L., "Slip Instability and State Variable Friction Laws," *J. Geophys. Res.*, 1983.

83. Ruina, A. L., "Constitutive Relations for Frictional Slip," **Mechanics of Geomaterials**, ed. by Z. Bazant, John Wiley and Sons, pp. 163–187, 1985.

84. Sampson, J. B., Morgan, F., Reed, D. W., and Muskat, M., "Friction Behaviour During the Slip Portion of the Stick–Slip Process," *Journ. Appl. Physics*, **14**, pp. 689–700, 1943.

85. Sanchez-Palencia, E., and Suqet, P., "Friction and Homogenization of a Boundary," 1983.

86. Soom, A., and Kim, C., "Interactions Between Dynamic Normal and Frictional Forces During Unlubricated Sliding," *Journ. Lubr. Technol.*, **105**, pp. 221–229.

87. Soom, A., and Kim, C., "Roughness–Induced Dynamic Loading at Dry and Boundary–Lubricated Sliding Contacts," *Journ. Lubr. Technol.*, **105**, pp. 514–517, 1983.

88. Tabor, D., "Friction—The Present State of Our Understanding," *Journ. Lubr. Technol.*, **103**, pp. 169–179, 1981.

89. Tallian, T. E., *Wear*, **21**, p. 49, 1972.

90. Timoshenko, S. and Goodier, J.N., **Theory of Elasticity**, McGraw-Hill, New York, 2nd edition.

91. Towle, L. C., "Shear Strength and Polymer Friction," *Am. Chem. Soc. Polymer Science and Technology*, Vol. 5A, pp. 179–189, 1974.

92. Tworzydlo, W., and Becker, E., "Influence of Forced Vibrations on the Static Coefficient of Friction–Numerical Analysis," *Wear*, **143**, pp. 175–186, 1991.

93. Tworzydlo, W., and Becker, E., "Numerical Study of Friction–Induced Vibrations and Dynamic Instabilities of Frictional Systems," in **Friction-Induced Vibration, Chatter, Squeal, and Chaos**, Ibrahim, R.A. and Soom, A., editors, ASME Publications, New York, 1992, pp. 13-32.

94. Tworzydlo, W., and Oden, J.T., "New Micro- and Macroscopic Models of Contact and Friction ," annual report, AFOSR contract F49620-91-C-0011, 1991.

95. Tworzydlo, W.W. and Oden, J.T., "Towards an Automated Environment in Computational Mechanics", to appear in Comp. Meths. Appl. Mech. Engng. in 1993.

96. Villaggio, P., "An Elastic Theory of Coulomb Friction," *Archive for Rational Mechanics and Analysis*, Vol. 70, pp. 135–143, 1979.

97. Votinov, K. V., **The Rigidity of Machine Tools**, Leningrad Section, Machine Builders' Union (LONITOMASH), Leningrad, 1940.

98. Weic, W. L., "The Investigation of the Static Friction and the Direction of Sliding at Low–Frequency External Vibrations," *New in Friction Theory*, Lzd. Akad, Nauk SSSR, Moscow, pp. 60–82, 1962.

99. Whitehouse, D. J., and Archard, J. F., "The Properties of Random Surfaces of Significance in Their Contact," **Proc. Roy. Soc. (London)**, A316, pp. 97–121, 1970.

100. Wilson, Ph.D. Thesis, University of Cambridge, 1952.